AD_____

Award Number: W81XWH-06-1-0328

TITLE: Three-Dimensional Near Infrared Imaging of Pathophysiological Changes within the Breast

PRINCIPAL INVESTIGATOR: Phaneendra K. Yalavarthy

CONTRACTING ORGANIZATION: Dartmouth College
Hanover, NH 03755

REPORT DATE: March 2008

TYPE OF REPORT: Annual Summary

PREPARED FOR: U.S. Army Medical Research and Materiel Command
Fort Detrick, Maryland 21702-5012

REPORT DOCUMENTATION PAGE

Form Approved
OMB No. 0704-0188

1. REPORT DATE *(DD-MM-YYYY)*	**2. REPORT TYPE**	**3. DATES COVERED** *(From - To)*
01-03-2008	Annual	03 Feb 2007 - 02 Feb 2008

4. TITLE AND SUBTITLE

Three-Dimensional Near Infrared Imaging Of Pathophysiological Changes Within The Breast

5a. CONTRACT NUMBER

5b. GRANT NUMBER
W81XWH-06-1-0328

5c. PROGRAM ELEMENT NUMBER

6. AUTHOR(S)
Phaneendra K. Yalavarthy

E-Mail: pyalavarthy@wustl.edu

5d. PROJECT NUMBER

5e. TASK NUMBER

5f. WORK UNIT NUMBER

7. PERFORMING ORGANIZATION NAME(S) AND ADDRESS(ES)

Dartmouth College
Hanover, NH 03755

8. PERFORMING ORGANIZATION REPORT NUMBER

9. SPONSORING / MONITORING AGENCY NAME(S) AND ADDRESS(ES)
U.S. Army Medical Research and Materiel Command
Fort Detrick, Maryland 21702-5012

10. SPONSOR/MONITOR'S ACRONYM(S)

11. SPONSOR/MONITOR'S REPORT NUMBER(S)

12. DISTRIBUTION / AVAILABILITY STATEMENT
Approved for Public Release; Distribution Unlimited

13. SUPPLEMENTARY NOTES

14. ABSTRACT

Near Infrared optical imaging is a non-invasive and non-ionizing medical imaging technique that can image functional properties of biological tissue using Near Infrared (NIR) light. Due to the dominance of scattering of light in tissue, modeling of light propagation in tissue requires advanced computational methods. This project was aimed to develop novel computational methods that will lead to use of optical imaging in a routine clinical setting. As a part of this work, an optimization of computational parameters for the existing methods was performed. A novel algorithm which includes noise characteristics of the instruments was also developed to get an optimal estimate of breast tissue optical properties. New methods for effectively using Magnetic resonance image information in NIR image reconstruction procedure were also developed to improve the total outcome of NIR functional images of breast. Optical image reconstruction methods that improve the computational efficiency by a factor of 10 for three-dimensional optical imaging were also developed.

15. SUBJECT TERMS
Near Infrared medical imaging, Diffuse Optical Tomography, Breast tissue characterization

16. SECURITY CLASSIFICATION OF:			**17. LIMITATION OF ABSTRACT**	**18. NUMBER OF PAGES**	**19a. NAME OF RESPONSIBLE PERSON**
a. REPORT	**b. ABSTRACT**	**c. THIS PAGE**			USAMRMC
U	U	U	UU	103	**19b. TELEPHONE NUMBER** *(include area code)*

Standard Form 298 (Rev. 8-98)
Prescribed by ANSI Std. Z39.18

Table of Contents

Page

Introduction……..…….…..….. **3**

Body…… **4**

Key Research Accomplishments…….…… **9**

Reportable Outcomes…… **10**

Conclusion…… **11**

References…… **12**

Appendices…… **12**

Introduction

Figure 1: The fiber optic patient interface.

This project aimed at developing new reconstruction methods that improves the quality and quantification of functional properties in near in near infrared (NIR) imaging [1-3]. This NIR imaging technique uses NIR light (600 nm – 1000 nm) to probe the breast tissue delivered through fiber optic bundles, which are also used to collect the propagated diffused light (fiber-optic setup is shown in Figure 1) [2,3], giving its name diffuse optical tomography (DOT). Modeling of this diffuse light propagation requires advanced computational methods due to the non-linear nature of light propagation, mainly due to the dominance of light scattering over attenuation [1]. Most of the current computational models are in two-dimensions (2D), even though light travels in three-dimensions (3D), due to computational complexity and limited number of measurements. Estimation of functional properties is highly dependent on these computational models and development of new computational methods (image reconstruction methods) in 3D that reduce computational complexity is the main objective of this project.

Specifically, the aims of this project are

1) Reducing the computational complexity of 3D optical imaging by investigating different data collection strategies and optimizing these procedures.
2) Improving the quantitative accuracy of optical images by exploring the effect of penalty terms on the reconstruction techniques. Incorporation of a priori information from other modalities (like MRI, CT) into the reconstruction procedures and studying its effect.
3) Exploring effective ways of displaying and coregistering 3D DOT images.

During last 2 years of funding of this project, the main aims of this project were completed. Optimization of critical computational aspects in NIR imaging was completed. An optimal data-collection strategy especially for the DOT clinical system at Dartmouth for the current estimation of breast tissue optical properties was also found. An effective way for usage of *a priori* structural of information from MRI/CT into the image reconstruction procedure was developed and proven that the quantitative accuracy of DOT images can be improved by at least a factor of two with this additional information. A generalized estimation procedure was developed which will take into account the noise characteristics of instruments and breast tissue optical properties and has been shown robust to highly noisy data. A computationally efficient approach to dramatically reduce the size of the matrix to be inverted in cases where the number of imaging parameters are much larger than the boundary data is developed. This algorithm reformulates the inversion approach, within most least-squares approaches, to allow the inversion to be based upon the size of the data, rather than the number of imaging field parameters, and this is useful for most 3D imaging situations. This algorithm improved the computational speed by at least a factor of three. The final aim of the project was modified, as there are commercial platforms available to coregister 3D DOT images with MRI/CT (for example, OMIRAD from Siemens [4]; available to NIR imaging group from Siemens as a part of network effort funded by NIH (U54 CA105480: Network for Translational Research in Optical Imaging)), to an important problem to find methods to counteract the noisy data (which is more common in imaging large breasts (> 8 cm in diameter)). This noisy data causes large artifacts when used in the traditional reconstruction methods, some times these traditional methods may not be able to converge to any meaningful solutions in these cases. When the experimental system

was characterized to provide noise characteristics of the data collected, along with structural and spectral prior information, using these (noise characteristics) in the generalized reconstruction approach was proven to give more quantitative accurate images (with in 20% error limit) of spectrally-derived tissue functional properties even in cases of highly noisy experimental phantom data. With out these noise characteristics, traditional reconstruction algorithms are not able to provide any meaningful functional images.

Body

Optimizing the critical computational aspects of near infrared tomographic imaging

The image resolution and contrast in Near-Infrared (NIR) tomographic image reconstruction are affected by parameters such as the number of boundary measurements, the mesh resolution in the forward calculation and the reconstruction basis. The magnitude of the total sensitivity was analyzed to find the spatial variation for a given problem, and the field response of the domain becomes more uniform by increasing the sensitivity to deeper regions, while suppressing the hypersensitivity near the external boundaries. This is achieved with an increase in the number of measurements.

Using singular-value decomposition (SVD) and example reconstructed images, numbers of 16 or 24 fibers are sufficient for imaging the 2D domain. The number of useful measurements actually decreases exponentially with the number of measurements used, and the number of useful singular values increases only as the logarithm of the number of measurements. For this 2D reconstruction problem, given a computational limit of 10 sec per iteration, leads to choice of forward mesh with 1785 nodes and reconstruction (pixel) basis of 30x30 elements.

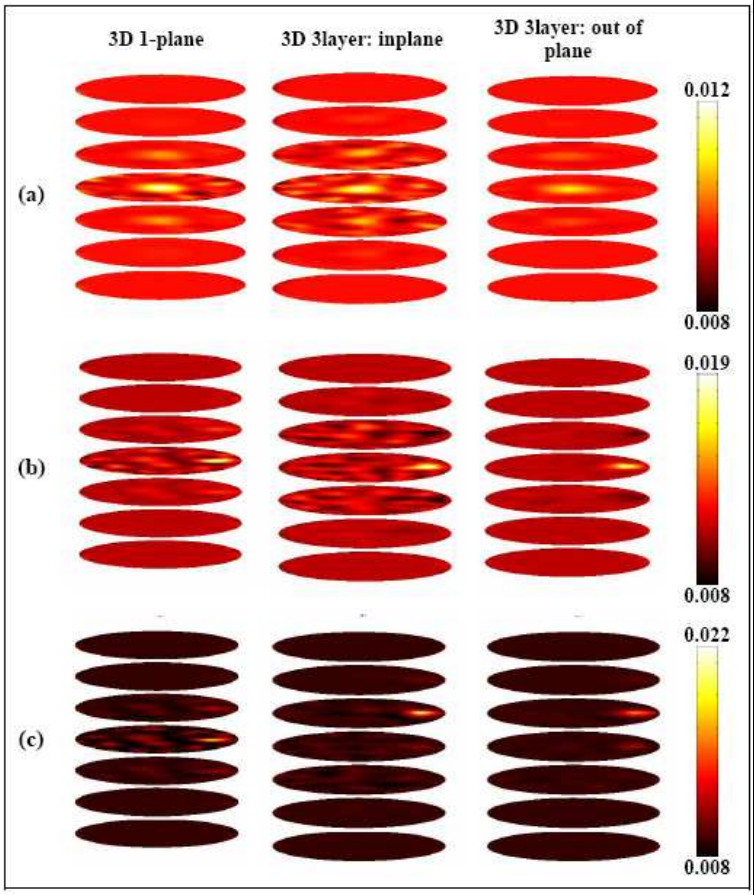

Figure 2: The reconstructed absorption coefficient distribution for the cylindrical object with a spherical absorption inhomogeneity (diameter of 15mm and contrast 2:1 with respect to background) located at x, y and z locations (a) (0,0,0), (b) (30,0,0) and (c) (30,0,10). The three columns of images show the results achieved with the three different data collection schemes

The use of three fundamentally different data collection strategies for three-dimensional (3D) NIR tomography was compared. Given a 3D NIR imaging problem, using a single plane of data can provide useful images if the anomaly to be reconstructed is within the measurement plane. However, if the location of the anomaly is not known, 3D data collection strategies are very important. The recovered quantitative accuracy of the anomaly region decreases (approximately 10%) with the addition of out-of-plane data relative to in-plane data. Usage of

single-plane of data gives slightly better quantitative accuracy, if the anomaly lies in the data acquisition plane. Further the quantitative accuracy of the reconstructed anomaly increased approximately from 15% to 89% as the anomaly moved from the centre to boundary, respectively. The data supports the idea that the use of in-plane data in the 3D data collection strategies may be sufficient for the 3D NIR imaging.

Complete work along with the methods employed and detailed discussion of the results given in the appendix [5] (Yalavarthy et al, Opt. Express 14, p. 6113-6127, 2006).

Usage of structural a-priori information

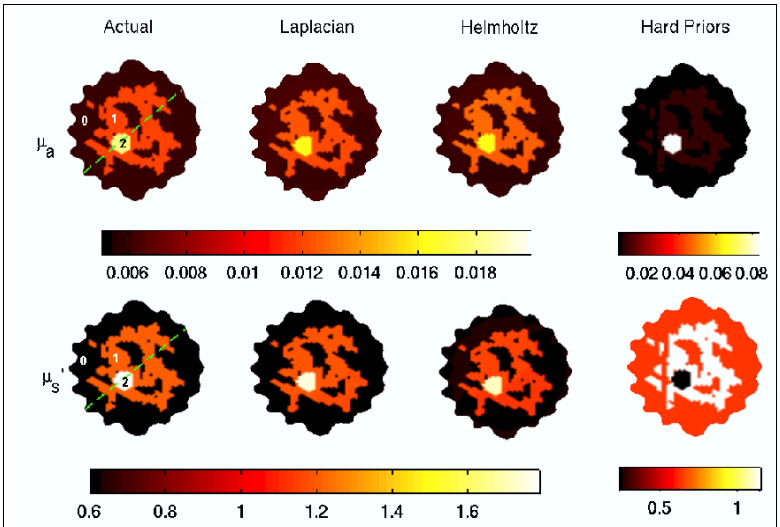

Figure 3: Reconstruction results with the usage of imperfect structural priors using different reconstruction techniques.

NIR tomography combined with conventional imaging modalities (MRI, CT and Ultra Sound) has been a very active area of research. These hybrid systems show superior performance in terms of qualitative (resolution) and quantitative accuracy compared to stand-alone systems. But still there is lot of ambiguity in utilizing the spatial information from these high spatial resolution images into NIR tomography (coregistration). This work develops a simple framework to incorporate structural a-priori information. Simple weight matrices that have Laplacian-type or Helmholtz-type structures that are derived from a-priori information have been developed. It has been shown that utilization of structural information using these weight matrices will not bias the reconstruction problem towards imperfect structural priors. Usage of imperfect a-priori information in a parameter reduction (i.e. hard-priors) in the imaging field through the enforcement of spatially explicit regions gives erroneous results. In the phantom experiments, it is shown that the Helmholtz type of regularization matrix gives the best estimate of the scattering parameter and the Laplacian provides best estimate for the absorption parameter. Overall, usage of structural-priors improve the reconstructed image quantitative accuracy by at least a factor of two.

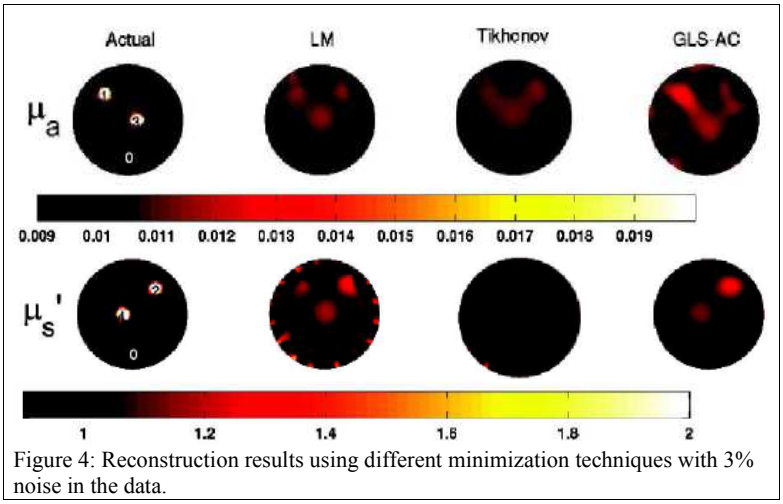

Figure 4: Reconstruction results using different minimization techniques with 3% noise in the data.

Details of the implementation along with analysis of results given in the appendix [6] (Yalavarthy et al, Opt. Express 15, p. 8043-8058, 2007).

Generalized Least-Squares (GLS) minimization: Two-dimensional imaging (Numerical Study)

DOT involves recovery of the distribution of optical parameters by matching the experimental data with modeled data (Levenberg-Marquardt (LM) Minimization). A variation of this approach by adding the parameter field to the minimization

function is done through Tikhonov regularization, where the regularization parameter is chosen to overcome the ill-conditioning of the problem. In this work, a generalized framework for DOT was developed including variance of the data and parameters as weight matrices. These weight matrices can also include the structural information obtained by MRI, Ultrasound or X-ray imaging. These weight matrices, include the system noise characteristics and expected size of optical parameters and constraints for the imaging problem and make the inversion routine more robust to noise. This also makes the imaging problem more stable. It is also important to note that Tikhonov regularization becomes a special case of the Generalized Least-Squares (GLS) formulation. This GLS estimation of optical properties has been shown to be very robust to noise and proven to be stable over iterations.

Complete formulation along with results is given in the appendix [6] (Yalavarthy et al, Med. Phys. 34, p. 2085-2098, 2007).

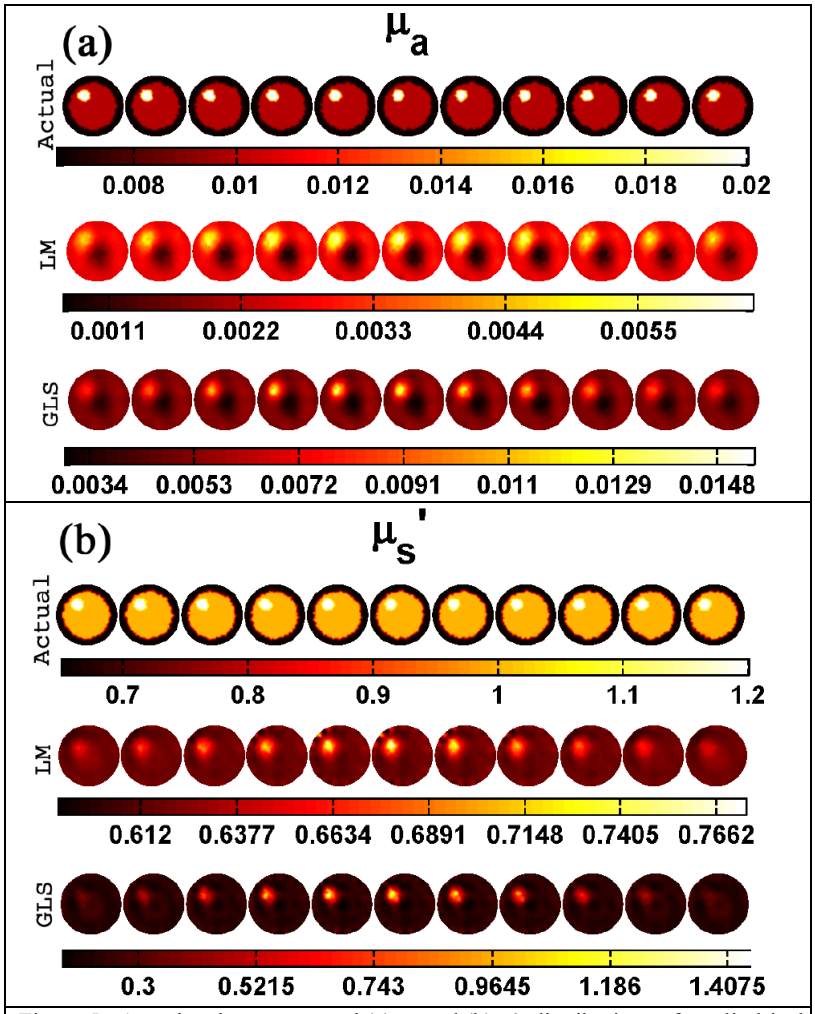

Figure 5: Actual and reconstructed (a) μ_a and (b) μ'_s distributions of a cylindrical target using experimental multi-layered phantom data. Two-dimensional cross-sections of the 3D volume in 2.5 mm increments spanning from z = -12.5 mm to z = 12.5 mm (from left to right) are shown. Actual distributions are given in the first row. Reconstructed distribution using the Levenberg-Marquardt (LM) minimization scheme and GLS minimization scheme are presented in the middle and last rows respectively.

A computationally efficient algorithm for three-dimensional imaging

Three-dimensional (3D) diffuse optical tomography (DOT) is known to be a non-linear, ill-posed and sometimes under-determined problem, where regularization is added to the minimization to allow convergence to a unique solution. In this work, a generalized least-squares (GLS) minimization method was implemented, which employs weight matrices for both data-model misfit and optical properties to include their variances and covariances, using a computationally efficient scheme. This allows inversion of a matrix that is of dimension dictated by the number of measurements, instead of by the number of imaging parameters. This increases the computation speed up to four times per iteration in most of under-determined 3D imaging problems. An analytic derivation, using the Sherman-Morrison-Woodbury identity, is shown for this efficient alternative form and it is proven to be equivalent, not only analytically, but also numerically. Equivalent alternative forms for other minimization methods, like Levenberg-Marquardt (LM) and Tikhonov, are also derived. 3D reconstruction results indicate that the poor recovery of quantitatively accurate values in 3D optical images can also be a characteristic of the reconstruction algorithm, along with the target size. Interestingly, usage of GLS reconstruction methods reduces error in the periphery of the

image, as expected, and improves by 20% the ability to quantify local interior regions in terms of the recovered optical contrast, as compared to LM methods. Characterization of detector (PMTs) noise have enabled the use of the GLS method for reconstructing experimental data and showed a promise for better quantification of target in 3D optical imaging. Use of these new alternative forms becomes effective when the ratio of the number of imaging property parameters exceeds the number of measurements by a factor greater than 2.

Complete formulation along with the analytic derivation is given in the appendix [7] (Yalavarthy et al, Med. P hys. 2007 (submitted)).

Incorporation of noise characteristics into the near infrared tomographic image reconstruction algorithms

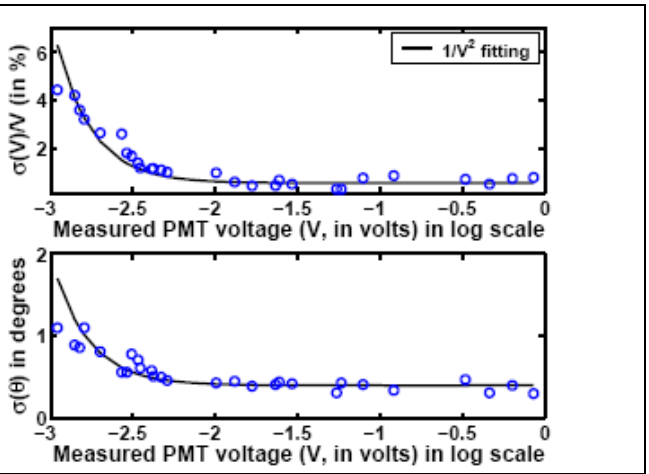

Figure 6: An error (deviation, σ) plot of the measured voltage and phase (θ) as a function of mean of measured PMT voltage. The leger of the figure represents the fitting model used. Each data point corresponds to a sample size of 200.

To incorporate the noise characteristics into the image reconstruction algorithm, the first step was to characterize the experimental data collection system. As photomultiplier tubes (PMT) are used as a detectors in the data-collections syst

em at Dartmouth for the data-collection [8], to measure the deviation in the measured signal, a series of light signal measurements were taken through a homogeneous intralipid phantom experiments were conducted with increasing levels of blood (HbT) concentration, varying from 7.3 μM to 36 μM, leading to a decrease in the measured PMT voltage. To achieve this, the gain of the PMT was kept at 0.9. A concise discussion of the PMT gain setting in the system characterization is given in Ref. [8]. A single source and the farthest detector (number-8) was used for these transmission measurements. For every

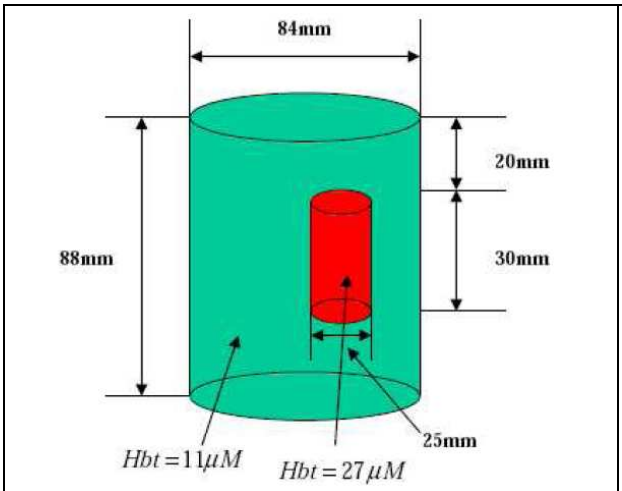

Figure 7: Schematic diagram of cylindrical gelatin phantom showing the dimensions of the imaging domain and the target

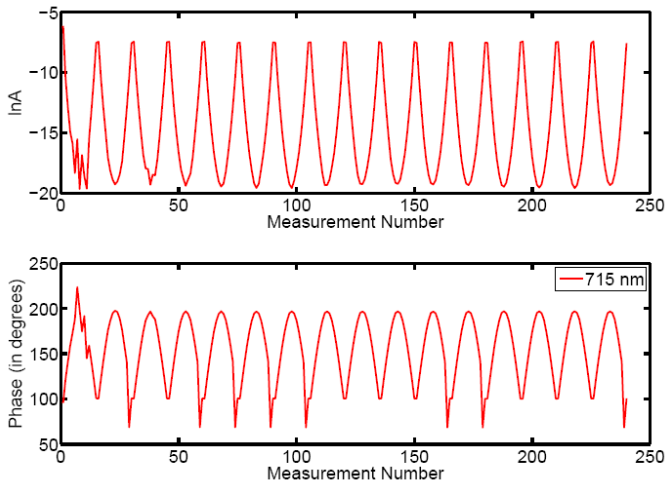

Figure 7: A sample of calibrated data corresponding to wavelength 715 nm collected from the gelatin phantom (schematic diagram is given in Fig.7)

concentration 200 data points were collected to estimate the deviation in the measured voltage using the same gain settings. The approach for the characterization is similar to the one described in Ref. [8], except the raw detected voltage was used here for estimation of the error (or deviation σ). Note also that two sets of diameters,

56 mm and 84 mm, were used to get the voltage in the range of 0-1 volts. This was repeated for all the wavelengths to ensure uniformity of performance in the signal, and to ensure that the trend was independent of wavelength and gain setting.

Figure 6 gives a plot of error ($\sigma(V)/V$) as a function of measured PMT voltage for 785 nm wavelength. A similar trend was observed for other wavelengths. This plot also gives a deviation in phase ($\sigma(\theta)$) in degrees for the same voltage. The lowest voltage that was measured was 0.001, which is in the noise floor. The measured deviations were 1% for lnA (amplitude) and 0.5^o for θ (phase). These values are similar to the ones reported in the literature (Mcbride et. al [8] reported 0.32% for the PMT voltage and 0.48^o in phase). A solid line shows these average deviation using $1/V^2$ fitting (following shot-noise model) in Fig. 6. Using this plot, the noise characteristics can be estimated using the measured PMT voltage. Inclusion of these noise characteristics into the generalized least-squares (GLS) scheme combined with spectral and spatial priors lead to the reasonable estimates of target functional properties in the case of noisy phantom data (example data set from a cylindrical gelatin phantom (Fig. 7) is plotted in Fig. 8).

Methods	*All Det*	*HbT (μM)*		*StO_2 (%)*		*H_20 (%)*		*a*		*b*	
		Bkg	*Target*	*Bkg*	*Target*	*Bkg*	*Target*	*Bkg*	*Target*	*Bkg*	*Target*
Actual	-	11	27	-	-	95.0	95.0	-	-	-	-
LM	NO	10.5	22.5	78.1	81.8	86.6	95.7	0.71	0.74	0.90	1.10
GLS	NO	10.2	22.4	80.1	81.9	88.1	92.8	0.91	0.89	1.05	1.16
GLS	YES	10.4	21.9	81.6	80.5	91.6	90.5	0.93	0.85	1.08	1.11

Table-1: Summary of reconstruction results of phantom data (schematic diagram is given in Fig. 7) using LM and GLS methods. The middle two rows are reconstruction results from the data in which noisy detectors (1, 2, 10, 14, and 15) data points were removed. The last row represents the case of GLS scheme using all the detectors data using noise modle, $1/V^2$ fit (legend of Fig. 6). *Notations*: HbT: Total Hemoglobin (in μM); StO_2: Oxygenation Saturatin (in %); H_20: Waiter content (in %); a: Scattering Amplitude; b: Scattering Power

Typically in these cases of noisy data, an experienced researcher looks at the data and discards the noisy data points from the reconstruction scheme, which becomes very subjective. The aim was to include to the noisy characteristics into the reconstruction scheme using Fig. 6. When this was performed using all the data points, the estimates using GLS reconstruction scheme was with in the 20% error limit of the expected functional properties. In this case of using all the data points, traditional reconstruction algorithm (Levenberg-Marquardt (LM)) did not give any meaningful solutions. These results are summarized in Table-1. The important conclusion from this phantom study is that the GLS procedure (developed as part of this project) is able to give reasonable estimates of the functional properties even when the data from the noisy detectors is used. Where as the traditional algorithms are not able to converge to any meaningful solution when the noisy detectors data was used, and a subjective way of removing the noisy detectors data was able provide reasonable estimates.

All these results along with extensive simulation studies are presented in the chapter-6 of Ref. [9]. We are panning to submit a journal paper with these results and analysis.

Key research accomplishments

- Optimization of computational aspects of DOT image reconstruction (especially, data-collection strategy) (*Aim-1*).
- Effective way of incorporating structural priors into NIR-DOT image reconstruction procedure (*part of Aim-2*)
- Generalized least squares minimization formulation and extensive testing of the algorithm in simulations

(*part of Aim-2*).

- Development of a computationally efficient algorithm for under-determined three-dimensional DOT problems (*part of Aim-2*).
- Inclusion of noise characteristics of the experimental data in the Generalized least squares algorithm to improve the estimation capability of 3D functional images in the case of highly noisy data (*modified Aim-3*).

Reportable outcomes

All the formalities (including thesis defense) for the award of the Ph.D. degree for the P.I. is completed (Appendix contains the completion certificate), where the Ph.D. degree will be awarded at the commencement on June 8, 2008. Due to this training, P.I. is employed as a post-doctoral research associate in the division of medical physics, Department of Radiation Oncology, Washington University School of Medicine in St. Louis.

This funding has lead to 7 journal publications (including 4 first author publications from the P.I.), 6 refereed international conference proceeding (including 2 first author proceeding from the P.I.), and 5 international conference presentations (including 3 presented by the P.I.). These are listed in separate categories in chronological order below.

Journal Publications:

1. **P. K. Yalavarthy**, D. R. Lynch, B. W. Pogue, H. Dehghani, and K. D. Paulsen, "Implementation of a computationally efficient least–squares algorithm for highly underdetermined three-dimensional diffuse optical tomography problems," Med. Phys. 2007 (submitted).
2. M. Eames, B.W. Pogue, **P. K. Yalavarthy**, and H. Dehghani, "An efficient Jacobian reduction method for diffuse optical image reconstruction," Opt. Express 15, 15908–15919 (2007).
3. S. Srinivasan, B. W. Pogue, C. M. Carpenter, **P. K. Yalavarthy**, and K. D. Paulsen, "A boundary element approach for image-guided near-infrared absorption and scatter estimation," Med. Phys. 34 4545–4557 (2007).
4. **P. K. Yalavarthy**, B. W. Pogue, H. Dehghani, C. M. Carpenter, S. Jiang, and K. D. Paulsen, "Structural information within regularization matrices improves near infrared diffuse optical tomography," Opt. Express 15, 8043–8058 (2007).
5. A. L. Darling, **P. K. Yalavarthy**, M. M. Doyley, H. Dehghani, and B. W. Pogue, "Simulated interstitial fluid pressure in soft tissue as a result of externally applied contact pressure," Phys. Med. Biol. 52, 4121–4136 (2007).
6. **P. K. Yalavarthy**, B. W. Pogue, H. Dehghani, and K. D. Paulsen, "Weight-Matrix Structured Regularization Provides Optimal Generalized Least-Squares Estimate in Diffuse Optical Tomography," Med. Phys. 34, 2085–2098 (2007).
7. **P. K. Yalavarthy**, H. Dehghani, B. W. Pogue, and K. D. Paulsen, "Critical computational aspects of near infrared circular tomographic imaging: Analysis of measurement number, mesh resolution and reconstruction basis," Opt. Express 14, 6113–6127 (2006).

Refereed Conference Proceeding:

1. **P. K. Yalavarthy**, R. Langoju, B. W. Pogue, H. Dehghani, A. Patil, and K. D. Paulsen, "Cramer-Rao estimation of error limits for diffuse optical tomography with spatial prior information," Proc. of SPIE 6434 (BiOS-2007 in Photonics West-2007, 20-25 January 2007, San Jose, California), 643403:1-13 (2007).
2. S. C. Davis, H. Dehghani, **P. K. Yalavarthy**, B. W. Pogue, K. D. Paulsen, "Comparing two regularization techniques for diffuse optical tomography," Proc. of SPIE 6434 (BiOS-2007 in Photonics West-2007, 20-25

January 2007, San Jose, California), 64340X:1-12 (2007).
3. H. Dehghani, C. M. Carpenter, **P. K. Yalavarthy**, B. W. Pogue, and J. P. Culver, "Structural a-priori Information in near infrared optical tomography," Proc. of SPIE 6431 (BiOS-2007 in Photonics West-2007, 20-25 January 2007, San Jose, California), 64310B:1-7 (2007).
4. A. Darling, **P. K. Yalavarthy**, H. Dehghani, and B. W. Pogue, "Interstitial fluid pressure due to externally applied force in breast tissue," Proc. of SPIE 6431 (BiOS-2007 in Photonics West-2007, 20-25 January 2007, San Jose, California), 64310Z:1-10 (2007).
5. **P. K. Yalavarthy**, C. Carpenter, S. Jiang, H. Dehghani, B. W. Pogue, and K. D. Paulsen, "Incorporation of MR structural information in diffuse optical tomography using Helmholtz type regularization," Proc. of OSA Biomedical Topical Meetings, OSA Technical Digest, SH29:1-3, Optical Society of America, Washington, DC (2006).
6. C. Carpenter, B. W. Pogue, **P. K. Yalavarthy**, S. Davis, S. Jiang, H. Dehghani, and K. D. Paulsen, "Analysis of 3-dimensional reconstruction in a MR-guided NIR tomography system," Proc. of OSA Biomedical Topical Meetings, OSA Technical Digest, SH33:1-3, Optical Society of America, Washington, DC (2006).

Conference Presentations:
1. **P. K. Yalavarthy**, B. W. Pogue, and H. Dehghani, "A generalized least-squares minimization method for near infrared diffuse optical tomography," Department of Defense Era of Hope Meeting, Baltimore, Maryland 25-28 June 2008 (submitted).
2. B. W. Pogue, C. M. Carpenter, **P. K. Yalavarthy**, S. C. Davis, J. Wang, and K. D. Paulsen, "Recovery of hemoglobin images from MR-guided NIR spectroscopy," SPIE Medical Imaging-2007, San Diego, California, 17-22 February 2007 (*Oral presentation*).
3. B. W. Pogue, C. M. Carpenter, **P. K. Yalavarthy**, H. Dehghani, S. Jiang, X. Wang, W. A. Wells, C. A. Kogel, S. P. Poplack, J. B. Weaver, and K. D. Paulsen, "Proposed methods to improve false positive and false negative rates in MR breast imaging, through combination with NIR broadband spectroscopy/tomography," BiOS-2007 in Photonics West-2007, San Jose, California, 20-25 January 2007 (*Invited oral presentation*).
4. **P. K. Yalavarthy**, B. W. Pogue, H. Dehghani, S. Jiang, and K. D. Paulsen, "Generalized Least-Squares minimization for Magnetic Resonance guided Diffuse Optical Tomography," BiOS-2007 in Photonics West-2007, San Jose, California, 20-25 January 2007 (*Oral presentation*).
5. **P. K. Yalavarthy**, B. W. Pogue, H. Dehghani, S. Jiang, and K. D. Paulsen, "Outline of the Weighted Least-Squares minimization for Diffuse Optical Tomography," Network for Translational Research Optical Imaging Network (NTROI) Retreat, Hyatt Regency Newport Beach, CA, June 22-24, 2006 (*Poster presentation*).

Conclusions

This project was part of continuing effort to develop methods/algorithms for three-dimensional alternative breast imaging modalities at Dartmouth. Some important miles stones in the project include completing the work on optimizing the NIR data-collection strategies in 3D (completing Aim-1). A framework to incorporate the spatial-priors in to the NIR image reconstruction procedure was developed and also proven to be effective even in case of imperfect spatial priors, which is part of Aim-2. Moreover, a new algorithm that takes into account noise characteristics of the instruments was developed and tested extensively in the simulation studies. A computational efficient algorithm which reduces the computational cost of three-dimensional imaging problem by at least a factor of three was also developed. This algorithm was compared with the traditional reconstruction algorithms and was proven to be effective in the phantom case (completing Aim-2). Rather than finding an effective way of displaying optical images (Aim-3), which could be achieved using a commercial platform (available to NIR imaging group from Siemens as a part of network effort funded by NIH (U54

CA105480: Network for Translational Research in Optical Imaging)), incorporation of noise characteristics into the three-dimensional optical image reconstruction scheme in the case of experimental data was performed and it was tested using phantom data leading to reasonable estimates (20% of expected values) of functional properties of the gelatin phantom (completing the modified Aim-3).

References

1. A. Gibson, J. C. Hebden, and S. R. Arridge, "Recent advances in diffuse optical tomography," Phys. Med. Biol. 50, R1-R43 (2005).
2. S. Srinivasan, B. W. Pogue, S. Jiang, H. Dehghani, C. Kogel, S. Soho, J. J. Gibson, T. D. Tosteson, S. P. Poplack and K. D. Paulsen, "Interpreting Hemoglobin and Water Concentration, Oxygen Saturation and Scattering Measured In Vivo by Near-Infrared Breast Tomography," Proc. Nat. Acad. Sci. U.S.A. 100, 12349-12354 (2003).
3. B. Brooksby, B. W. Pogue, S. Jiang, H. Dehghani, S. Srinivasan, C. Kogel, T. D. Tosteson, J. Weaver, S. P. Poplack and K. D. Paulsen, "Imaging Breast Adipose and Fibroglandular Tissue Molecular Signatures using Hybrid MRI-Guided Near-Infrared Spectral Tomography," Proc. Nat. Acad. Sci. U.S.A. 103, 8828-8833 (2006).
4. F. S. Azar, K. Lee, A. Khamene, R. Choe, A. Corlu, S. D. Konecky, F. Sauer, and A. G. Yodh, "Standardized platform for coregistration of nonconcurrent diffuse optical and magnetic resonance breast images obtained in different geometries," J. Biomed. Opt. 12, 051902 (2007).
5. P. K. Yalavarthy, H. Dehghani, B. W. Pogue, and K. D. Paulsen, "Critical computational aspects of near infrared circular tomographic imaging: Analysis of measurement number, mesh resolution and reconstruction basis," Opt. Express 14, 6113-6127 (2006).
6. P. K. Yalavarthy, B. W. Pogue, H. Dehghani, C. M. Carpenter, S. Jiang, and K. D. Paulsen, "Structural information within regularization matrices improves near infrared diffuse optical tomography," Opt. Express 15, 8043–8058 (2007).
6. P. K. Yalavarthy, B. W. Pogue, H. Dehghani, and K. D. Paulsen, "Weight-Matrix Structured Regularization Provides Optimal Generalized Least-Squares Estimate in Diffuse Optical Tomography," Med. Physics 34(6), 2085-2098 (2007).
7. P. K. Yalavarthy, D. R. Lynch, B. W. Pogue, H. Dehghani, and K. D. Paulsen, "Implementation of a computationally efficient least–squares algorithm for highly underdetermined three-dimensional diffuse optical tomography problems," Med. Phys. 2007 (submitted).
8. T. O. McBride, B. W. Pogue, S. Jiang, U. L. Osterberg, and K. D. Paulsen, "A parallel-detection frequency-domain near-infrared tomography system for hemoglobin imaging of the breast in vivo," Rev. Sci. Instr. 72, 1817–1824 (2001).
9. P. K. Yalavarthy, *A generalized least-squares minimization method for near infrared diffuse optical tomography*, Ph.D. Thesis, Dartmouth College 2007.

Appendix

The Ph.D. degree completion certification of the P.I. from the Registrar is attached. Four journal papers (one manuscript and three published) are attached which were a direct result of this project, where P.I. being the first author.

1. **P. K. Yalavarthy**, H. Dehghani, B. W. Pogue, and K. D. Paulsen, "Critical computational aspects of near infrared circular tomographic imaging: Analysis of measurement number, mesh resolution and reconstruction basis," Opt. Express 14, 6113–6127 (2006).
2. **P. K. Yalavarthy**, B. W. Pogue, H. Dehghani, and K. D. Paulsen, "Weight-Matrix Structured Regularization Provides Optimal Generalized Least-Squares Estimate in Diffuse Optical Tomography," Med. Phys. 34, 2085–

2098 (2007).
3. **P. K. Yalavarthy**, B. W. Pogue, H. Dehghani, C. M. Carpenter, S. Jiang, and K. D. Paulsen, "Structural information within regularization matrices improves near infrared diffuse optical tomography," Opt. Express 15, 8043–8058 (2007).
4. **P. K. Yalavarthy**, D. R. Lynch, B. W. Pogue, H. Dehghani, and K. D. Paulsen, "Implementation of a computationally efficient least–squares algorithm for highly underdetermined three-dimensional diffuse optical tomography problems," Med. Phys. 2007 (submitted).

THAYER SCHOOL OF
ENGINEERING
AT DARTMOUTH

Daryl Laware
Registrar
daryl.a.laware@dartmouth.edu
p 603.646.3801 f 603.646.1620

October 24, 2007

To Whom It May Concern:

This is to certify that Phaneendra K. Yalavarthy has now fulfilled all of the requirements for the Doctor of Philosophy degree from the Thayer School of Engineering, Dartmouth College, and will formally graduate at Commencement on June 8, 2008. (Dartmouth College awards degrees once per year in June.).

If I can supply additional information, or be of further assistance, please do not hesitate to call me at 603-646-3801.

Sincerely,

Daryl A. Laware

Not valid without the impressed seal of the Thayer School of Engineering

Letter from the Registrar about the Ph.D. completion

Critical computational aspects of near infrared circular tomographic imaging: Analysis of measurement number, mesh resolution and reconstruction basis

Phaneendra K. Yalavarthy[§], Hamid Dehghani[§,†], Brian W. Pogue[§] and Keith D. Paulsen[§]

[§]Thayer School of Engineering, Dartmouth College, Hanover, New Hampshire 03755
[†]School of Physics, University of Exeter, Exeter, UK EX4 4QL
Phaneendra.K.Yalavarthy@dartmouth.edu, Brian.W.Pogue@dartmouth.edu

Abstract: The image resolution and contrast in Near-Infrared (NIR) tomographic image reconstruction are affected by parameters such as the number of boundary measurements, the mesh resolution in the forward calculation and the reconstruction basis. Increasing the number of measurements tends to make the sensitivity of the domain more uniform reducing the hypersensitivity at the boundary. Using singular-value decomposition (SVD) and reconstructed images, it is shown that the numbers of 16 or 24 fibers are sufficient for imaging the 2D circular domain for the case of 1% noise in the data. The number of useful singular values increases as the logarithm of the number of measurements. For this 2D reconstruction problem, given a computational limit of 10 sec per iteration, leads to choice of forward mesh with 1785 nodes and reconstruction basis of 30×30 elements. In a three-dimensional (3D) NIR imaging problem, using a single plane of data can provide useful images if the anomaly to be reconstructed is within the measurement plane. However, if the location of the anomaly is not known, 3D data collection strategies are very important. Further the quantitative accuracy of the reconstructed anomaly increased approximately from 15% to 89% as the anomaly is moved from the centre to boundary, respectively. The data supports the exclusion of out of plane measurements may be valid for 3D NIR imaging.

OCIS codes: (170.0170) Medical optics and biotechnology; (100.3190) Inverse problems; (170.3660) Light propagation in tissues; (170.4580) Optical diagnostics for medicine; (170.7050) Turbid media.

References and links

1. D. A. Boas, D. H. Brooks, E. L. Miller, C. A. DiMarzio, M. Kilmer, R. J. Gaudette, and Q. Zhang, "Imaging the body with diffuse optical tomography," IEEE Signal Process. Mag. **18**, 57-75 (2001).
2. B. W. Pogue, M. Testorf, T. Mcbride, U. L. Osterberg, and K. D. Paulsen, "Instrumentation and design of a frequency-domain diffuse optical tomography imager for breast cancer detection,". Opt. Express **1**, 391-403 (1997).
3. S. Srinivasan, B. W. Pogue, S. Jiang, H. Dehghani, C. Kogel, S. Soho, J. J. Gibson, T. D. Tosteson, S. P. Poplack, and K. D. Paulsen, "Interpreting hemoglobin and water concentration, oxygen saturation and scattering measured in vivo by near-infrared breast tomography," Proc. Natl. Acad. Sci. U.S.A. **100,** 12349-12354 (2003).
4. J. C. Hebden, A. Gibson, R. M. Yusof, N. Everdell, E. M. C. Hillman, D. T. Delpy, S. R. Arridge, T. Austin, J. H. Meek, and J. S. Wyatt, "Three-dimensional optical tomography of the premature infant brain," Phys. Med. Biol. **42**, 4155-4166 (2002).
5. N. Ramanujam, G. Vishnoi, A. H. Hielscher, M. E. Rode, I. Forouzan and B. Chance, "Photon migration through fetal head in utero using continuous wave, near infrared spectroscopy: clinical and experimental model studies," J. Biomed. Opt. **5**, 173-184 (2000).

6. S. R. Arridge, "Optical tomography in medical imaging," Inv. Problems **5**, R41-R93 (1999).
7. N. Polydorides1 and H. McCann, "Electrode configurations for improved spatial resolution in electrical impedance tomography," Meas. Sci. Technol. **13**, 1862-1870 (2002).
8. E. E. Graves, J. Ripoll, R. Weissleder, and V. Ntziachristos, "A sub-millimeter resolution fluorescence molecular imaging system for small animal imaging," Med. Phys. **30**, 901-911 (2003).
9. E. E. Graves, J. P. Culver, J. Ripoll, R. Weissleder, and V. Ntziachristos, "Singular-value analysis and optimization of experimental parameters in fluorescence molecular tomography," J. Opt. Soc. Am. A **21**, 231-241 (2004).
10. H. Xu, H. Dehghani, B. W. Pogue, R. Springett, K. D. Paulsen and J. F. Dunn, "Near-infrared imaging in the small animal brain: optimization of fiber positions," J. Biomed. Opt. **8**, 102-110 (2003).
11. J. P. Culver, V. Ntziachristos, M. J. Holboke and A. G. Yodh, "Optimization of optode arrangements for diffuse optical tomography: A singular-value analysis," App. Opt. **26**, 701-703 (2001).
12. H. Dehghani, B. W. Pogue S. P. Poplack and K. D. Paulsen, "Multiwavelength three dimensional near infrared tomography of the breast: Initial simulation, phantom and clinical results," App. Opt. **42**, 135-145 (2003).
13. H. Dehghani, B. W. Pogue, J. Shudong, B. Brooksby, and K. D. Paulsen, "Three dimensional optical tomography: Resolution in small object imaging," App. Opt. **42**, 3117-3128 (2003).
14. H. Dehghani, B. W. Pogue, S. Jiang, S. Poplack and K. D. Paulsen, "Optical images from Pathophysiological signals within breast tissue using three-dimensional near-infrared light," in *Optical Tomography and Spectroscopy of Tissue V*, B. Chance, R. R. Alfano, B. J. Tromberg, M. Tamura, and E. M. Sevick-Muraca, eds., Proc. SPIE **4955**, 191-198 (2003).
15. B. W. Pogue, S. Geimer, T. Mcbride, S. Jiang, U. L. Osterberg, and K. D. Paulsen, "Three-dimensional simulation of near-infrared diffusion in tissue: boundary conditions and geometry analysis for a finite element reconstruction algorithm," Appl. Opt. **40**, 588-600 (2001).
16. J. C. Hebden, H. Veenstra, H. H. Dehghani, E. M. C. Hillman, M. Schweiger, S. R. Arridge, and D. T. Delpy, "Three dimensional time-resolved optical tomography of a conical breast phantom," App. Opt. **40**, 3278-3287 (2001).
17. A. Gibson, R. M. Yusof, E. M. C. Hillman, H. Dehghani, J. Riley, N. Everdale, R. Richards, J. C. Hebden, M. Schweiger, S. R. Arridge, and D. T. Delpy, "Optical tomography of a realistic neonatal head phantom," Appl. Opt. **42**, 3109-3116 (2003).
18. J. P. Culver, R. Choe, M. J. Holboke, L. Zubkov, T. Durduran, A. Slemp, V. Ntziachristos, B. Chance and A. G. Yodh, "Three-dimensional diffuse optical tomography in the parallel plane transmission geometry: Evaluation of a hybrid frequency domain/continuous wave clinical system for breast imaging," Med. Phys. **30**, 235-247 (2003).
19. H. Jiang, K. D. Paulsen, and U. Osterberg, B. W. Pogue and Michael S. Patterson, "Optical image reconstruction using frequency domain data: simulations and experiments," J. Opt. Soc. Am. A **13**, 253-266 (1996).
20. M. Schweiger, S R Arridge, M Hiroaka and D T Delpy, "The finite element model for the propagation of light in scattering media: Boundary and source Conditions," Med. Phys. **22**, 1779-1792 (1995).
21. S. R. Arridge and M. Schweiger, "Photon-measurement density functions. Part2: Finite-element-method calculations," App. Opt. **34**, 8026-8037 (1995).
22. B. Brooksby, S. Jiang, C. Kogel, M. Doyley, H. Dehghani, J. B. Weaver, S. P. Poplack, B. W Pogue, and K. D Paulsen, "Magnetic resonance guided near infrared tomography of the breast", Rev. Sci. Inst. **75**, 5262-5270 (2004).
23. M. Schweiger and S. R. Arridge, "Optical tomographic reconstruction in a complex head model using a priori region boundary information," Phys. Med. Biol. **44**, 2703-2722 (1999).
24. H. Jiang, K. D. Paulsen, U. L. Osterberg, and M. Patterson, "Improved continuous light diffusion imaging in single and multiple target tissue-like phantoms," Phys. Med. Biol. **43**, 675-693 (1998).
25. Q. Zhu, N. G. Chen, and S. C. Kurtzman, "Imaging tumor angiogenesis by use of combined near-infrared diffusive light and ultrasound," Opt. Lett. **28**, 337 - 339 (2003).
26. M. Molinari, B. H. Blott, S. J. Cox, and G. J. Daniell, "Optimal imaging with adaptive mesh refinement in electrical impedance tomography," Physiol. Meas. **23**, 121-128 (2002).

1. Introduction

In the recent years, there has been a heightened interest in near-infra-red (NIR) optical tomography, for applications such as diagnostic breast cancer imaging [1-3] and for brain function assay [1, 4, 5]. In NIR tomography, the aim is to reconstruct interior optical properties of the tissue under investigation from a finite, yet incomplete set of transmission measurements taken at the tissue external boundaries. The reconstructed optical properties can give clinically useful information regarding tissue physiology and state, such as chromophore concentration and oxygen saturation. Typically, the optical source light used for excitation in

NIR studies is delivered through optical fibers and the transmitted light is also collected through the same or additional fibers which are in contact with the external surface of the tissue. Using these measurements, distributions of wavelength dependent absorption and/or scattering coefficients of the tissue are reconstructed using a model-based iterative algorithm. NIR studies have the advantage of being non-invasive, non-hazardous and can therefore be applied repeatedly to investigate functional changes in tissue over a prolonged time.

The dominance of light scattering in tissue at NIR wavelengths makes optical tomography inherently more difficult in the sense that light becomes diffuse within millimeters of travel, reducing the resolution of the reconstructed images. The image reconstruction procedure (i.e. the inverse problem) is non-linear, ill-posed and ill-conditioned [6] and to improve image reconstruction, the number of measurements are generally increased, to increase the amount of independent information. However due to experimental set-up constraints, such as the light collection strategy, source and detector fiber size and the imaging domain geometry, the total number of boundary measurements that can be taken from is often quite limited. In addition, there are constraints on the data acquisition and computation time that need to be considered for the specific application in which NIR light is used.

There have been some limited studies [7-11] on optimization of the fiber positions and measurements to get the best possible image resolution and contrast in NIR tomography. More specifically, Culver et. al [11] have showed that singular value decomposition (SVD) analysis of the weight matrix (also known as the Jacobian or sensitivity matrix) can be used to optimize detector placement in the reflectance and direct transmittance geometries of a homogeneous slab medium, and indicated that this could be extended to arbitrary geometries with heterogeneous tissue volumes. However, there remain many unknowns regarding the appropriate number of measurements required to get a sufficiently good image given the practical constraints of measurement number and image recovery algorithm, which is the subject of this paper. Furthermore, few studies have specifically investigated the effect of mesh resolution in both the forward and inverse calculations and very little is known about the quantitative increase in accuracy which is a direct result of mesh resolution and appropriate reconstruction bases. This work is an attempt to answer questions regarding the limited increase in number of measurements, more specifically benefits from the increased amount of information as well as investigating aspects that will have effects on image reconstruction procedure and resolution as well as the contrast of the reconstructed image.

In the present work, both a two dimensional (2D) circular domain and a three dimensional (3D) cylindrical geometry are investigated since most investigations to date have used either of these geometries for system and algorithm evaluation. Initially the effect of mesh resolution is investigated in the forward problem by comparing the Jacobian cross-section for various resolution 2D meshes to show improvements in numerical accuracy. Next the effect of increasing the number of measurements upon the resulting reconstructed image using singular-value analysis is investigated. Results regarding the optimized reconstruction basis are presented for the given 2D model, and the impact in the Root Mean Square (RMS) error of increased spatial sensitivity is presented as a function of increasing number of measurements. Finally a case-to-case analysis is shown by increasing the number of measurements in image reconstruction procedure and comparing the underlying image errors within the reconstructed images.

Since 3D problems have more degrees of freedom (unknown parameters), they are highly ill-determined as compared to the 2D problem. But NIR optical tomography utilizes the data from the 3D tissue volumes and therefore should be treated as a 3D imaging problem. Since light propagation in tissue is physically spread in all directions, 3D models are known to be an accurate prediction of the light fluence, whereas 2D models are simple yet inaccurate at predicting the interior fluence distributions [4, 12-17]. In order to further advance NIR optical tomography into a suitable and accurate clinical imaging modality, it is important to develop fully 3D imaging tools, yet, the major challenge in this task is to determine how to acquire large data sets which overcome the inherent limitation of the 3D problem being ill-determined

[18]. That is, to improve image reconstruction quality in 3D, the number of measurements can be increased as mentioned in 2D case, even here these measurements are quite limited.

For the chosen 3D cylindrical geometry, for example, acquiring experimental data from three different planes of fiber setup improves the reconstructed image of the entire domain as compared to one single plane of data, as there are greater numbers of measurements providing a larger set of sampling of the entire volume of interest. There are many strategies to increase measurement number and it is not clear which present the best improvement in the final image. Specifically, this work examines effects of different measurement strategies for 3D NIR tomography by presenting and quantifying the underlying effects of using a single plane of tomographic data as compared to three planes of tomographic data. Within the latter case, this work also presents, quantifies and discusses the benefits, limits and losses due to the measurement of in-plane data as compared to out-of plane data and will compare and contrast these data collection geometries from the prospective of gain and loss in the reconstructed image quality and respective computation time.

2. Methods

Conventional numerical methods for the forward calculations in NIR imaging use the Finite Element Method (FEM), which is considered as a flexible and accurate approach to modeling heterogeneous domains with arbitrary boundaries. Light transport in scattering tissue can be accurately described by the Diffusion Approximation (DA) to the Radiative Transfer Equation (RTE) [19]:

$$-\nabla.\kappa(r)\nabla\Phi(r,\omega)+\left(\mu_a(r)+\frac{i\omega}{c}\right)\Phi(r,\omega)=q_0(r,\omega) \tag{1}$$

where $\Phi(r,\omega)$ is the photon density at position r and modulation frequency ω (100 MHz in this work), and $\kappa = 1/[3(\mu_a + \mu_s')]$, the diffusion coefficient, where μ_a and μ_s' are the probabilities per unit length of absorption and transport scattering, respectively, and $q_0(r,\omega)$ is an isotropic source term. The Robin (Type III) boundary condition is used which best describes the light interaction from a scattering medium to the external air boundary [20]. The calculated boundary data values with a frequency domain system are the amplitude and phase of the signal, from which the diffusion and absorption coefficients can be simultaneously reconstructed.

For the inverse problem, a small change in boundary data is related to a small change in optical properties through the Jacobian matrix of values. The Jacobian matrix for reconstructing both the unknowns using two different data-types is calculated using the Adjoint-method [21], and has dimensions of (2×S×D) by (2×N), where S and D are the number of sources and detectors corresponding to each source respectively. N represents the number of nodes in the mesh used in the forward calculation. Here the Jacobian maps the changes in log amplitude and phase (2xSxD) to both absorption and diffusion changes at each node of the FEM model (2xN). The Jacobian which maps the change in detected signal to image space has four parts:

$$J=\begin{bmatrix} J1=\frac{\partial \ln I}{\partial \kappa}; & J2=\frac{\partial \ln I}{\partial \mu_a} \\ J3=\frac{\partial \theta}{\partial \kappa}; & J4=\frac{\partial \theta}{\partial \mu_a} \end{bmatrix} \tag{2}$$

In all our analysis, only the *J2* section is considered (dimension of (S×D) by N), which maps a small change in the absorption coefficient to a small change in measured log intensity of the signal. Since all kernels of the complete Jacobian show similar results, the discussion is limited to the results of *J2*, and shall henceforth be referred to as J.

In the reconstruction procedure presented, a modified Levenberg-Marquadt algorithm is used for calculating the estimates of μ_a, which is an iterative procedure [10] solving:

$$[\Delta\mu_a] = [\mathbf{J}^T\mathbf{J} + \lambda\mathbf{I}]^{-1}.\ \mathbf{J}^T\mathbf{b} \quad (3)$$

Here $[\Delta\mu_a]$ is an update vector for the absorption coefficient, **I** is the identity matrix and λ is a regularization parameter. Also, **b** = [**y** - $\mathcal{F}(\mu_a)$], where **y** is the measured (or simulated) heterogeneous boundary data and $\mathcal{F}(\mu_a)$ is the forward data for the current estimate of μ_a. In all of the presented work using simulated data, 1% noise was added to the amplitude, which is a typical noise observed in experimental data [2].

For the 2D analysis a circular model with a diameter of 86 mm centered at (0, 0) and with homogeneous optical properties of μ_a = 0.01 mm^{-1} and $\mu_s^{/}$ = 1.0 mm^{-1} is considered. The light collection/delivery fibers are arranged in a circular equally spaced fashion, where one fiber is used as the source while all other fibers are used as detectors, to give 'P' number of measurements (where P= M(M-1), where M is number of fibers). The source is a Gaussian source of Full Width Half Maximum (FWHM) of 3mm, and it is placed one transport scattering length within the external boundary.

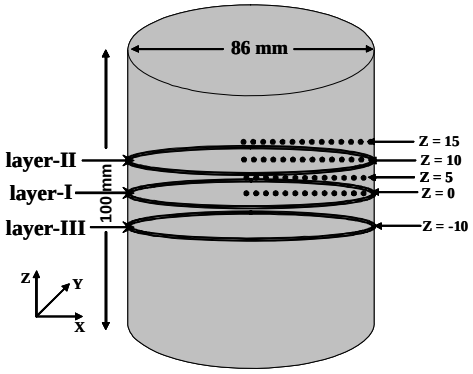

Fig. 1. Schematic diagram of data collection geometry used for the 3D cylindrical model.

For the 3D analysis, a cylindrical medium with a diameter of 86 mm having height of 100 mm centered at (0, 0, 0), with homogeneous optical properties of μ_a = 0.01 mm^{-1} and $\mu_s^{/}$ = 1 mm^{-1} is used (Fig. 1). The light collection/delivery fibers are arranged in a circular and equally spaced fashion and are in either a single plane of 16 fibers or 3 planes of 16 fibers per plane, totaling 48 fibers. Specifically three different strategies for data collection are considered:

(a). Single layer data: The 16 fibers are arranged in a circular and equally spaced fashion in a single Layer-I (Fig. 1), where one fiber is used at a time as the source while all other fibers are used as detectors, to give 240 (16x15) amplitude measurements.

(b). Three layers of in-plane data: The 48 fibers are arranged in a circular equally spaced fashion in all three layers (Layers-I, II & III in Fig. 1), giving 16 fibers per plane, where one fiber is used at a time as the source while only those fibers in the same "source fiber layer" are used as detectors, to give 720 (3x16x15) amplitude measurements.

(c). Three layers of out-of-plane: Same as above, except when one fiber is used at a time as the source, all other fibers in all three planes are used as detectors. This leads to 2256 (48x47) amplitude measurements.

For the image reconstruction process, an iterative update to the Jacobian matrix was computed, after each successive image estimation. At each iteration, the objective function was evaluated to estimate the projection error. The reconstruction procedure was then stopped when the projection error decreased by less than 3%.

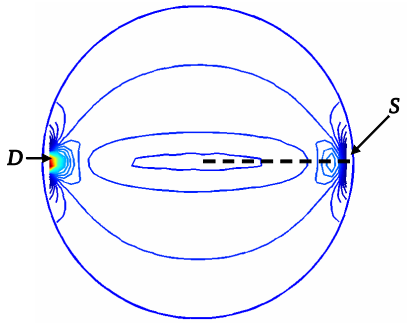

Fig. 2. The sensitivity (Jacobian) contour plot of log amplitude and μ_a for a source (S) and detector (D), which are diagonally opposite to each other as shown, calculated on a circular mesh of 9664 nodes.

2.1. 2D Mesh Resolution

In FEM the domain is divided into finite discretized sub-domains wherein the numerical accuracy and stability depends highly on this discretization (mesh resolution). Since the Jacobian represents the sensitivity of the detected signal to a small change in optical properties, the numerical accuracy of this value is crucial component of the image reconstruction problem, to study the effect of mesh resolution in 2D case, we choose different resolution meshes (with number nodes ranging from 150 to 4617 nodes) along with a high-resolution mesh of 9664 nodes for calculation of Jacobian. The Jacobian with a diagonally opposite source and detector is used, as shown in Fig. 2, from which the RMS error is calculated for each mesh with respect to the high-resolution mesh. The RMS error is calculated by interpolating the Jacobian of each mesh unto a uniformly distributed grid, allowing direct comparison of each result. Since the Jacobian represents the sensitivity of the detected signal to a small change in optical properties, the numerical accuracy of this value is a crucial component of the image reconstruction problem. Here the highest resolution mesh provides the most accurate and numerically stable solution, therefore the calculated RMS error indicates the numerical accuracy of each lower resolution mesh. The computation time taken for calculation of Jacobian and forward data is also noted as a function of mesh resolution. All the computations were carried out on Pentium-IV 2.5 GHz processor with 2 GB of RAM.

2.2. Singular-Value (SV) analysis

Singular-Value (SV) analysis for the Jacobian matrix is explained in detail elsewhere [10]. Using SV-analysis, the Jacobian is decomposed into:

$$\mathbf{J} = \mathbf{U}\mathbf{S}\mathbf{V}^{\mathrm{T}} \tag{4}$$

where, U & V are orthonormal matrices containing the eigenvectors of J and S is a diagonal matrix containing the singular values of J. Vectors of U and V correspond to the modes in the detection space and image space, respectively, while the magnitude of the singular values in S represents the importance of the corresponding eigenvectors in U and V. More nonzero singular values indicating more modes are effective in between the two spaces, which bring more detail and improve the resolution in the space. There are normally P nonzero singular values in the diagonal matrix and these values are sorted in decreasing order. Typically only those singular values above the noise level (in this study, 1 % noise in amplitude) are used, as they contain the only useful information in the matrix. Thus, it is possible to determine whether increasing the number of measurements gives rise to an increase in the number of useful singular values, which indicates improvement in the recovered images.

In 2D, this analysis was applied to two separate cases: (1) a homogeneous case with optical properties as given before, and (2) a heterogeneous case which mimics breast optical properties [22], with properties of fibro-glandular layer being μ_a = 0.003 mm^{-1} and $\mu_s^{/}$ = 0.95 mm^{-1} and having diameter of 66 mm and fatty layer surrounding it having μ_a = 0.006 mm^{-1} and $\mu_s^{/}$ = 1.1 mm^{-1} with a thickness of 20mm. The number of useful singular values above the noise level were calculated as the number of measurements was increased. The mesh that was found to have an optimum resolution from the previous analysis of the Jacobian (Sec. 2.1) was used for these analysis. For both these cases, the percentage of useful measurements with respect to total number of measurements was calculated as:

$$\text{Useful measurements (in \%)} = \left[\frac{\text{Useful number of singular values}}{\text{Total number of singular values}}\right] \text{x100} \quad (5)$$

Additionally, the effect of mesh resolution was studied for its impact on the number of independent boundary data points with an increase in number of measurements by calculating the rank of the Jacobian, which is defined as the maximum number of linearly independent rows/columns of a given matrix. As each row of the Jacobian indicates each measurement, the rank of the Jacobian indicates the total number of independent measurements.

Image reconstruction consists of two separate, yet equally important parts; the forward model and the inverse model. For the forward model, the mesh used in FEM needs to be such that to ensure numerical accuracy, as already discussed. For the inverse problem, however, the goal is to reduce the number of unknowns for the iterative update by the use of a reconstruction basis [23]. Therefore it is important to investigate the effects of various reconstruction basis degrees of freedom on the reconstruction. Various reconstruction basis can be used, such as second mesh basis [24], pixel basis [23] or adaptive [25, 26] . With this goal, a reconstruction basis was optimized for the given 2D problem by looking at the number of useful singular values for various pixel (reconstruction) basis. A linear pixel basis of having 100 (10 by 10) elements to 1600 (40 by 40) elements was used and the Jacobian was mapped to this basis for the analysis.

Table 1. The RMS error (with respect to the fine mesh of 9664 nodes) in the Jacobian cross-section from center to boundary, (indicated by dashed line in Fig. 2) at y = 0 mm. This is tabulated as a function of mesh resolution, or number of nodes in the mesh. Last two rows show the computation time taken for calculation the Jacobian and Forward data for 16 source-detector pairs (240 measurements). For the fine mesh of 9664 nodes the computation time for Jacobian and Forward data is 98.1 sec and 28 sec respectively.

Nodes	150	425	1360	1785	2683	3047	3569	4617
RMS error	60.56	27.84	5.06	4.84	2.57	2.15	1.85	1.07
Jacobian Computation Time (in Sec.)	1.1	2.5	7.8	10.1	15.2	17.8	20.8	38.1
Forward data Computation Time (in Sec.)	0.1	0.3	0.9	1.2	1.9	2.2	2.6	9.8

2.3. Reconstruction examples

In order to understand the effect of increasing the number of measurements on total sensitivity for a given 2D model the magnitude of the Jacobian was examined as a function of number of measurements. To achieve this, the horizontal cross-section of the whole Jacobian was plotted, which was summed up over all measurements, from center to boundary, and examined as the number of measurements increased. Since the Jacobian provides relative sensitivity, a cross-section plot was normalized in each case with respect to its magnitude at the center of the model and calculated as a function of number of measurements (56 to 4032). For the 3D model, the cross-section of the total Jacobian was normalized with respect to its magnitude at the center of the model (as in the 2D case), for each case of the three different data collection strategies. Finally, for the 2D model, only the absorption coefficient was

reconstructed with an increasing number of measurements of an object with absorption inhomogeneity at various positions of domain using log of amplitude data. A circular absorption anomaly of diameter of 10 mm was used having a contrast of 2:1 compared to its background. We used the optimal forward mesh along with optimal reconstruction basis for the reconstruction procedure. A total of 2 positions of absorption inhomogeneity were considered with it center at (x,y) of (0, 0), and (30, 0) for various number of measurements starting from 56 to 4032.

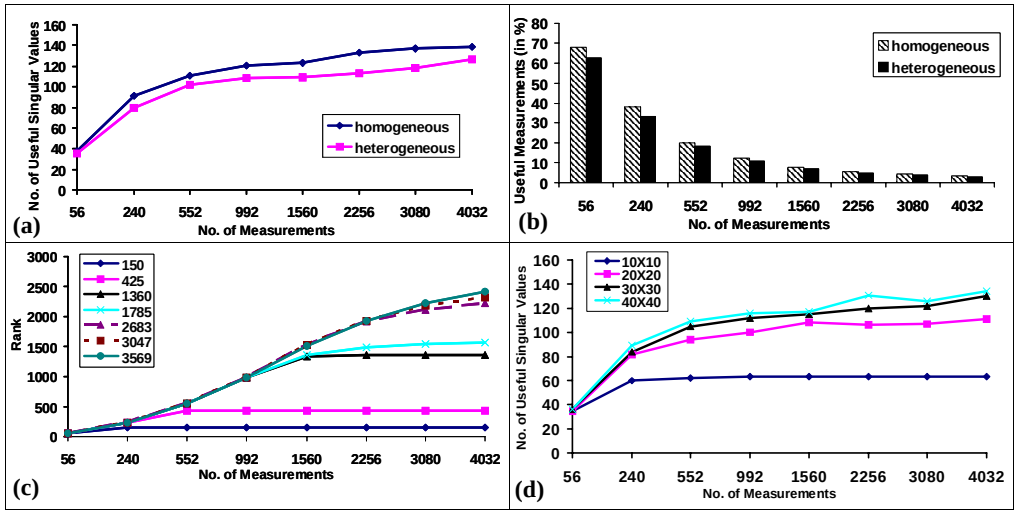

Fig. 3. Singular value analysis of homogeneous and heterogeneous 2D circular models. (a). Plot of the useful singular values versus number of measurements. (b). Plot of percentage of useful measurements versus the total number of measurements. (c). Plot of the Rank versus number of measurements is shown for a range of mesh nodes. (d). Plot of the number of useful singular values versus number of measurements is shown, for various reconstruction bases.

For the 3D case, a spherical absorption anomaly of diameter of 15 mm was assumed having a contrast of 2:1 compared to its background. A total of 3 positions of absorption inhomogeneity were considered with its center at x, y and z of (0,0,0), (30,0,0) and (30,0,10). The anomalies were reconstructed using the noise added data (1% in amplitude) simulated from the three different fiber location strategies. Full Width at Half-Maximum (FWHM) was measured for each of the peaks in the X-Y and Z-Y planes as well as the total computation time for reconstruction process.

Table 2. The number of useful measurements above the 1% expected noise level, is shown for the 2D circular and 3D cylindrical models, having 16 source and detector fibers with one or three planes of data collection. The two upper rows have only 1 plane of collection, whereas the 2nd last row has 3 planes of collection but not between the planes, and the last row has 3 planes of data collection with complete out of plane measurements.

	Number of Unknowns	Number of Measurements	Number of Useful Singular values	Useful measurements (%)	Magnitude of largest singular value
2D	1785	240	91	37.92	796.4
3D 1layer	20163	240	107	44.58	117.1
3D 3layer in-plane	20163	720	269	37.36	164
3D 3layer out-of-plane	20163	2256	328	14.54	304.6

3 Results

Figure 2 shows a sensitivity plot of log amplitude and the absorption coefficient using a 2D mesh with 9664 nodes for a source and detector which are diagonally opposite to each other.

Table-1 shows the RMS error with respect to the high resolution mesh in the horizontal cross-section (as indicated by the dotted line in Fig. 2) using the method described earlier. The RMS error calculated here was also calculated along different cross-sections of the model and a similar trend was seen. The mesh with 1785 nodes was found to have an RMS error of less then 5% as compared to the finest mesh.

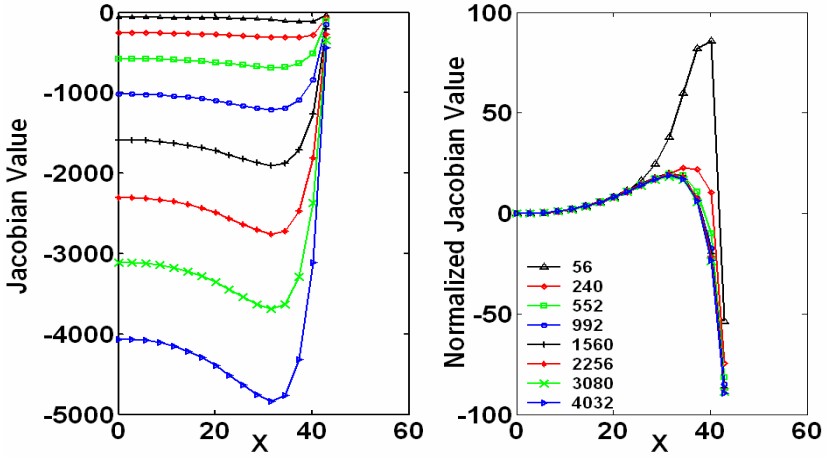

Fig. 4. Comparison of Jacobian cross-section with respect to measurement number. (a). The horizontal cross-sectional plot of the sum of 2D circular Jacobian matrix values, from center to the boundary at y = 0 mm. (b) The normalized sum of 2D circular Jacobian matrix values, with respect to the value at the center (at x = 0 mm, y = 0 mm). The legend gives number of measurements associated with each plot.

The 2D mesh with 1785 nodes was used for the calculation of the Jacobian and the expected noise level in the amplitude measurements was assumed to be 1%. For both the heterogeneous and homogeneous 2D cases, the number of useful singular values above the noise level were calculated, and the results are shown in Fig. 3(a). Figure 3(b) is a bar chart showing useful measurements in percentage [given by Eq. (5)] for each set of measurements. Figure 3(c) is a plot of the rank of the Jacobian versus the total number of measurements for meshes having different resolution starting from 150 to 3569 nodes versus number of measurements. The Jacobian calculated is also mapped onto a reconstruction (pixel) basis ranging from 10×10 to 40×40. The number of useful singular values as function of pixel basis elements, for each set of measurements, are plotted in Fig. 3(d). Finally, for the 2D case, Fig. 4 shows the total sensitivity distribution at the mid-axis cross-section, as a function of the number of measurements. Table 2 shows the number of useful singular values of the 3D model Jacobian which are above the noise level (1%) for the three different strategies, and indicates the effective number of measurements which will be contributing to the reconstructed image space and quality. The number of useful singular values is higher for the three layer out-of-plane strategy. The useful percentage of measurements is higher for the 3D single plane of data, whereas the condition number is very high for the 3D three-layer out of plane case. Similar data is also included using the 2D circular geometry for comparison purposes, with 240 measurements and the same corresponding optical properties as the 3D model.

The plots of the 3D Jacobian magnitude as normalized to the value at the center of the model are shown in Fig. 5. These plots shows that, all the three strategies of data collection in 3D are hypersensitive (in X & Y direction) at the boundary. Moreover this is pronounced for the 3D single-plane case. In the Z-direction (not shown) it was found that, as expected that, the sensitivity decreases as the position moves from centre to boundary for all the three cases.

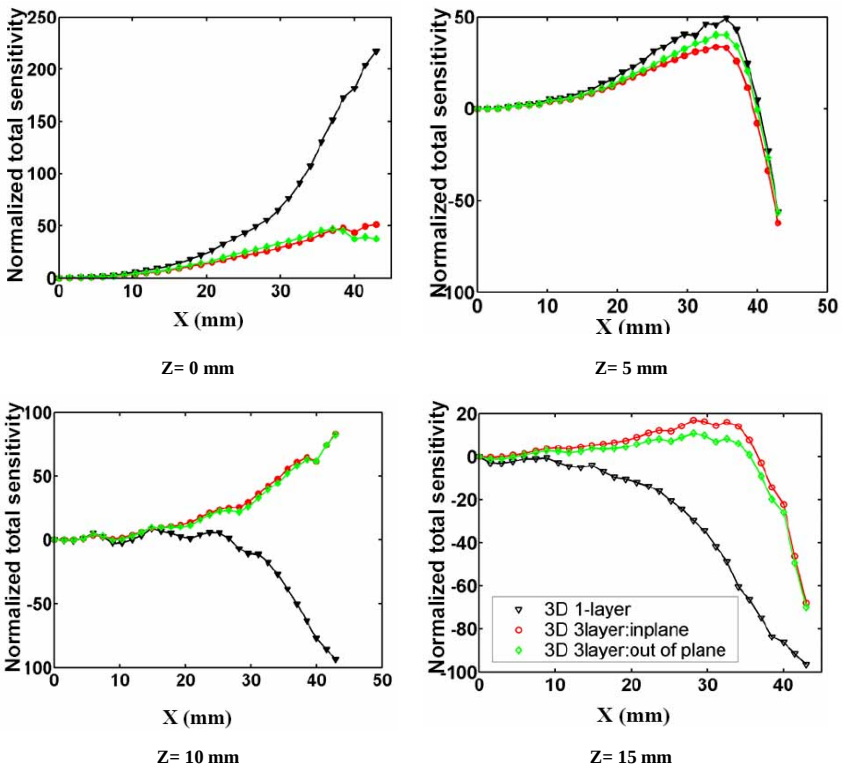

Fig. 5. The normalized cross-section in the X-Y plane, showing the total sensitivity across the dotted line in Fig. 2, from x= 0 mm to x = 43 mm (center to boundary) at Y = 0 mm normalized with respect to the sensitivity at the origin, (i.e. X = 0, Y = 0 & Z = 0 mm).

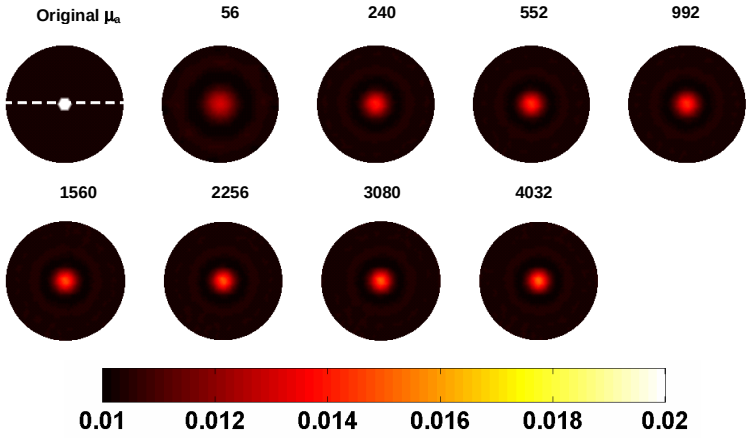

Fig. 6. The reconstruction of the μ_a distribution, using noisy simulated data of log amplitude, for a circular object with an absorbing inhomogeneity at the center. Different numbers of measurements were used as denoted above each image, ranging from 56 up to 4032 data points. The forward mesh was 1785 nodes and the pixel basis consisted of 30x30 elements. The original μ_a distribution is shown as the first image.

The 2D reconstruction of a circular object with a centralized absorption anomaly of diameter of 10mm using different number of measurements, along with original μ_a distribution, is shown in Fig. 6. The contrast of the inhomogeneity to background is 2:1 and

for these reconstructions a pixel basis of 30 x 30 elements is used, with a forward mesh consisting of 1785 nodes. Figure 7 shows the plot of logarithm of rms error in the horizontal cross-section (as sown by dotted line in Fig. 6) as a function of measurement number. The legend of the figure gives the position of the inhomogeneity (diameter of 10mm).

Table 3 summarizes the results of the 3D reconstruction. Figure 8(a) shows the reconstructed absorption coefficient distributions for a spherical absorption inhomogeneity (diameter of 15 mm) located at (0, 0, 0) with a contrast of 2:1 to background, using the data collected from the three strategies. Figure 8(b) shows the results of the same effort with a spherical inhomogeneity located near to the boundary (30, 0, 0). The results show that the quantitative values of the anomaly increases as the anomaly is moved from centre to boundary in X & Y direction. The anomaly for this location is reconstructed with 89% quantitative accuracy compared to the 15% accuracy for central location. Finally the reconstructed absorption coefficient distribution for a spherical absorption inhomogeneity (diameter - 15 mm), which is centered at (30, 0, 10) are shown in Fig. 8(c) and it can be seen that single layer case reconstructed the anomaly in the wrong location. Here, both the in-plane and out-of-plane strategies are able to give up to 84% quantitative accuracy (Table 3).

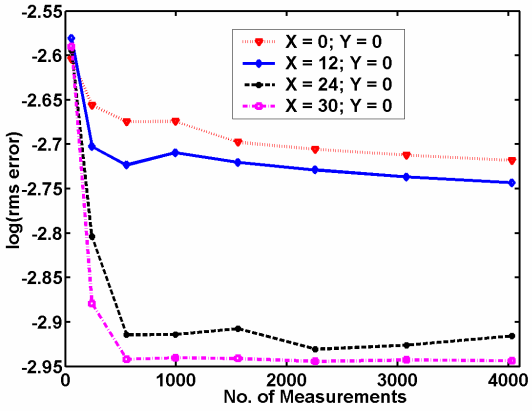

Fig. 7. A plot of logarithm of rms error in the horizontal cross-section of μ_a at y = 0 (as shown in original μ_a distribution of Fig. 6) versus number of measurements for various positions of an absorption inhomogeneity. These calculations used 1785 nodes in the mesh of the forward problem and a pixel basis of 30x30 elements in the reconstruction.

4 Discussion

The decrease in the RMS error for the horizontal cross-section of the 2D Jacobian for a given source-detector (diagonally opposite each other) for a mesh greater than 1500 nodes as compared to 9664 nodes (Table-1) is below 5%. It should be noted that the other kernels of the Jacobian, for example J3 ($\frac{\partial\theta}{\partial\kappa}$), showed better accuracy (2%) when the mesh had 1785 nodes or greater. As with many iterative reconstruction problems, optical tomography requires repeated forward calculations and re-computation of the Jacobian, thereby increasing mesh resolution which further implies increase in computational time, which is clearly evident from last two rows of Table 1. A computation limit of 10 seconds per iteration, lead to a choice of mesh resolution with 1785 nodes for the forward problem in two-dimensional case, and extending this same level of resolution to 3D would require nearly 80,000 nodes, which is near the limit of what can be done computationally. Thus much of the 2D study presented here was run at the level of 1785 nodes. Since the computation of the Jacobian using the FEM relies on the discretization of the domain and the accuracy of the numerical model depends on

Table 3. The computation time and accuracy of the 3D reconstruction is shown for the three different data collection strategies, along with three different locations of the anomaly for each.

Strategy	Position of anomaly (original)	Iterations	Total Computation time (s)	Quantitative accuracy (%) of the reconstructed anomaly	FWHM along X-axis (mm)	FWHM along Z-axis (mm)
3D: 1layer	(0,0,0)	11	3179	15%	16.1	25.2
	(30,0,0)	14	4046	89%	17.2	23.3
	(30,0,10)	10	2890	-	-	-
3D 3layer in-plane	(0,0,0)	14	8022	14%	16.5	25.3
	(30,0,0)	14	8022	80%	13.1	18.7
	(30,0,10)	12	6876	110%	11.2	18.6
3D 3layer out-of-plane	(0,0,0)	6	10926	11%	23.7	24.1
	(30,0,0)	9	16389	78%	13.6	18.9
	(30,0,10)	8	14568	84%	13.2	18.7

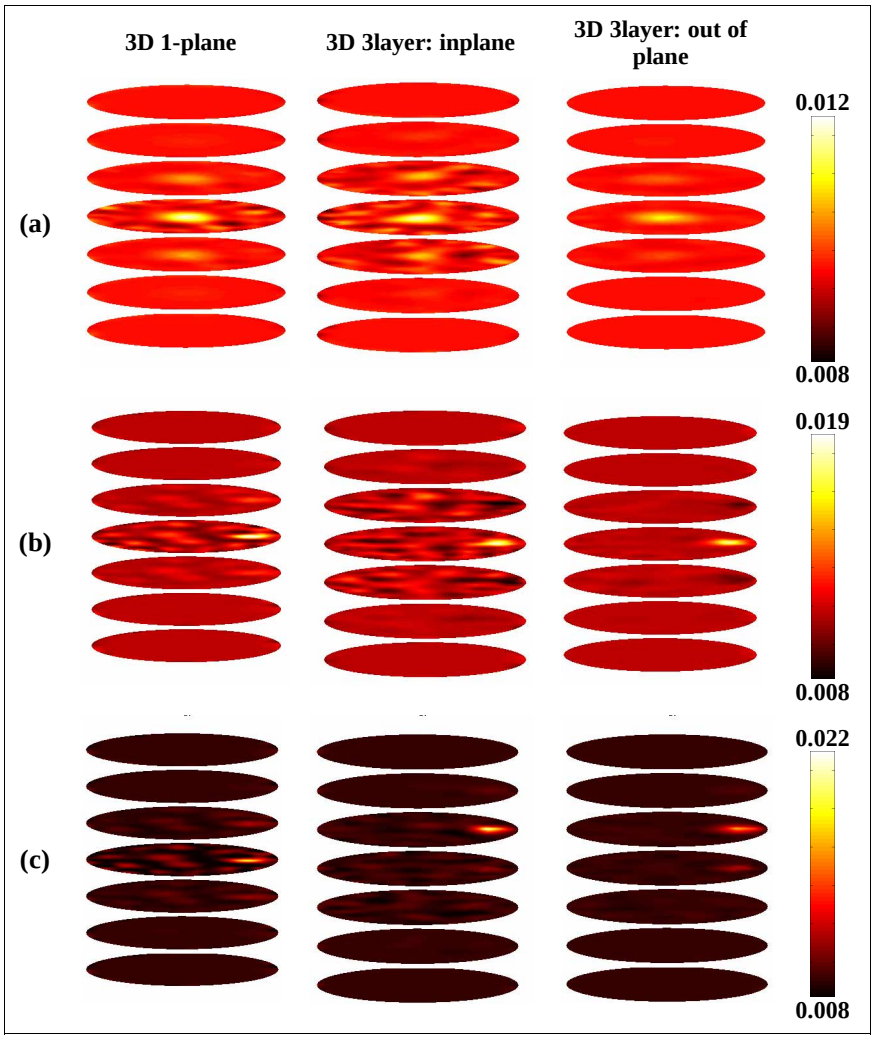

Fig. 8. The reconstructed absorption coefficient distribution for the cylindrical object with a spherical absorption inhomogeneity (diameter of 15mm and contrast 2:1 with respect to background) located at x, y and z locations (a) (0,0,0), (b) (30,0,0) and (c) (30,0,10). The three columns of images show the results achieved with the three different data collection schemes.

this discretization and the associated integration of the shape functions, the resolution of the mesh and the associated optical properties will affect these results. For example, if the absorption coefficient is much smaller, then lower resolution meshes may be adequate, as the problem becomes more energy conserving, whereas for a higher absorption or scattering problem, a higher resolution mesh will be needed to ensure numerical accuracy within each FEM element for a lossy problem. Note also that for spectral reconstruction [3] with six wavelengths data, each iteration takes about 30 sec for 1785 nodes mesh.

For a heterogeneous or homogeneous 2D case, number of useful singular values, which are above the noise level (1% in amplitude) showed similar trends and behavior with increasing numbers of measurements, as evident from Fig. 3(a). Further, the percentage of useful measurements (useful singular values) drops exponentially as the number of measurements is increased, Fig. 3(b). It is worth noting that for a heterogeneous model, since light propagation becomes more complex, and in this case more diffusive, the total number of useful measurements is slightly lower than that of homogeneous model. In this work, useful singular values are defined as the ones which are above noise level (1%). This is used only for optimizing the parameters used in the reconstruction procedure, but in the actual reconstruction procedure, regularization is used to reduce the condition number.

Next, the effect of the 2D mesh resolution was investigated, for it's impact upon the number of independent available measurements. From Fig. 3(c), it is evident that if the degrees of freedom (mesh resolution) in the forward problem is less than the total number of measurements, then increasing the number of measurements does not increase the number of independent measurements (i.e. the rank), since the rank is predominantly restricted by the number of nodes in the mesh. For example, given a system from which only 240 measurements are available, any mesh which has a resolution of 240 nodes or more will give the same number of independent measurements. Therefore no additional measurements can be gained in terms of independent information by increasing the mesh resolution. Given a 2D mesh of 1785 nodes, for example, no considerable gain in independent data can be obtained when the number of measurements are increased above 1560 (40 source and detectors). At this point, it will be worth remembering that, in real time there is a physical constraint on number of measurements, because of the physical geometry and fiber size. To take an example, for a circular test phantom of 86 mm diameter and fiber of 6 mm diameter, no more than 40 fibers (which corresponds to 1560 measurements) can be arranged around the outer boundary of domain. However this issue becomes more important perhaps for non-contact imaging systems in which the number of source-detector locations can be arbitrarily large.

Using a 2D mesh of 1785 nodes, the effect of an increase in the reconstruction (regular pixel) basis resolution upon reconstruction was investigated [Fig. 3(d)]. An increase in pixel basis elements increases the number of useful singular values, but there is no significant improvement in the pixel basis from 30×30 (900 elements) to 40×40 (1600 elements). This is very interesting, since one would assume that fewer degrees of freedom for the inverse problem would produce a better solution. But although the problem may become better posed, the rank will be similar to that shown in Fig. 3(d). However, these results indicate the best possible resolution obtainable is by using the 40 x 40 pixel basis and again these results will be dependent on the physical problem dimension and level of complexity. Figure 4 shows that increasing the number of measurements for a 2D model increases the sensitivity of the problem, as evident from magnitude plot of the Jacobian (calculated from 1785 nodes mesh). Also shown in Fig. 4 is a normalized plot, relative to the central value, and indicates that for fewer number of measurements, the sensitivity is maximal near the boundary and lower at the center, as expected. By increasing the number of measurements, eventually the hypersensitivity near to the boundary reduced and the sensitivity became uniform regardless of distance from boundary. Finally, it is observed that increasing the number of measurements above 552 (24 sources and detectors) did not result in any further improvement in the sensitivity distribution.

For the 3D model, Table 2 shows that three layers of out-of-plane measurements yields a higher number of useful singular values, but the useful percentage of the total measurements

was below 15%. An increase in number of measurements means more data acquisition time and more computation time. Non-linear iterative image reconstruction procedures in NIR imaging use repeated calculation of the forward data. Therefore increasing the number of sources and measurements substantially increases the computation time. In comparing the three layer in-plane and three layer out-of-plane data collection strategies, having more than three times the measurements in the latter case improves the number of useful singular values only by 22%. The improvement in the number of useful singular values is not significant if the data acquisition time is considered as well as the computation time. The magnitude of the singular values indicates the importance of that eigenvector in the image space, which is directly related to reconstructed image contrast that can be achieved. To compare the magnitude of the largest singular value, even though it is at its highest for the three layer out-of-plane strategy, it should be noted that only 3 of the singular values are above 164 (magnitude of largest singular value of 3D 3layer-in-plane), indicating that there would not be dramatic differences in the reconstructed image contrast in both these cases. If the magnitude of largest singular value in 2D and 3D are compared, in 2D the magnitude is higher, whereas the number of useful singular values are lower than 3D, indicating that the modes that contribute to image space are fewer and the quality of the reconstructed image in 2D will be lower than 3D. Even though magnitude of the singular values dictate the contrast, the singular vectors associated with it will tend to affect the reconstructed image quality. The magnitude of the largest singular value in the 3D 3layer cases are the same because of the smoothness of the singular vectors in the case of 3D 3 layer: out-of-plane, the reconstructed image quality is better than the rest cases (Fig. 8). The FWHM analysis also confirms this.

It should be noted that there is always a trade-off between image quality and computation time. Therefore having out-of-plane data increases the image resolution, but taking into consideration the overall computation time, this improvement is perhaps not so significant. The computation time per iteration is high in the case of out-of-plane data (computation time per iteration: 2D problem – 70 sec; single-layer – 289 sec; three layer: in-plane – 573 sec; three layer: out-of-plane – 1821 sec).

Figure 5 indicates that for the 3D model with a single measurement plane case, the total sensitivity is higher near the boundary, as compared to the three plane data case and by increasing the number of measurements the sensitivity near the boundary is decreased. The results show that although the sensitivity is still higher at the boundary with three planes of data acquired, there is no significant difference in the sensitivity pattern observed between three layer in-plane or out-of-plane strategies.

Since only one component of the full Jacobian matrix, *J2* in Eq. (2), has been examined here, images have also been reconstructed for μ_a using log amplitude data for a 2D forward mesh of 1785 nodes and a reconstruction basis 30 by 30 pixel basis. Noisy simulated data were generated for various radial positions of the absorption inhomogeneity with a contrast of 2, relative to the background and having a diameter of 10 mm. The log of RMS error was calculated as the difference in the original and the reconstructed horizontal cross-sections of each image (Fig. 6) as a function of number of measurements and these were plotted in Fig. 7. The results show that, as evident from Fig. 7, although there is a decrease in the RMS error as the number of measurements is increased, the improvement in the reconstructed images is not significant for measurements greater than 552 (corresponding to 24 fibers). However, for a central anomaly, the RMS error continued to decrease with increasing number of measurements, whereas for an anomaly near the boundary the RMS error does not improve more than 0.5% with respect to 552 measurements.

To study the effect of data collection strategies on the 3D reconstructed image, the FWHM (Full Width at Half Maximum) of the peaks for all the reconstructed cases have been calculated and compared, Table 3. As the inhomogeneity moves from the centre towards the boundary, the FWHM reduces for both of the three layer cases and it remains approximately the same for the single layer case. For example, when the inhomogeneity is placed at (30,0,0), Fig. 8(b), the FWHM (in the X-cross section) values for single layer is 17.2mm and for the three–layers in-plane and out-of-plane strategies is 13.1mm and 13.6mm respectively. It is

evident from the reconstruction examples that the quantitative values of the inhomogeneities increase as the object moves from the centre to boundary, which is in close match with Jacobian analysis above. Reconstruction of absorption using single layer data, is not accurate, in a case where the anomaly is not presented in the imaging plane, such a case results are presented in Fig. 8(c). In this case, single-layer reconstructed image shows the inhomogeneity at a false position (reconstructed: (30,0,0); actual: (30,0,10)). Most of the 3D NIR studies indicate that, the quantitative accuracy of the images will be poor due the partial volume effect in three dimensions[13,16,17] and these quantification can be greatly improved by the use of more sophisticated regularization and the addition of penalty terms into Eq. (3).

5 Conclusions

In this investigation, the mesh resolution and numerical accuracy in the 2D and 3D forward problems were examined, using specific data-collection geometries. Several choices such as domain size, optical properties and anomaly position and size were kept fixed, relative to typical breast cancer imaging situations. It was shown that increasing the number of measurements increases the total amount of information available, and these specifically enhance the recovery of the central region of the model, regardless of dimensionality. Further, by increasing the number of measurements, the rank of the problem (i.e. amount of independent useful information) may not increase if the degrees of freedom (i.e. number of nodes in the mesh) are low. Reconstruction basis plays an important role in the inverse problem and it has been found that a pixel basis of 30×30 is optimal for a typical breast imaging problem.

More specifically for a 3D imaging problem, this work has shown the benefits and drawbacks of multi-plane data collection as well as the use of in-plane versus out-of-plane data measurements strategies. It has been shown that the use of single-plane of data in a 3D model is perhaps adequate, in terms of image quality, computation time and data collection time, if the anomaly being imaged is within the plane of measurements. However, if prior information such as plane of interest is not known, it has been shown that multi-plane data is crucial. The use of in-plane and out-of-plane data has been addressed and is shown that although the use of out-of-plane data provides more independent and useful information for image reconstruction, the magnitude of this additional information does not provide enough advantages worth the data acquisition and image computation time.

Finally it is worth noting that the 3D study has been limited to 16 source/detection fibers per plane. The addition of more measurement fibers and/or investigation of a different image reconstruction basis, such as those performed for the 2D problem can be easily extended for the presented 3D problem. The technique and analysis described here can be used as a tool to improve resolution and contrast, given prior information about the domain being imaged. This specific study was undertaken to better understand the parameters and capabilities of existing breast imaging system at Dartmouth and to focus on software improvements which may increase its recovery of lesion information.

Acknowledgments

P.K.Y. acknowledges support from the US DOD for Breast Cancer predoctoral fellowship (BC050309). As well, this work has been sponsored by the National Cancer Institute through grants RO1CA69544, PO1CA80139, and the DOD through DAMD17-03-1-0405.

Weight-matrix structured regularization provides optimal generalized least-squares estimate in diffuse optical tomography

Phaneendra K. Yalavarthy[a] and Brian W. Pogue
Thayer School of Engineering, Dartmouth College, Hanover, New Hampshire 03755

Hamid Dehghani
School of Physics, University of Exeter, Stocker Road, Exeter EX4 4QL, United Kingdom

Keith D. Paulsen
Thayer School of Engineering, Dartmouth College, Hanover, New Hampshire 03755

(Received 20 December 2006; revised 29 March 2007; accepted for publication 29 March 2007; published 17 May 2007)

Diffuse optical tomography (DOT) involves estimation of tissue optical properties using noninvasive boundary measurements. The image reconstruction procedure is a nonlinear, ill-posed, and ill-determined problem, so overcoming these difficulties requires regularization of the solution. While the methods developed for solving the DOT image reconstruction procedure have a long history, there is less direct evidence on the optimal regularization methods, or exploring a common theoretical framework for techniques which uses least-squares (LS) minimization. A generalized least-squares (GLS) method is discussed here, which takes into account the variances and covariances among the individual data points and optical properties in the image into a structured weight matrix. It is shown that most of the least-squares techniques applied in DOT can be considered as special cases of this more generalized LS approach. The performance of three minimization techniques using the same implementation scheme is compared using test problems with increasing noise level and increasing complexity within the imaging field. Techniques that use spatial-prior information as constraints can be also incorporated into the GLS formalism. It is also illustrated that inclusion of spatial priors reduces the image error by at least a factor of 2. The improvement of GLS minimization is even more apparent when the noise level in the data is high (as high as 10%), indicating that the benefits of this approach are important for reconstruction of data in a routine setting where the data variance can be known based upon the signal to noise properties of the instruments. © *2007 American Association of Physicists in Medicine*. [DOI: 10.1118/1.2733803]

Key words: near infrared, diffuse optical tomography, inverse problems, least-squares minimization

I. INTRODUCTION

Image reconstruction methods used in diffuse optical tomography (DOT) are mainly dependent on the type of data, the diffuse light model, and the number of available anatomical/spectral priors. There are numerous reconstruction techniques available in the literature depending on the application.[1–5] Yet despite the volume of work in this area there is no single investigation with a direct comparison of the least-squares (LS) minimization techniques using the same implementation scheme, especially in terms of data noise level and complexity in the test fields. Most of the comparisons in the literature have been in terms of implementation of minimization and convergence rates of one or two techniques at hand.[1–5] This work addresses this problem and compares minimization methods (more specifically different types of regularization) with the same implementation scheme for a direct quantitative comparison. Moreover, usage of weight matrices in the regularization which include the variance and covariance properties of data and image space are extensively explored here. A new covariance form borrowed from meteorological studies is introduced and proven to be effective for reconstructing highly noisy data in the generalized theoretical frame work.

Near infrared DOT involves reconstructing images of optical properties from transmission measurements using wavelengths from 650–1000 nm to interrogate tissue.[1,6–8] Optical absorption and scattering images obtained using multiple wavelengths can be used to estimate tissue hemoglobin, water concentration, scattering amplitude, and scattering power.[8] To overcome the inherent low-spatial resolution in DOT, there is a considerable interest in developing hybrid systems,[9–27] which use the spatial mapping of one system as the template for DOT. Image formation from the data collected by these (stand-alone/hybrid) systems involves solving an inversion problem. This article describes LS minimization techniques to solve the inverse problem and to quantitatively compare their performance in a systematic series of simulations. The inverse problem (image reconstruction procedure) in DOT is known to be a nonlinear, ill-posed, and ill-determined problem,[2] and to solve such a problem, a regularization term must be added to constrain the solution space in order to obtain a meaningful image. There are many

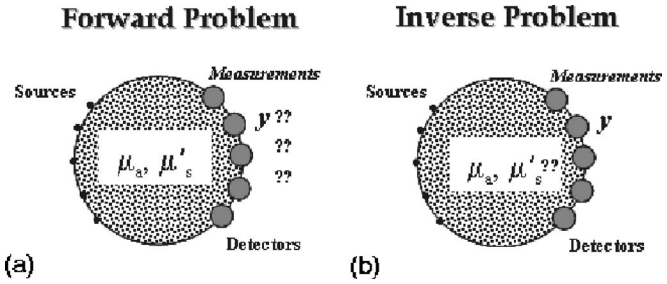

FIG. 1. An illustration of the forward and inverse problem in diffuse optical tomography is shown (see Ref. 64), where (a) the data y is estimated given values of μ_a and μ_s' and source/detector positions. In the inverse problem (b), the values of μ_a and μ_s' must be obtained given a set of measurements (y).

regularization methods available in the literature and this work focuses on the fact that most LS techniques presented in the literature can be encompassed within a generalized theoretical framework, which includes a regularization matrix that is based upon weights from the data and parameter variances. Note that Appendix A gives the terminology used in this work along with definitions of symbols.

Because of the interest in using spatial information derived from conventional imaging modalities in the DOT inverse problem, a number of methods have been presented in the literature.[9–27] These techniques were initially proposed by Barbour *et al.*[9] and Schweiger *et al.*[13] and used in to improve the quantitative outcome of reconstructed images. Ntziachristos *et al.*[14] used the magnetic resonance (MR) information to divide the imaging domain into tumor and nontumor regions to make the problem better posed. Li *et al.*[17] used an x-ray tomosynthesis volume to segment the breast into different subregions and used different regularization parameters depending on the size of the subregions. Recently Guven *et al.*[24] proposed a Bayesian frame work to include spatial prior information in an effective way which will not bias the image reconstruction problem to imperfect anatomical priors. Pogue and Paulsen,[10] Brooksby *et al.*[18,21,25] and Yalavarthy *et al.*[26] have extended these approaches for the use of anatomical prior information in which, depending on the connectivity and size of the subregion, the regularization term was scaled. Even though the effect of imperfect spatial prior information on the image reconstruction is a very active research area,[23,24,26] it was assumed here that the spatial priors were perfect. Other ongoing studies are examining this more complex issue.

II. DOT FORWARD PROBLEM

DOT involves solving a model (forward) and estimation (inverse) problem, sequentially as illustrated in Fig. 1. In this section, the forward problem is described, which involves generating the measurement data, for a given set of optical property estimates within the tissue, using a finite element solution to the diffuse transport equation.

Light propagation in a turbid elastic-scattering media, like tissue, is treated as "neutral-particle transport" rather than "wave propagation" and in the frequency domain, the diffusion equation is used, which is given by[2,28]

$$-\nabla \cdot D(\mathbf{r})\,\nabla \Phi(\mathbf{r},\omega) + [\mu_a(\mathbf{r}) + i\omega/c]\Phi(\mathbf{r},\omega) = Q_o(\mathbf{r},\omega), \tag{1}$$

where $\Phi(\mathbf{r},\omega)$ is the photon density at position $\mathbf{r}$ and the light modulation frequency is given by ω ($\omega=2\pi f$, in this work $f=100$ MHz). The isotropic source term is represented by $Q_o(\mathbf{r},\omega)$ and the speed of light in tissue by c, which is constant here. $\mu_a(\mathbf{r})$ is the optical absorption coefficient and $D(\mathbf{r})$ is the optical diffusion coefficient, which is defined as

$$D(\mathbf{r}) = \frac{1}{3[\mu_a(\mathbf{r}) + \mu_s'(\mathbf{r})]}, \tag{2}$$

where $\mu_s'(\mathbf{r})$ is the reduced scattering coefficient, which is defined as $\mu_s'=\mu_s(1-g)$. μ_s is the scattering coefficient and g is the anisotropy factor. A Robin (type-III) boundary condition is applied to model the refractive-index mismatch at the boundary.[29] The measured data for a frequency domain system are the amplitude and phase of the transmitted signal. If F is the forward model [finite element method (FEM) in here] which gives the fluence at every point, then the modeled data $G(\mu)$ can be obtained by sampling the forward model at the boundary given internal spatial distributions of optical properties and source-detector locations, where μ represents the parameters $\{\mu=[D(\mathbf{r});\mu_a(\mathbf{r})]\}$,

$$G(\mu) = S\{F(\mu)\}. \tag{3}$$

The details of the FEM formulation of the forward model are given in Refs. 30–32. The results presented are restricted to frequency-domain data, more specifically data (y) is the natural logarithm of the amplitude (A) and phase (θ) of the frequency-domain signal. Defining A and θ in terms of modeled data, $A=\sqrt{\mathrm{Re}\{G(\mu)\}^2+\mathrm{Im}\{G(\mu)\}^2}$ and $\theta=\tan^{-1}(\mathrm{Im}\{G(\mu)\}/\mathrm{Re}\{G(\mu)\})$. The Jacobian ($J$), which gives the rate of change of modeled data with respect to parameters, is calculated using the adjoint method.[30] Even though the actual parameters being estimated are $D(\mathbf{r})$ and $\mu_a(\mathbf{r})$, the results are presented in terms of $\mu_a(\mathbf{r})$ and $\mu_s'(\mathbf{r})$, which are spectroscopically more meaningful.

III. LEAST-SQUARES MINIMIZATION TECHNIQUES

This section outlines several different minimization schemes used in this work. These techniques are used to solve the inverse problem [Fig. 1(b)], which is achieved by minimizing the objective function (Ω) over the range of μ. Minimizing the objective function can be achieved by several different approaches. The most common approaches involve obtaining repeated solutions of the forward model and recomputation of the Jacobian (J) (and its inversion) at every iteration because of the nonlinear nature of the problem. There are also gradient-based optimization schemes available in the literature[33,34] to minimize the objective function which does not require an explicit inversion of the Hessian

matrix. In this work direct methods, known as full-Newton approaches,[2] are employed in minimization for all the regularization techniques used for a fair comparison. LS minimization has the effect of reducing high frequency noise, leading to smooth images of optical properties. Total variation methods and variants of this are used to obtain edge preservation in reconstructed images.[27,35] Solving the inverse problem using LS minimization can also be seen from a Bayesian prospective to obtain *maximum a posteriori* estimate.[24,36,37] A correlation between the Bayesian frame work and LS minimization techniques is given in Refs. 12, 38, and 39, but usage of the Bayesian frame work requires one to choose a particular noise model for both data and image space, which might not reflect the actual noise characteristics unless some prior information is available. Here, the emphasis is on LS minimization techniques with a focus on what the value of the regularization method can be. The LS methods are divided into two groups: (1) Without spatial priors and (2) with spatial priors.

A. Without spatial priors

1. Levenberg–Marquardt minimization

This approach is also known as a trust-region method[5,39] where experimental data is matched with modeled data iteratively.[40,41] The objective function for the DOT problem is defined as

$$\Omega = \{\|y - G(\mu)\|^2\}, \tag{4}$$

where $\mathbf{y}$ is the data and $G(\mu)$ is the modeled data. This equation is minimized by setting the first-order derivative equal to zero.

a. First-order condition. Minimizing Ω with respect to μ, which is achieved by setting $\partial\Omega/\partial\mu=0$,

$$\frac{\partial\Omega}{\partial\mu} = J^T\delta = 0, \tag{5}$$

where δ is the data-model misfit, $\delta=\mathbf{y}-G(\mu)$, J is the Jacobian, and T represents the matrix transpose operator.

b. Iterative update equation. Imagine a sequence of approximations to μ represented by μ_i, then using Taylor series on $G(\mu_i)$ and expanding around μ_{i-1} gives

$$G(\mu_i) = G(\mu_{i-1}) + J\Delta\mu_i + \ldots, \tag{6}$$

where $\Delta\mu_i=\mu_i-\mu_{i-1}$. Rewriting δ utilizing the first two terms of Eq. (6) (ignoring the rest, equivalently linearizing the problem) gives

$$\delta_i = y - G(\mu_i) = y - G(\mu_{i-1}) - J\Delta\mu_i = \delta_{i-1} - J\Delta\mu_i. \tag{7}$$

Rewriting Eq. (5) for the ith iteration

$$J^T\delta_i = 0. \tag{8}$$

Substituting Eq. (7) into Eq. (8) gives

$$J^T(\delta_{i-1} - J\Delta\mu_i) = 0. \tag{9}$$

Further simplification leads to the update equation

$$[\mathbf{J}^T\mathbf{J}]\Delta\mu_i = \mathbf{J}^T\delta_{i-1}. \tag{10}$$

When J^TJ is ill-conditioned, a diagonal term is added to stabilize the problem. In this case, the update equation becomes:

$$[\mathbf{J}^T\mathbf{J} + \alpha\mathbf{I}]\Delta\mu_i = \mathbf{J}^T\delta_{i-1}, \tag{11}$$

where $\Delta\mu_i$ is the update for the parameter in the ith step. Note that α monotonically decreases with iterations (always >0), and also that $\alpha\geqslant\|\delta\|^2$. The iterative method (or its modified version) is the commonly used minimization technique in DOT. It can be seen from Eqs. (10) and (11), when α becomes zero in Eq. (11) it becomes Eq. (10). It is also important to note that J^TJ is always symmetric, because $(J^TJ)^T=J^T(J^T)^T=J^TJ$. The advantage of using this method is in the simple choice of a regularization parameter (α). The limitations[41] of this method include:

- J^TJ must be positive definite.
- The initial guess (μ_0) should be close to the actual solution.
- The update equation [Eq. (11)] does not solve the first-order conditions unless $\alpha=0$.
- Since parameters are not involved in the minimization scheme, the inverse problem may be unstable.

Even though J^TJ is not positive definite in DOT, the Levenberg–Marquardt (LM) approach (or its modified version) has been used successfully in a number of instances.[2,6,7,28,42]

2. Tikhonov minimization

The generalized objective function[43,44] in the Tikhonov case includes parameters in the minimization function, which is defined as

$$\Omega = \{\|\mathbf{y} - G(\mu)\|^2 + \lambda\|L(\mu - \mu_0)\|^2\}, \tag{12}$$

where λ is the Tikhonov regularization parameter and L is a dimensionless regularization matrix (in this work). Here, μ_0 is the prior estimate of the optical properties, which in DOT has typically been obtained from calibrating the data.[45,46]

a. Choice of λ. Rewriting Eq. (12), normalizing both terms by their variances yields

$$\Omega = \left\{\frac{\|\mathbf{y} - G(\mu)\|^2}{(\sigma_y)^2} + \frac{\|L(\mu - \mu_0)\|^2}{(\sigma_{\mu-\mu_0})^2}\right\}, \tag{13}$$

where σ_y is the standard deviation in the data y and $\sigma_{\mu-\mu_0}$ is the standard deviation in the optical properties (or deviation from the prior estimate of optical properties). Note that the variance of data-model misfit [$\delta=\mathbf{y}-G(\mu)$] is assumed from the data, i.e., $(\sigma_\delta)^2=(\sigma_y)^2+(\sigma_{G(\mu)})^2$ with $(\sigma_{G(\mu)})^2=0$ because synthetic data was used. Multiplying Eq. (13) by σ_y^2 and comparing the result with Eq. (12) leads to

$$\lambda = \frac{(\sigma_y)^2}{(\sigma_{\mu-\mu_0})^2}, \tag{14}$$

which shows that the Tikhonov regularization parameter (λ) should be equal to the square of the ratio of the standard deviation in data to the standard deviation of the parameters.

This is a subtle yet important point, especially since this parameter is rarely defined this way, and is most commonly derived empirically.

b. First-order condition. Minimizing Ω with respect to μ, which is achieved by setting $\partial\Omega/\partial\mu=0$,

$$\frac{\partial\Omega}{\partial\mu}=J^T\delta-\lambda L^TL(\mu-\mu_0)=0. \tag{15}$$

c. Update equation. Rewriting Eq. (15) for the ith iteration leads to

$$J^T\delta_i-\lambda L^TL(\mu_i-\mu_0)=0. \tag{16}$$

Substituting Eq. (7) into Eq. (16) results in

$$J^T(\delta_{i-1}-J\Delta\mu_i)-\lambda L^TL(\mu_{i-1}+\Delta\mu_i-\mu_0)=0. \tag{17}$$

Further simplification leads to the iterative update equation

$$[\mathbf{J}^T\mathbf{J}+\lambda\mathbf{L}^T\mathbf{L}]\Delta\mu_i=\mathbf{J}^T\delta_{i-1}-\lambda\mathbf{L}^T\mathbf{L}(\mu_{i-1}-\mu_0). \tag{18}$$

Note that L^TL is symmetric. The constraint on the choice of L is that it must be positive definite.[44] In the absence of spatial priors, a common choice for the form of L is the identity matrix (I), which leads to the update equation

$$[\mathbf{J}^T\mathbf{J}+\lambda\mathbf{I}]\Delta\mu_i=\mathbf{J}^T\delta_{i-1}-\lambda(\mu_{i-1}-\mu_0). \tag{19}$$

Refer to Appendix B for an analysis of the Tikhonov regularization in terms of singular values. This regularization method is particularly common for ill-posed problems. The advantage of the method, is that it includes parameters within the minimization scheme which can be selected to improve the stability of the solution. Its limitations are that:

- it requires a prior opinion about the noise characteristics of the parameter and data spaces (for λ) and
- it does not take into account the individual variances of the data points/parameters, nor their covariances.

However, the simplicity of the approach makes it attractive for use in ill-posed problems. When the dynamic range of the data is large (as in DOT), incorporation of the maximum variance in the data will cause the minimization to bias the solution to specific data points (e.g. near the boundaries at source-detector locations in DOT). To reduce the effect of bias, one can employ a generalized least squares (GLS) minimization scheme, described in the next section.

3. GLS minimization

Generalized least squares minimization schemes have been proposed in the context of Tikhonov minimization in the literature,[1,5,38] in which there is some ambiguity in choosing the regularization parameter (λ). In here, a direct inclusion of weight matrices (which are inverses of covariance matrices) in the minimization scheme was employed to explicitly remove the dependence of reconstructed image quality on the choice of regularization parameter. This type of choice leads to an objective function[47,48]

$$\Omega=\{[y-G(\mu)]^TW_\delta[y-G(\mu)]+(\mu-\mu_0)^TW_{\mu-\mu_0}(\mu-\mu_0)\}, \tag{20}$$

where W_δ is the weight matrix for data-model misfit (δ) with $W_\delta=[\mathrm{cov}(\delta)]^{-1}$ (Appendix A-4 of Ref. 47). $W_{\mu-\mu_0}$ is the weight matrix for optical properties $(\mu-\mu_0)$ with $W_{\mu-\mu_0}=[\mathrm{cov}(\mu-\mu_0)]^{-1}$ (Appendix A-4 of Ref. 47). Explicit forms for these weight matrices are discussed later. Since both are inverses of covariance matrices, they are symmetric and positive definite.

a. First-order condition. Minimizing Ω with respect to μ, which is achieved by setting $\partial\Omega/\partial\mu=0$ produces

$$\frac{\partial\Omega}{\partial\mu}=J^TW_\delta\delta-W_{\mu-\mu_0}(\mu-\mu_0)=0. \tag{21}$$

b. Update equation. Similar to the Tikhonov approach, linearizing the problem leads to the iterative update equation[48]

$$[\mathbf{J}^T\mathbf{W}_\delta\mathbf{J}+\mathbf{W}_{\mu-\mu_0}]\Delta\mu_i=\mathbf{J}^T\mathbf{W}_\delta\delta_{i-1}-\mathbf{W}_{\mu-\mu_0}(\mu_{i-1}-\mu_0). \tag{22}$$

4. Choice of W_δ

Since simulated data were used here, in the formation of the weight matrix (covariance matrix), it was assumed that the cov(δ) is due to measurement error only, which yields[47]

$$W_\delta=[\mathrm{cov}(\delta)]^{-1}=\{\mathrm{cov}[y-G(\mu)]\}^{-1}=[\mathrm{cov}(y)]^{-1}, \tag{23}$$

where cov represents the covariance operator. In the simulation, typically one generates the forward data and adds noise to it to form synthetic data

$$y=G(\mu)+\sigma_y\eta, \tag{24}$$

where η is a random number vector. Typically, a random number generator which follows a normal distribution with zero mean and unity variance is used. Here, σ_y is the standard deviation of the data, assuming the noise is totally uncorrelated (white noise) in which case, the covariance matrix becomes[47]

$$[\mathrm{cov}(y)]_{ij}=\begin{cases}0 & \text{if } i\neq j\\ (\sigma_y)_i^2 & \text{if } i=j.\end{cases} \tag{25}$$

Since synthetic data were used in this article, the weight matrix for the data (W_δ) becomes diagonal. In the experimental case, one needs to collect an ensemble of data sets from which a covariance matrix can be computed. In this case, "N" data sets need to be collected using the same phantom (different homogeneous phantoms need to be used for different signal levels), where N needs to be a large number. From this ensemble of $\{y\}$,

$$\{y\}=\bar{y}+\{\tilde{y}\}, \tag{26}$$

where $\bar{y}$ is the true or mean value of data and $\{\tilde{y}\}$ is perturbation due to noise. This leads to

$$[\mathrm{cov}(y)] = [\mathrm{cov}(\tilde{y})] = \overline{\{\tilde{y}\}\{\tilde{y}\}^T} = \frac{\Sigma_{i=1}^{N} \tilde{y}_i \tilde{y}_i^T}{N} \tag{27}$$

substituting Eq. (27) in Eq. (23) gives W_δ. Note that in Eq. (23), it was assumed the cov(δ) is due to measurement error, which is also true in the case of experimental data, as the data are calibrated to remove the offset and match the modeled data.[45,46]

5. Choices of $W_{\mu-\mu_0}$

Here, two forms were considered to highlight the versatility of the procedure, even though many other forms of the covariance matrix can exist.

a. Analytical covariance form. Borrowed from the meteorological studies, assuming the parameter field obeys the Helmholtz equation, an analytical form (for one-dimensional infinite domain case) for the covariance matrix is[47]

$$[\mathrm{cov}(\mu-\mu_0)]_{ij} = (\sigma_{\mu-\mu_0})^2 \left(1 + \frac{r_{ij}}{l}\right) e^{-r_{ij}/l}, \tag{28}$$

where r_{ij} is the separation distance between locations and l is the correlation length scale. $(\sigma_{\mu-\mu_0})^2$ is the expected variance for $\mu-\mu_0$. In this case, the weight matrix is constructed from $W_{\mu-\mu_0}=[\mathrm{cov}(\mu-\mu_0)]^{-1}$

b. Local Laplacian form. Here, the weight matrix is formed directly using a local Laplacian operator[5,49,50] between neighboring locations, where

$$W_{\mu-\mu_0} = [1/(\sigma_{\mu-\mu_0})^2] M^T M,$$

where M is the local Laplacian matrix, which is defined as

$$M_{ij} = \begin{cases} 0 & \text{if } i \text{ and } j \text{ are not neighbors} \\ -1 & \text{if } i \text{ and } j \text{ are neighbors} \\ \left|\sum_j M_{ij}\right| & \text{if } i = j \end{cases}, \tag{29}$$

where i and j represent the node numbers of the FEM mesh, which in turn become the indices of the local Laplacian matrix (M). The diagonal terms in M gives the total number of immediately connected nodes.

Computation of $W_{\mu-\mu_0}$ requires an estimate of variance of parameters $[(\sigma_{\mu-\mu_0})^2]$, as is the case for calculation of the Tikhonov regularization parameter [Eq. (14)]. The expected variance can be computed in many ways: the most common method for imaging problems is estimation from the literature. For example, the optical contrast between tumor and normal breast tissue is around 50%–400% (Refs. 51 and 52), which gives the expected standard deviation $(\sigma_{\mu-\mu_0})$ in the optical properties, and can be used to compute variance. The calibration of the experimental data is capable of giving a very good estimate of normal tissue optical properties.[45,46] Note that weight matrix containing the expected variance will not impose a hard constrain on the expected optical properties, but discourages update values ($\Delta\mu$) which are above these expected deviation in a given iteration.

The advantages of the GLS approach are that:

- It accounts for covariance among the parameters and data points.
- It also allows the individual data points/parameters to have different noise characteristics (variances).
- It constrains the problem through the weight matrices, to produce stable solutions.

The limitations of the procedure are:

- It requires prior knowledge about the noise characteristics of parameter and data spaces.
- The weight matrices may necessitate computation of the inverse of covariance matrices (increasing run time and memory requirements).
- It can generate unstable solutions when unreasonable constraints are inadvertently applied.

B. With spatial priors

Overall, the LS minimization schemes using spatial priors can be broadly classified into two approaches: (1) soft-priors and (2) hard-priors. The following two subsections will discuss these two approaches.

1. Soft-priors

In this approach, the regularization matrix L in the Tikhonov approach [Eq. (18)] encodes the spatial information.[21,26] Previous results have shown that using the spatial priors in this fashion do not bias the image estimate when the prior information is imperfect.[26] Typically, the conventional image is segmented into different regions depending on tissue type to generate the spatial constraints. The L matrix relates each nodal optical property in the numerical model to the other nodes in that region.[26] Two possible forms are indicated later.

a. Laplacian form[21]

$$L_{ij} = \begin{cases} 0 & \text{if } i \text{ and } j \text{ are not in the same region} \\ -1/N & \text{if } i \text{ and } j \text{ are in the same region} \\ 1 & \text{if } i = j \end{cases}, \tag{30}$$

where N is the number of sampling points (e.g., nodes in a FEM mesh) in that region.

b. Helmholtz form[26]

$$L_{ij} = \begin{cases} 0 & \text{if } i \text{ and } j \text{ are not in the same region} \\ -1/[N + (\kappa h)^2] & \text{if } i \text{ and } j \text{ are in the same region} \\ 1 & \text{if } i = j \end{cases}, \tag{31}$$

where N is the number of nodes in that region, $\kappa = 1/l$ with l being the covariance length and h is the distance between the nodes.

2. Hard-priors

In the hard-prior approach, also known as a parameter-reduction technique, the number of parameters to be esti-

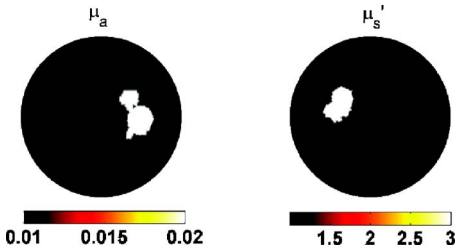

FIG. 2. The chosen optical property distribution/domain for the generation of synthetic data is shown. The diameter of the domain was 86 mm.

mated becomes the number of regions segmented from the other imaging modality (spatial priors).[26,53] Even though the number of parameters to be estimated reduces considerably (relative to soft-priors), the problem can still be ill-posed,[2] so a LM approach was used [Eq. (11)] in this case due to its simplicity. The main advantages of the method are:

- The problem is overdetermined, which also implies J^TJ is positive definite.
- It is computationally efficient.

The limitations include:

- The effect of error or uncertainty in the spatial priors can be amplified by the technique.
- The DOT problem may still be ill-posed (and ill-conditioned) after the constraints are added.[2]

3. Important notes about minimization schemes

There are additional important points about these minimization schemes.

- The weight matrices (W_δ and $W_{\mu-\mu_0}$) in the GLS scheme are computed before the iterative reconstruction procedure begins and are invariant during the iterative process. The same is true of the soft-priors L-matrix calculations.
- The first-order conditions [Eqs. (5), (15), and (21)] derived by minimizing the objective functions [Eqs. (4), (12), and (20)] in all minimization schemes appear on the right-hand side (rhs) of the update equations [Eqs. (11), (18), and (22)] which means that only when the rhs, has reached zero, the solution reached the global minimum.
- Computation of weight matrices, L matrices and the Tikhonov regularization parameter, requires a prior opinion about the variances of the parameters and data. Here, only the best prior estimates are used, which means that the actual variances of the parameter and data spaces are used in the reconstruction procedure. Variation from the best prior values can be examined also, to observe the effect of priors, but that work is beyond the scope of the present article.
- When spatial priors are used in this study (as well as in most studies), it is assumed that they are perfect. The effect of spatial prior uncertainty on the DOT inverse problem is discussed in Refs. 23, 24, and 26 and is the subject of ongoing study.
- The covariance lengths associated in the weight matrix [GLS-analytical covariance (AC) form, Eq. (28)], and the L matrix [Helmholtz form, Eq. (31)] calculations are chosen to be 10 and 5 mm, respectively. The effect of covariance length on the image reconstruction is discussed in Ref. 26.
- In the LM approach [Eq. (11)], the Jacobian is normalized by its optical properties. Also α was chosen initially to be 1 and it was reduced by a factor of $10^{0.25}$ at every iteration and multiplied by the maximum of the diagonal values of J^TJ. The normalization procedure is described in Ref. 54. Moreover, eight iterations were chosen for all the LM reconstructions, as it has been shown in the literature that after this iteration, error in the optical properties increases for this particular problem and algorithm.[55,56] This inherent instability can be attributed to the fact that J^TJ is not positive definite in DOT.
- For simplicity, all the reconstruction algorithms are tested only in the two-dimensional case. Comparison of three-dimensional reconstructions are left for future investigations.

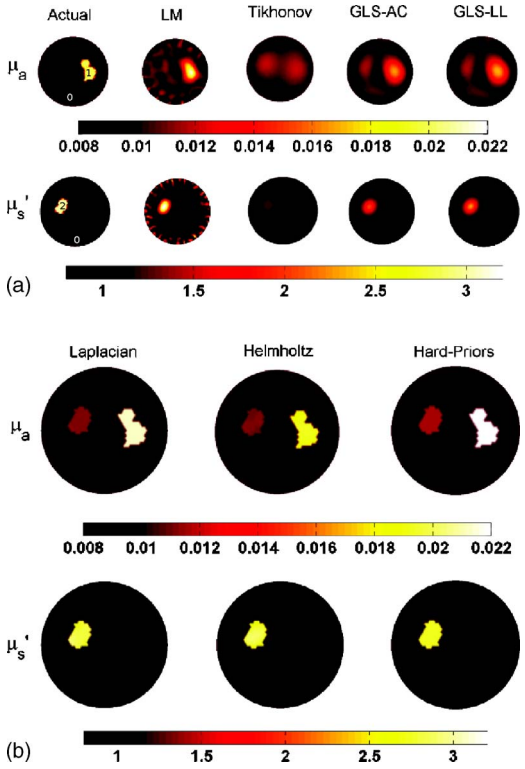

FIG. 3. Reconstruction results (top of the first row, abbreviations are given in Appendix A) are shown using noiseless data (bias calculations) (a) without spatial priors and (b) with spatial priors. The top row contains images of μ_a and bottom row shows μ_s' images.

4. Special cases of GLS minimization

The update equation for the GLS scheme, Eq. (22), turns into the Tikhonov case [Eq. (18)] when $W_\delta = I$ and $W_{\mu-\mu_0}$

TABLE I. Mean and standard deviation of the reconstructed: (a) μ_a and (b) μ_s' values (in mm^{-1}) for different regions [labeled in first column of Fig. 3(a)] recovered with data having 0%, 5%, 10% noise for images shown in Figs. 3–5.

Method	Noise level	Region-0	Region-1	Region-2
Actual	—	0.01	0.02	0.01
LM	*0%*	0.0101±0.001	0.0172±0.0023	0.0105±0.0005
	5%	0.0102±0.0016	0.0125±0.0016	0.0123±0.0011
	10%	0.0103±0.0029	0.0132±0.0026	0.0118±0.0023
Tikhonov	*0%*	0.0102±0.0005	0.0117±0.0003	0.0117±0.0002
	5%	0.0102±0.0004	0.0114±0.0002	0.0112±0.0001
	10%	0.0102±0.0003	0.0108±0.0009	0.0107±0.0005
GLS-AC	*0%*	0.01±0.001	0.015±0.0011	0.0112±0.0003
	5%	0.0101±0.0014	0.0146±0.0012	0.0106±0.0004
	10%	0.0101±0.0013	0.0136±0.0009	0.0112±0.0008
GLS-LL	*0%*	0.01±0.001	0.0152±0.0012	0.0113±0.0003
	5%	0.0101±0.0016	0.0149±0.0015	0.0108±0.0006
	10%	0.0101±0.0016	0.0138±0.0009	0.0112±0.001
Laplacian	*0%*	0.0098±0.0001	0.0212±0.0001	0.0112±0.0001
	5%	0.0098±0.0002	0.0247±0.0001	0.0097±0.0001
	10%	0.0095±0.0001	0.0276±0.0002	0.0157±0.0128
Helmholtz	*0%*	0.0099±0.0001	0.019±0.0002	0.0111±0.0001
	5%	0.0099±0.0002	0.0193±0.0002	0.0099±0.0001
	10%	0.0098±0.0002	0.0174±0.0002	0.0136±0.0001
Hard-Priors	*0%*	0.0099	0.0218	0.0116
	5%	0.0098	0.0218	0.0131
	10%	0.0098	0.018	0.0166

Table 1(a)

Method	Noise level	Region-0	Region-1	Region-2
Actual	—	1.0	1.0	3.0
LM	*0%*	1.0356±0.2364	0.9995±0.0359	2.3758±0.5160
	5%	1.075±0.0357	1.0555±0.3254	1.8215±0.3144
	10%	1.2672±0.9086	1.3111±0.4128	1.7111±0.6112
Tikhonov	*0%*	1.0096±0.0397	1.1153±0.0260	1.1644±0.0251
	5%	1.0111±0.0004	1.0912±0.0189	1.0934±0.0104
	10%	1.0107±0.0216	1.0441±0.0062	1.0416±0.0035
GLS-AC	*0%*	1.0034±0.0688	1.0335±0.0199	1.6838±0.1961
	5%	1.0008±0.0916	1.0670±0.0362	1.6972±0.2037
	10%	0.9987±0.0831	1.0761±0.0343	1.3703±0.0773
GLS-LL	*0%*	1.0022±0.0693	1.03±0.0183	1.7801±0.2573
	5%	0.9998±0.1035	1.0567±0.0329	1.8502±0.3034
	10%	0.9981±0.0947	1.0839±0.0425	1.4271±0.0990
Laplacian	*0%*	0.9918±0.0155	0.9429±0.0015	2.8207±0.0491
	5%	0.9895±0.0202	0.8559±0.0036	3.6931±0.1551
	10%	1.0103±0.0124	0.7447±0.0011	1.9884±0.0096
Helmholtz	*0%*	0.9878±0.0154	1.0518±0.0018	2.7833±0.0854
	5%	0.9813±0.0199	1.1204±0.0081	3.4252±0.1947
	10%	0.9884±0.0121	1.2766±0.01	2.1761±0.0382
Hard-Priors	*0%*	0.9919	0.9266	2.7332
	5%	0.9874	1.0358	2.345
	10%	0.9854	1.3899	1.822

Table 1(b)

$=\lambda L^T L$. Moreover, if one assumes that $\Delta\mu=\mu-\mu_0$, which is equivalent to taking a single step in the iterative procedure, then Eq. (19) maps into Eq. (11) with $\alpha=2\lambda$. Hence, the LM technique can be viewed as a special case of the Tikhonov method, which itself is a special case of the GLS approach. It is important, however, to differentiate LM from the single-step Tikhonov approach because LM requires α to reach zero asymptotically with number of iterations, whereas in the Tikhonov scheme, λ is constant. Moreover, LM does not involve parameters in the objective function.

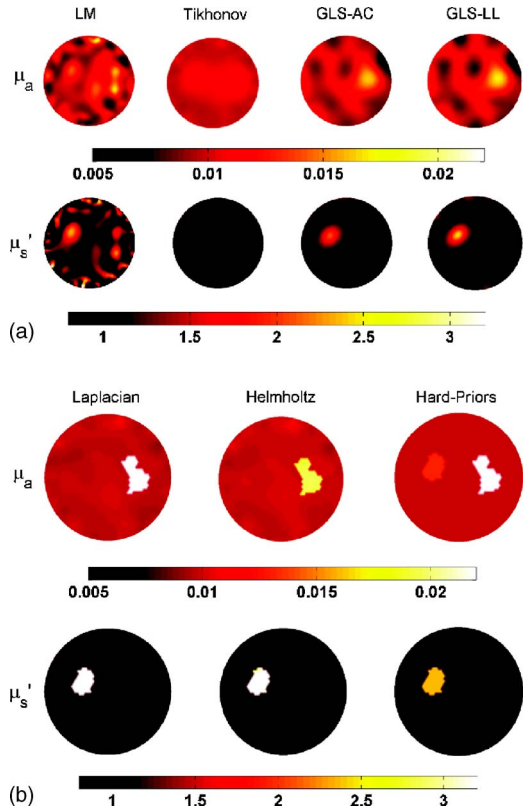

FIG. 4. Reconstruction results (top of the first row, abbreviations are given in Appendix A) are shown using 5% noisy data (a) without spatial priors and (b) with spatial priors. The top row gives images of μ_a and bottom row shows μ_s' images.

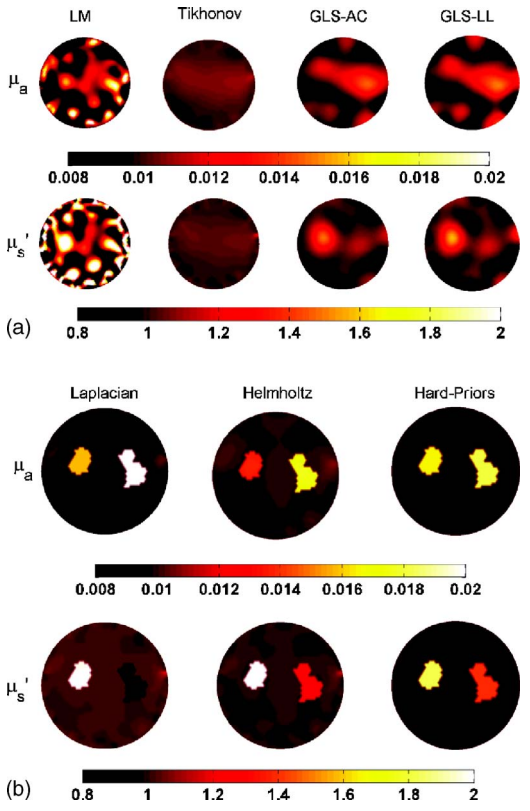

FIG. 5. Reconstruction results (top of the first row, abbreviations are given in Appendix A) are shown using 10% noisy data (a) without spatial priors and (b) with spatial priors. The top row gives images of μ_a and bottom row shows μ_s' images.

5. Stopping criterion

The importance of the stopping criterion in an iterative procedure cannot be ignored. The stopping criterion used in this work is based on the first-order conditions and data-model misfit, which in the limit ensures that the problem has reached the global minima. The iterative procedure is stopped when the $L2$ norm of the data-model misfit (δ) does not improve by more than $10^{-10}\%$ or the $L2$ norm of the first order conditions is less than $10^{-17}\%$. Beyond these values, the round-off error dominates. This stopping criterion is more robust because it involves first-order conditions as well.

IV. TEST PROBLEM

This section provides the details of the test problem considered here. The optical property distributions used for the synthetic data (y, noise added) generation are shown in Fig. 2. The diameter of the domain was 86 mm. The background optical properties were $\mu_a = 0.01\ \text{mm}^{-1}$ and $\mu_s' = 1.0\ \text{mm}^{-1}$. There were two irregular shaped targets, one in μ_a with a contrast of 2:1 to background and one in μ_s' with a contrast of 3:1 relative to the background. A mesh consisting of 4617 nodes (corresponding to 9040 linear triangular elements) was used for the generation of data. Sixteen light collection/delivery fibers were arranged equally spaced on the boundary of the circle, where one fiber was used as the source while all other fibers served as detectors in turn which produced a total of 240 measurements [that is 240 $\ln(A)$ data points and 240 θ data points]. The source was modeled as a Gaussian profile with a full width at half maximum of 3 mm to represent the light applied[57] and was placed at a depth of one transport scattering distance from the tissue boundary.[58] Noise levels of 1%, 3%, 5%, and 10% were added to the modeled data $\{[\ln(A);\theta]\}$ to form the experimental data (y). At the same time, the variances in the data were also computed to be used in the reconstruction algorithms.

The actual reconstructions and forward modeled data computation were performed on different FEM meshes.[59] This mesh has the same diameter (86 mm) with 1785 FEM nodes, which corresponded to 3418 linear triangular elements.[58] The expected distribution of optical properties is given in Fig. 3(a) (first column). Background optical properties were used as initial estimates (μ_0) in the evaluation of reconstruction methods. The number of parameters to be estimated was 3570 (1785 in μ_a and 1785 in μ_s'). The number of data points available for reconstruction was 480 [240 of $\ln(A)$ and 240 of θ]. The dimension of J was 480×3570, W_δ was 480×480, and $W_{\mu-\mu_0}$ was 3570×3570. Optical property distributions were reconstructed from the data without noise (bias calculations) as well as with noise levels of 1%, 3%, 5%, and 10%. The reconstructions are repeated for the case of 3% noise in the data with increasing complexity (targets) in the optical property distributions.

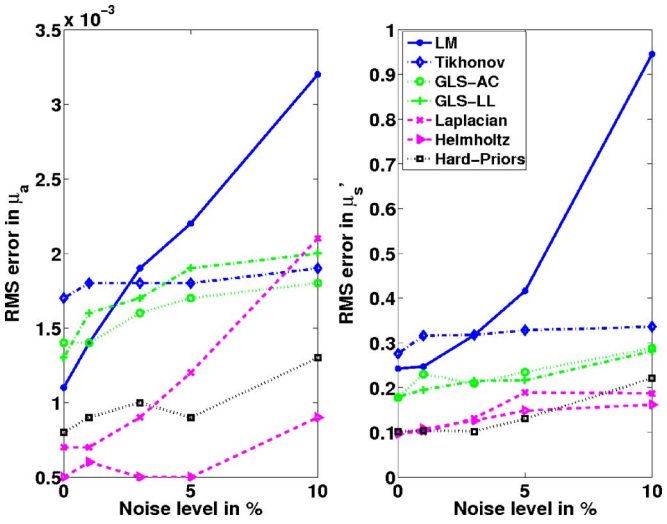

FIG. 6. A plot of the rms error in the estimated optical properties is shown as a function of increasing noise level for all reconstruction techniques.

V. RESULTS AND DISCUSSION

Initially all reconstruction techniques were executed on a data set without noise to estimate the bias. Note that for these calculations the variance was found between the data generated using meshes (described in Sec. IV) with 4617 nodes and 1785 nodes. The results without employing spatial prior information from the reconstruction techniques are given in Fig. 3(a). The first column shows the expected distribution for the 1785 node mesh used in the reconstruction and forward model calculations. The Tikhonov approach failed to recover the contrast. This was primarily due to the choice of λ, which was based on the maximum variance value, which biases the problem to data points that are above the average noise level. Since DOT is known to have a large dynamic range in the data (at least eight orders of magnitude[57]), this choice of λ deemphasize the data points that have low or intermediate variance values. The root-mean-square (rms) errors between the expected and reconstructed optical properties are plotted in Fig. 6. The mean and standard deviation in the reconstructed images for different regions [labeled in first column of Fig. 3(a)] using the reconstruction techniques discussed until now are given in Table I. In the case of no spatial priors, LM gives less bias in μ_a, where as GLS performs better in μ_s'. The bias calculations were repeated with spatial-priors and the reconstruction results are presented in Fig. 3(b). These rms errors in the optical properties are also plotted in Fig. 6. Surprisingly the soft-prior approach (Laplacian and Helmholtz) performed better than the hard-prior strategy. It can also be observed from Fig. 6 and Table I that the usage of spatial priors reduces the bias by at least a factor of 2.

Figure 4(a) shows reconstruction results using data with 5% noise in amplitude without employing spatial priors. Once again the Tikhonov approach fails to recover the contrast. The LM results are dominated by boundary artifacts. Figure 4(b) presents the results from the same data set when spatial priors were employed. Figures 5(a) and 5(b) show similar kinds of effort for the case of data with 10% noise. Note that, for the same choice of the regularization parameter (λ), Tikhonov minimization scheme with spatial priors yielded quantitatively more accurate results compared to without spatial priors case, indicating that the reconstructed image accuracy along with the quality largely depends on the prior information. The rms error in the reconstructed μ_a and μ_s' images are plotted in Fig. 6 as a function of increasing noise level. The rms error using the LM approach increases with increasing noise. GLS techniques perform very well even in the case of 10% noise [Figs. 5(a) and 6]. Among the GLS methods, usage of an analytical covariance form gives better results (≈13% less rms error) in μ_a and the local Laplacian form performs slightly better (≈3% less rms error) in μ_s'. In the case of employment of spatial-priors, it can clearly be seen [from Figs. 4(b), 5(b), and 6 and Table I] that hard-priors perform better in μ_s' reconstruction when the noise level is below 10%. Among the soft-prior results, for μ_a, the rms error linearly increases with increasing noise level in the Laplacian case (Fig. 6). In μ_s' reconstructions, the performance of Laplacian and Helmholtz are comparable, clearly Helmholtz performs slightly better (≈5%) when the noise level is above 3%. Interestingly, the Helmholtz regularization emerges with the lowest rms error in μ_a reconstruction. This is primarily because of the covariance length factor in the Helmholtz form of the regularization matrix [Eq. (31)], which ensures that the optical properties covary within that correlation length (in here it is 5 mm). The same explanation is true for the GLS-analytical covariance form [Eq. (28)], which performs better in μ_a estimation. It is also important to note that in the case of a limited number of wavelengths, Srinivasan *et al.*[60] have shown that 5% error in the optical property estimate (μ_a and μ_s') can lead to approximately 45% error in spectral properties (hemoglobin, water concentrations, oxygen saturation, and scattering estimates) of tissue. Any small improvement in the optical property estimates would be important for improvement in the utility of this type of imaging under practical conditions.

To emphasize the effects of complexity on the reconstruction procedures, a set of simulations were performed with an increasing number of targets. Each target was chosen to be circular with a diameter of 10 mm. The contrast to background optical properties was 2:1. The target locations and corresponding optical properties are shown in the first column of Fig. 7(a). The targets were also labeled from 1 to 4 (background is labeled as 0). The data used in this case have a noise level of 3%. A total of four different reconstructions were performed by adding each target at a time (from 1 to 4). The result of the four target case is shown in Fig. 7. Corresponding mean and standard deviation of the reconstructed optical properties for different regions [labeled in first column of Fig. 7(a)] are given in Table II. Figure 8 contains a plot of rms error in the reconstructed optical properties with increasing number of targets. The rms error increases with increasing number of targets for every reconstruction algorithm. Note that targets 3 and 4 were placed close to the center of the domain, where the sensitivity is low compared

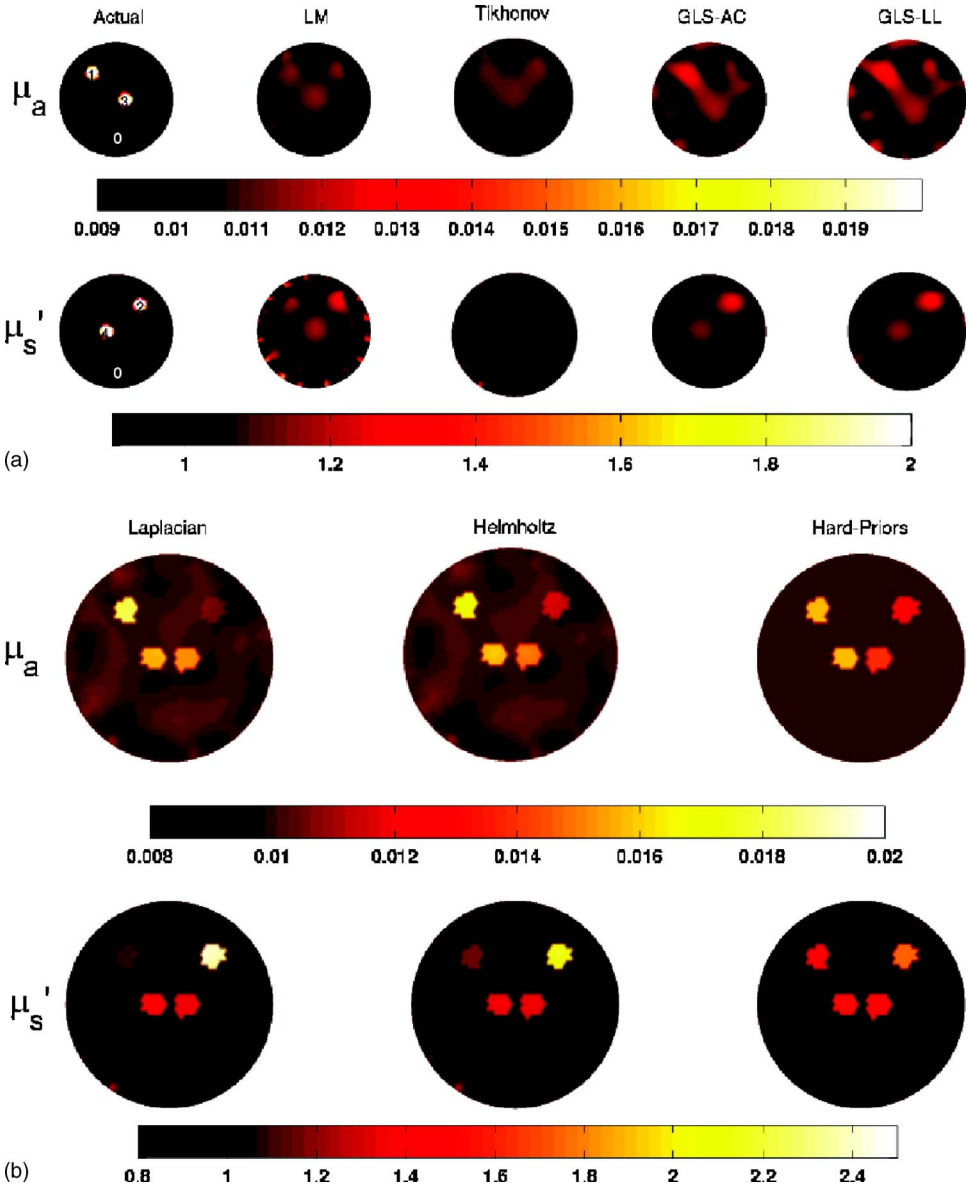

FIG. 7. Reconstruction results (top of the first row, abbreviations are given in Appendix A) are shown using 3% noisy data (a) without spatial priors and (b) with spatial priors for four targets in the tissue as shown. The top row gives images of μ_a and bottom row shows μ_s' images. The actual μ_a and μ_s' with target numbers are given in the first column of (a).

to the periphery.[58] Moreover, increasing the μ_a targets (from 1 to 2, target numbers 1 and 3), caused the rms error to increase by at least 30%. The same is true with the μ_s' targets. In the case of multiple targets, the Helmholtz type of regularization matrix resulted in the least error in both μ_a and μ_s'. Even though the hard-prior case performs very well in terms of lowest rms error for a single target, as the complexity (or number of parameters to be estimated) of the problem increases, it clearly performs poorer than most of the techniques presented (Fig. 8).

Even though the choice of the Tikhonov regularization parameter (λ) given by Eq. (14) is the optimal, the other common way is to use *L*-curve analysis.[61] The *L* curve for DOT is shallow,[62] similar to the estimation problem in electrical impedance tomography, which poses a problem in selection of λ, and is shown to be unreliable in Ref. 59.

Table III gives the computational time per iteration for each of the reconstruction technique (in these two-dimensional cases) on Pentium IV (dual core) 2.8 GHz, 2GB RAM Linux work station. GLS schemes take little more computation time than the Tikhonov minimization, as expected hard priors took the least computation time.

Overall, the inclusion of spatial priors has an important positive effect. The errors in the estimated optical properties are also reduced by at least a factor of 2 with spatial information. The reconstructed images also contain the fine features extracted from conventional imaging modalities. Through the incorporation of the individual variability of the data points and optical parameters (GLS scheme), reconstruction performs better even when the noise level in the data is high. It is also important to note that, as mentioned before, iteration number 8 (which is the best result in terms of lowest rms error) is chosen for rms error calculations in LM approach, after this iteration, the solution becomes unstable. Whereas the rest of the approaches yield stable solutions (error in optical properties did not increase with increasing iterations). When the individual data point variances were not considered (Tikhonov approach), the reconstruction

TABLE II. Mean and standard deviation of the reconstructed: (a) μ_a and (b) μ_s' values (in mm^{-1}) for different regions [labeled in first column of Fig. 7(a)] recovered with data having 3% noise for images shown in Fig. 7.

Method	Region-0	Region-1	Region-2	Region-3	Region-4
Actual	0.01	0.02	0.01	0.02	0.01
LM	0.0101±0.0004	0.0113±0.0001	0.0112±0.0002	0.0111±0.0003	0.011±0.0002
Tikhonov	0.0102±0.0004	0.011±0.0001	0.0112±0.0001	0.0109±0.0001	0.011±0.0001
GLS-AC	0.0102±0.0009	0.0129±0.0003	0.0111±0.0003	0.0114±0.0003	0.0113±0.0003
GLS-LL	0.0102±0.0011	0.0133±0.0004	0.0115±0.0004	0.0113±0.0003	0.0113±0.0002
Laplacian	0.01±0.0002	0.0181±0.0001	0.0105±0.0001	0.0152±0.0001	0.0158±0.0001
Helmholtz	0.01±0.0002	0.0169±0.0001	0.0115±0.0001	0.0149±0.0001	0.0158±0.0001
Hard-Priors	0.01	0.0158	0.0126	0.014	0.0158

(a)

Method	Region-0	Region-1	Region-2	Region-3	Region-4
Actual	1.0	1.0	2.0	1.0	2.0
LM	1.0063±0.0986	1.1333±0.0027	1.24±0.0623	1.1191±0.0396	1.097±0.0366
Tikhonov	1.0051±0.0217	1.0341±0.0019	1.0575±0.0073	1.0321±0.0056	1.0329±0.0043
GLS-AC	0.9993±0.0489	0.9885±0.0139	1.2486±0.0447	1.021±0.0234	1.1184±0.0076
GLS-LL	0.9987±0.0553	0.9764±0.0127	1.2726±0.0596	1.0271±0.0262	1.1422±0.0105
Laplacian	0.9886±0.0163	1.0891±0.0023	2.3799±0.0242	1.3445±0.0043	1.4044±0.0036
Helmholtz	0.9899±0.0164	1.1499±0.0037	2.1122±0.0386	1.3382±0.0079	1.3521±0.0066
Hard-Priors	0.9856	1.3712	1.7319	1.4471	1.5255

(b)

algorithm may not have the ability to recover the contrast in the target. Moreover, simultaneous estimation of both absorption and scattering coefficients causes crosstalk between the two parameter estimates. Even with error-free spatial priors, as the complexity of the estimation problem (or number of targets) increased for a given noise level in the data, the parameter-reduction (hard-priors) technique failed to give the best estimates of the optical properties due to its LM implementation.

VI. CONCLUSIONS

The diffuse optical tomography inverse problem is often solved by Levenberg–Marquardt/modified Tikhonov minimization. A generalized approach for diffuse optical tomographic imaging which incorporates the expected variability of the data noise and magnitude of the optical parameter variation is presented as a structured weight-matrix regularization. It is also shown that Tikhonov minimization and the

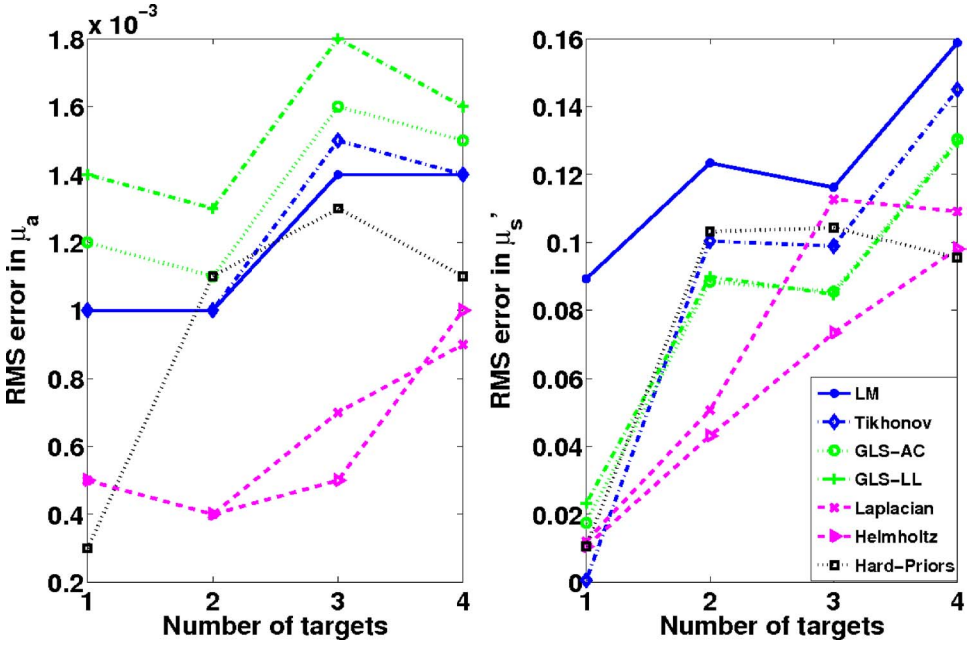

FIG. 8. Plot of the rms error in the estimated optical properties is shown for increasing number of targets with 3% noise in the data for all reconstruction techniques (legend of the figure). Abbreviations used for the techniques are given in Appendix A. The targets used are numbered in the images presented in Fig. 7(a).

TABLE III. Comparison of computation time per iteration for different reconstruction techniques on Pentium IV (dual core) 2.8 GHz, 2 GB RAM Linux work station. the abbreviations used for the reconstruction techniques are given in Appendix A.

Reconstruction method	Computation time per iteration
LM	17.92 Sec
Tikhonov	21.28 Sec
GLS-AC	23.39 Sec
GLS-LL	23.39 Sec
Laplacian	22.78 Sec
Helmholtz	22.78 Sec
Hard-Priors	10.73 Sec

Levenberg–Marquardt approach are special cases of this GLS minimization formalism. Weight matrices that are used in this reconstruction procedure, consisting of the variance and covariance among the data points and optical properties, penalize the solution to match the modeled data with the experimental data more appropriately. This framework can also be used to incorporate structural information, given by MR, computed tomography, or other imaging modalities when the two are acquired on the same tissue volume. Using a test problem, all of these techniques are studied in terms of the data noise level and test field complexity and a uniform comparison was made using the same implementation scheme for each minimization method. Even with highly noisy data, the GLS approach gives meaningful reconstruction results. It appears that the standard Levenberg–Marquardt approach may be unstable for the DOT problem. It is also shown that consideration of the individual variances of data points is the key for an estimation procedure to recover high optical contrast. Employing spatial information reduced the errors in the reconstruction results by at least a factor of 2. Parameter reduction using spatial priors can produce erroneous results when the noise level is high. The same is true for increasing numbers of targets. Future work includes investigating various approaches for incorporating spatial priors into the GLS scheme with experimental data sets. Moreover, a thorough examination of these techniques in three-dimensional case will be taken up as a future investigation. The computer algorithms and test data used in this article (along with some additional material) are given at this web page.[63]

ACKNOWLEDGMENTS

The authors are grateful to Professor Daniel R. Lynch for the useful discussions and valuable comments on this article. P.K.Y. acknowledges the DOD Breast Cancer predoctoral fellowship (BC050309). This work has been sponsored by the National Cancer Institute through Grant Nos. RO1CA78734, PO1CA80139, and DAMD17-03-1-0405.

APPENDIX A: TERMINOLOGY

DOT—diffuse optical tomography.

$\boldsymbol{\mu_a(\mathbf{r})}$—optical absorption coefficient of tissue.

$\boldsymbol{\mu_s'(\mathbf{r})}$—reduced (or transport) scattering coefficient of tissue.

$\boldsymbol{D(\mathbf{r})}$—optical diffusion coefficient of tissue$=1/3[\mu_a(\mathbf{r})+\mu_s'(\mathbf{r})]$.

$\boldsymbol{\mu}$—parameters (generalized) to estimate$=[D(\mathbf{r});\mu_a(\mathbf{r})]$.

$\boldsymbol{\mu_0}$—prior value of the parameters (initial guess, generally obtained from prior calibration of data[45,46]).

$\boldsymbol{F(\mu)}$—forward model.

$\boldsymbol{G(\mu)}$—Modeled data (G—sampled forward model $=S\{F\}$).

$\boldsymbol{A}$—amplitude of the signal.

$\boldsymbol{\theta}$—phase of the signal.

$\boldsymbol{y}$—Measured data$=[\ln(A);\theta]$.

$||X||$—$L2$ norm of vector $X=\sqrt{\Sigma_{i=1}^{N}X_i^2}$.

$\boldsymbol{\delta}$—data-model misfit$=y-G(\mu)$.

$\boldsymbol{W_\delta}$—weight matrix for $\delta=[\mathrm{cov}(\delta)]^{-1}$ (Appendix A-4 of Ref. 47).

$\boldsymbol{W_{\mu-\mu_0}}$—weight matrix for $\mu-\mu_0=[\mathrm{cov}(\mu-\mu_0)]^{-1}$ (Appendix A-4 of Ref. 47).

$\boldsymbol{\lambda}$—Tikhonov regularization parameter.

$\boldsymbol{L}$—Tikhonov regularization matrix.

$\boldsymbol{I}$—identity matrix.

$\boldsymbol{\sigma^2}$—variance.

$\boldsymbol{J}$—Jacobian of the sampled forward model$=\partial G(\mu)/\partial\mu$.

$\boldsymbol{\Omega}$—objective function.

Error—true value-estimated value (prediction).

Bias—difference between the true optical property distribution and estimated optical properties in the case of model generated data (without adding the noise).

Ill-posed—Small changes in the data can cause large changes in the parameters.

Ill-conditioned—the condition number (ratio of largest singular value to smallest singular value) is large, which implies the inverse solution would not be unique.

Ill-determined—(or under-determined) the number of independent equations are smaller than number of unknowns.

Unstability—error gets amplified with iterations.

LM—Levenberg–Marquardt minimization (Sec. III A 1).

Tikhonov—Tikhonov minimization scheme without spatial-priors, $L=I$ (Sec. III A 2).

GLS-AC—generalized least squares minimization scheme (Sec. III A 3) with analytical covariance form for $W_{\mu-\mu_0}$ [Eq. (28)].

GLS-LL—generalized least squares minimization scheme (Sec. III A 3) with local Laplacian form for $W_{\mu-\mu_0}$ [Eq. (29)].

Laplacian—Tikhonov minimization scheme in the case of soft priors (Sec. III B 1) where L approximates Laplacian form, defined by Eq. (30).

Helmholtz—Tikhonov minimization scheme in the case of soft priors (Sec. III B 1) where L approximates Helmholtz form, defined by Eq. (31).

Hard-priors—parameter-reduction technique based on spatial priors (Sec. III B 2).

APPENDIX B: TIKHONOV REGULARIZATION-SINGULAR VALUES

It is interesting to examine Tikhonov regularization from the point of view of singular values. If one rewrites the update equation [Eq. (19)] as

$$[J^T J + \lambda I]\Delta\mu_i = J^T \delta_{i-1} + C, \tag{B1}$$

where $C=\lambda(\mu_{i-1}-\mu_0)$, as it is a constant vector for a chosen iteration i. Singular-value decomposition of J gives

$$J = USV^T, \tag{B2}$$

where U and V are orthonormal matrices containing the singular vectors of J, i.e., $U^TU=I$ and $V^TV=I$. S is a diagonal matrix containing the singular values (S_i) of J. Substituting this into update equation [Eq. (B1)] generates

$$(VS^TU^TUSV^T + \lambda I)\Delta\mu_i = VS^TU^T\delta_{i-1} + C. \tag{B3}$$

Using the orthonormal properties of U and left multiplying by V^T on both sides of Eq. (B3) yields

$$(V^TVS^TSV^T + \lambda V^T)\Delta\mu_i = V^TVS^TU^T\delta_{i-1} + V^TC. \tag{B4}$$

Now using the orthonormal properties of V and rearranging the terms leads to

$$(S^TS + \lambda I)V^T\Delta\mu_i = S^TU^T\delta_{i-1} + V^TC. \tag{B5}$$

Taking the inverse, left multiplying by V and simplifying the result gives

$$\Delta\mu_i = V(S^TS + \lambda I)^{-1}(S^TU^T\delta_{i-1} + V^TC). \tag{B6}$$

Writing Eq. (B7) in the form

$$\Delta\mu_i = VDP, \tag{B7}$$

where $P=(S^TU^T\delta_{i-1}+V^TC)$, a column vector, and D is a diagonal matrix which has the form

$$D_{ij} = \begin{cases} 0 & \text{if } i \neq j \\ \dfrac{1}{S_i^2 + \lambda} & \text{if } i = j. \end{cases} \tag{B8}$$

Similar expressions hold for $L \neq I$ (Ref. 65) in Eq. (18). Considering the case $\lambda=0$, one can clearly see that for an ill-conditioned matrix J, implying some of the singular values are almost zero ($S_i \approx 0$), the inversion becomes unstable (some of the diagonal values of D become infinite). By using Tikhonov regularization, even when $S_i=0$, the inversion procedure is stabilized [Eq. (B8)]. The λ act as a filtering factor, giving the name Tikhonov filtering[65] for this procedure. Moreover, as this λ damps the amplification of the diagonal values of D for smaller values of S_i in Eq. (B8), this is also known as damped least squares minimization procedure.[65]

[a]Electronic mail: phaneendra.k.yalavarthy@dartmouth.edu

[1]A. Gibson, J. C. Hebden, and S. R. Arridge, "Recent advances in diffuse optical tomography," Phys. Med. Biol. **50**, R1–R43 (2005).
[2]S. R. Arridge, "Optical tomography in medical imaging," Inverse Probl. **15**, R41–R93 (1999).
[3]S. R. Arridge and J. C. Hebden, "Optical imaging in medicine: II. Modelling and reconstruction," Phys. Med. Biol. **42**, 841–853 (1997).
[4]S. R. Arridge and M. Schweiger, in "A general framework for iterative reconstruction algorithms in optical tomography, using a finite element method," *The IMA Volumes in Mathematics and Its Applications: Computational Radiology and Imaging, Therapy and Diagnostics*, edited by F. N. C. Börgers (Springer, New York, 1998), pp. 45–70.
[5]M. Schweiger, S. R. Arridge, and I. Nissila, "Gauss–Newton method for image reconstruction in diffuse optical tomography," Phys. Med. Biol. **50**, 2365–2386 (2005).
[6]D. A. Boas, D. H. Brooks, E. L. Miller, C. A. DiMarzio, M. Kilmer, R. J. Gaudette, and Q. Zhang, "Imaging the body with diffuse optical tomography," IEEE Signal Process. Mag. **18**, 57–75 (2001).
[7]B. W. Pogue, M. Testorf, T. McBride, U. Osterberg, and K. D. Paulsen, "Instrumentation and design of a frequency-domain diffuse optical tomography imager for breast cancer detection," Opt. Express **1**, 391–403 (1997).
[8]S. Srinivasan, B. W. Pogue, S. Jiang, H. Dehghani, C. Kogel, S. Soho, J. J. Gibson, T. D. Tosteson, S. P. Poplack, and K. D. Paulsen, "Interpreting hemoglobin and water concentration, oxygen saturation and scattering measured *in vivo* by near-infrared breast tomography," Proc. Natl. Acad. Sci. U.S.A. **100**, 12349–12354 (2003).
[9]R. L. Barbour, H. L. Graber, J. W. Chang, S. L. S. Barbour, P. C. Koo, and R. Aronson, "MRI-guided optical tomography: Prospects and computation for a new imaging method," IEEE Comput. Sci. Eng. **2**, 63–77 (1995).
[10]B. W. Pogue and K. D. Paulsen, "High-resolution near-infrared tomographic imaging simulations of the rat cranium by use of a priori magnetic resonance imaging structural information," Opt. Lett. **23**, 1716–1718 (1998).
[11]V. Ntziachristos, X. H. Ma, and B. Chance, "Time-correlated single photon counting imager for simultaneous magnetic resonance and near-infrared mammography," Rev. Sci. Instrum. **69**, 4221–4233 (1998).
[12]J. P. Kaipio, V. Kolehmanien, M. Vauhkonen, and E. Somersalo, "Inverse problems with structural prior information," Inverse Probl. **15**, 713–729 (1999).
[13]M. Schweiger and S. R. Arridge, "Optical tomographic reconstruction in a complex head model using a priori region boundary information," Phys. Med. Biol. **44**, 2703–2721 (1999).
[14]V. Ntziachristos, A. G. Yodh, M. Schnall, and B. Chance, "Concurrent MRI and diffuse optical tomography of breast after indocyanine green enhancement," Proc. Natl. Acad. Sci. U.S.A. **97**, 2767–2772 (2000).
[15]A. H. Hielscher and S. Bartel, "Use of penalty terms in gradient-based iterative reconstruction schemes for optical tomography," J. Biomed. Opt. **6**, 183–192 (2001).
[16]Q. Zhu, N. G. Chen, and S. C. Kurtzman, "Imaging tumor angiogenesis by use of combined near-infrared diffusive light and ultrasound," Opt. Lett. **28**, 337–339 (2003).
[17]A. Li, E. L. Miller, M. E. Kilmer, T. J. Brukilacchio, T. Chaves, J. Stott, Q. Zhang, T. Wu, M. Chorlton, R. H. Moore, D. B. Kopans, and D. A. Boas, "Tomographic optical breast imaging guided by three-dimensional mammography," Appl. Opt. **42**, 5181–5190 (2003).
[18]B. Brooksby, H. Dehghani, B. W. Pogue, and K. D. Paulsen, "Near infrared (NIR) tomography breast image reconstruction with *a priori* structural information from MRI: algorithm development for reconstructing heterogeneities," IEEE J. Sel. Top. Quantum Electron. **9**, 199–209 (2003).
[19]B. Brooksby, S. Jiang, C. Kogel, M. Doyley, H. Dehghani, J. B. Weaver, S. P. Poplack, B. W. Pogue, and K. D. Paulsen, "Magnetic resonance guided near infrared tomography of the breast," Rev. Sci. Instrum. **75**, 5262–5270 (2004).
[20]X. Intes, C. Maloux, M. Guven, B. Yazici, and B. Chance, "Diffuse optical tomography with physiological and spatial *a priori* constraints," Phys. Med. Biol. **49**, N155–N163 (2004).
[21]B. Brooksby, S. Jiang, H. Dehghani, B. W. Pogue, K. D. Paulsen, J. Weaver, C. Kogel, and S. P. Poplack, "Combining near infrared tomography and magnetic resonance imaging to study *in vivo* breast tissue: Implementation of a Laplacian-type regularization to incorporate magnetic resonance structure," J. Biomed. Opt. **10**, 051504:1–10 (2005).
[22]Q. Zhang, T. J. Brukilacchio, A. Li, J. J. Stott, T. Chaves, E. Hillman, T. Wu, M. Chorlton, E. Rafferty, R. H. Moore, D. B. Kopans, and D. A. Boas, "Coregistered tomographic x-ray and optical breast imaging: initial results," J. Biomed. Opt. **10**, 024033:1–024033:9 (2005).
[23]G. Boverman, E. L. Miller, A. Li, Q. Zhang, T. Chaves, D. H. Brooks, and D. Boas, "Quantitative spectroscopic diffuse optical tomography of the breast guided by imperfect a priori structural information," Phys. Med. Biol. **50**, 3941–3956 (2005).

[24]M. Guven, B. Yazici, X. Intes, and B. Chance, "Diffuse optical tomography with *a priori* anatomical information," Phys. Med. Biol. **50**, 2837–2858 (2005).
[25]B. Brooksby, B. W. Pogue, S. Jiang, H. Dehghani, S. Srinivasan, C. Kogel, T. D. Tosteson, J. Weaver, S. P. Poplack, and K. D. Paulsen, "Imaging breast adipose and fibroglandular tissue molecular signatures using hybrid MRI-guided near-infrared spectral tomography," Proc. Natl. Acad. Sci. U.S.A. **103**, 8828–8833 (2006).
[26]P. K. Yalavarthy, H. Dehghani, B. W. Pogue, C. M. Carpenter, S. Jiang, and K. D. Paulsen, "Structural information within regularization matrices improves near infrared diffuse optical tomography" (unpublished).
[27]A. Douiri, M. Schweiger, J. Riley, and S. R. Arridge, "Anisotropic diffusion regularization methods for diffuse optical tomography using edge prior information," Meas. Sci. Technol. **18**, 87–95 (2007).
[28]H. Jiang, K. D. Paulsen, and U. Osterberg, B. W. Pogue, and M. S. Patterson, "Optical image reconstruction using frequency domain data: simulations and experiments," J. Opt. Soc. Am. A **13**, 253–266 (1996).
[29]M. Schweiger, S. R. Arridge, M. Hiroaka, and D. T. Delpy, "The finite element model for the propagation of light in scattering media: Boundary and source conditions," Med. Phys. **22**, 1779–1792 (1995).
[30]S. R. Arridge and M. Schweiger, "Photon-measurement density functions. Part 2: Finite-element-method calculations," Appl. Opt. **34**, 8026–8037 (1995).
[31]H. Dehghani, B. W. Pogue, S. P. Poplack, and K. D. Paulsen, "Multiwavelength three-dimensional near-infrared tomography of the breast: Initial simulation, phantom, and clinical results," Appl. Opt. **42**, 135–145 (2003).
[32]H. Dehghani, B. Brooksby, K. Vishwanath, B. W. Pogue, and K. D. Paulsen, "The effects of internal refractive index variation in near infrared optical tomography: A finite element modeling approach," Phys. Med. Biol. **48**, 2713–2727 (2003).
[33]S. R. Arridge and M. Schweiger, "A gradient based optimization scheme for optical tomography," Opt. Express **2**, 213–226 (1998).
[34]A. H. Hielscher, A. D. Klose, and K. M. Hanson, "Gradient-based iterative image reconstruction scheme for time-resolved optical tomography," IEEE Trans. Med. Imaging **18**, 262–271 (1999).
[35]K. D. Paulsen and H. Jiang, "Enhanced frequency domain optical image reconstruction in tissues through variation minimization," Appl. Opt. **35**, 3447–3458 (1996).
[36]J. C. Ye, C. A. Bouman, K. J. Webb, and R. P. Milane, "Nonlinear multigrid algorithms for Bayesian optical diffusion tomography," IEEE Trans. Image Process. **10**, 909–922 (2001).
[37]M. J. Eppstein, D. E. Dougherty, D. J. Hawysz, and E. M. Sevick-Muraca, "Three-dimensional Bayesian optical image reconstruction with domain decomposition," IEEE Trans. Med. Imaging **20**, 147–163 (2001).
[38]V. Kolehmainen, "Novel approaches to image reconstruction in diffusion tomography," Ph.D. thesis, Kuopio University, Finland, 2001.
[39]M. S. Zhdanov, *Geophysical Inverse Theory and Regularization Problems*, 1st ed. (Elsevier Science, New York, 2002).
[40]K. Levenberg, "A method for the solution of certain nonlinear problems in least squares," Proc. Soc. Exp. Stress Anal. **2**, 164–168 (1944).
[41]D. W. Marquardt, "An algorithm for least squares estimation of nonlinear parameters," J. Soc. Ind. Appl. Math. **11**, 431–441 (1963).
[42]M. Schweiger, S. R. Arridge, and D. T. Delpy, "Application of the finite element method for the forward and inverse models in optical tomography," J. Math. Imaging Vision **3**, 263–283 (1993).
[43]A. N. Tikhonov and V. A. Arsenin, *Solution of Ill-posed Problems* (Winston and Sons, Washington, 1977).
[44]A. Tarantola, *Inverse Problem Theory and Methods for Model Parameter Estimation* (SIAM, 2004).
[45]B. W. Pogue, K. D. Paulsen, H. Kaufman, and C. Abele, "Calibration of near-infrared frequency-domain tissue spectroscopy for absolute absorption coefficient quantitation in neonatal head-simulating phantoms," J. Biomed. Opt. **5**, 185–193 (2000).
[46]S. Jiang, B. W. Pogue, T. O. McBride, M. M. Doyley, S. P. Poplack, and K. D. Paulsen, "Near-infrared breast tomography calibration with optoelastic tissue simulating phantoms," J. Electron. Imaging **12**, 613–620 (2003).
[47]D. R. Lynch, *Numerical Partial Differential Equations for Environmental Scientists and Engineers—A First Practical Course* (Springer, New York, 2005).
[48]P. K. Yalavarthy and D. R. Lynch, "Generalized least-squares minimization for diffuse optical tomography: Use of complex data," NML Lab Report, NML-06-9, Dartmouth College, 2006, http://www-nml.dartmouth.edu/Publications/internal_reports/NML-06-9/.
[49]B. Brandstter, K. Hollaus, H. Hutten, M. Mayer, R. Merwa, and H. Scharfetter, "Direct estimation of Cole parameters in multifrequency EIT using a regularized Gauss–Newton method," Physiol. Meas **24**, 437–448 (2003).
[50]N. Soni, K. D. Paulsen, H. Dehghani, and A. Hartov, "Finite element implementation of Maxwell's equations for image reconstruction in electrical impedance tomography," IEEE Trans. Med. Imaging **25**, 55–61 (2006).
[51]A. Cerussi, N. Shah, D. Hsiang, A. Durkin, J. Butler, and B. J. Tromberg, "*In vivo* absorption, scattering and physiologic properties of 58 malignant breast tumors determined by broadband diffuse optical spectroscopy," J. Biomed. Opt. **11**, 044005 (2006).
[52]V. Chernomordik, D. W. Hattery, D. Grosenick, H. Wabnitz, H. Rinneberg, K. T. Moesta, P. M. Schlag, and A. Gandjbakhche, "Quantification of optical properties of a breast tumor using random walk theory," J. Biomed. Opt. **7**, 80–87 (2002).
[53]H. Dehghani, B. W. Pogue, J. Shudong, B. Brooksby, and K. D. Paulsen, "Three-dimensional optical tomography: Resolution in small-object imaging," Appl. Opt. **42**, 3117–3126 (2003).
[54]S. Srinivasan, B. W. Pogue, H. Dehghani, S. Jiang, X. Song, and K. D. Paulsen, "Improved quantification of small objects in near-infrared diffuse optical tomography," J. Biomed. Opt. **9**, 1161–1171 (2004).
[55]B. W. Pogue, X. Song, T. D. Tosteson, T. O. McBride, S. Jiang and K. D. Paulsen, "Statistical analysis of non-linearly reconstructed near-infrared tomographic images: Part I—Theory and simulations," IEEE Trans. Med. Imaging **21**, 755–763 (2002).
[56]X. Song, B. W. Pogue, T. D. Tosteson, T. O. McBride, S. Jiang, and K. D. Paulsen, "Statistical analysis of non-linearly reconstructed near-infrared tomographic images: Part II—Experimental interpretation," IEEE Trans. Med. Imaging **21**, 764–772 (2002).
[57]T. O. Mcbride, B. W. Pogue, S. Jiang, U. L. Osterberg, and K. D. Paulsen, "A parallel-detection frequency-domain near-infrared tomography system for hemoglobin imaging of the breast *in vivo*," Rev. Sci. Instrum. **72**, 1817–1824 (2001).
[58]P. K. Yalavarthy, H. Dehghani, B. W. Pogue, and K. D. Paulsen, "Critical computational aspects of near infrared circular tomographic imaging: Analysis of measurement number, mesh resolution and reconstruction basis," Opt. Express **14**, 6113–6127 (2006).
[59]B. M. Graham and A. Adler, "Objective selection of hyperparameter for EIT," Physiol. Meas **27**, S65–S79 (2006).
[60]S. Srinivasan, B. W. Pogue, H. Dehghani, S. Jiang, X. Song, and K. D. Paulsen, "Effect of image reconstruction bias upon spectroscopy-based quantification of chromophores in near infrared tomography," Proc. OSA Biomedical Topical Meetings, OSA Technical Digest, WB3:1-3, Optical Society of America, Washington, DC, 2004.
[61]P. C. Hansen, "Analysis of discrete ill-posed problems by means of the *L*-curve," SIAM Rev. **34**, 561–581 (1992).
[62]R. J. Gaudette, D. H. Brooks, C. A. DiMarzio, M. E. Kilmer, E. L. Miller, T. Gaudette, and D. A. Boas, "A comparison study of linear reconstruction techniques for diffuse optical tomographic imaging of absorption coefficient," Phys. Med. Biol. **45**, 1051–1070 (2000).
[63]http://nir.thayer.dartmouth.edu/lscomparison.html.
[64]P. K. Yalavarthy, "Diffuse optical tomographic reconstruction in low-scattering tissue: Development of inversion algorithms based on Monte-Carlo simulation," M.Sc.(Engg.) thesis, Indian Institute of Science, Bangalore, India, 2004.
[65]M. Fedi, P. C. Hansen, and V. Paoletti, "Analysis of depth resolution in potential-field inversion," Geophysics **70**, A1–A11 (2005).

Structural information within regularization matrices improves near infrared diffuse optical tomography

Phaneendra K. Yalavarthy[†], Brian W. Pogue[†], Hamid Dehghani[§], Colin M. Carpenter[†], Shudong Jiang[†], and Keith D. Paulsen[†]

[†]*Thayer School of Engineering, Dartmouth College, Hanover NH 03755 USA*
[§]*School of Physics, University of Exeter, Stocker Road, Exeter, EX4 4QL, UK*

Phani@dartmouth.edu, Pogue@dartmouth.edu

Abstract: Near-Infrared (NIR) tomographic image reconstruction is a non-linear, ill-posed and ill-conditioned problem, and so in this study, different ways of penalizing the objective function with structural information were investigated. A simple framework to incorporate structural priors is presented, using simple weight matrices that have either Laplacian or Helmholtz-type structures. Using both MRI-derived breast geometry and phantom data, a systematic and quantitative comparison was performed with and without spatial priors. The Helmholtz-type structure can be seen as a more generalized approach for incorporating spatial priors into the reconstruction scheme. Moreover, parameter reduction (i.e. hard prior information) in the imaging field through the enforcement of spatially explicit regions may lead to erroneous results with imperfect spatial priors.

OCIS codes: (170.0170) Medical optics and biotechnology; (170.0110) Imaging systems; (170.3010) Image reconstruction techniques; (170.3880) Medical and biological imaging; (170.6960) Tomography; (100.3190) Inverse problems

References and links

1. D. A. Boas, D. H. Brooks, E. L. Miller, C. A. DiMarzio, M. Kilmer, R. J. Gaudette, and Q. Zhang, "Imaging the body with diffuse optical tomography," IEEE Sig. Proc. Mag. **18**, 57–75 (2001).
2. B. W. Pogue, M. Testorf, T. McBride, U. Osterberg, and K. D. Paulsen, "Instrumentation and design of a frequency-domain diffuse optical tomography imager for breast cancer detection," Opt. Express **1**, 391–403 (1997).
3. S. Srinivasan, B. W. Pogue, S. Jiang, H. Dehghani, C. Kogel, S. Soho, J. J. Gibson, T. D. Tosteson, S. P. Poplack and K. D. Paulsen, "Interpreting Hemoglobin and Water Concentration, Oxygen Saturation and Scattering Measured in Vivo by Near-Infrared Breast Tomography," Proc. Nat. Acad. Sci. U.S.A. **100**, 12349–12354 (2003).
4. Q. Zhu, N. G. Chen, and S. C. Kurtzman, "Imaging tumor angiogenesis by use of combined near-infrared diffusive light and ultrasound," Opt. Lett. **28**, 337–339 (2003).
5. Q. Zhang, T. J. Brukilacchio, A. Li, J. J. Stott, T. Chaves, E. Hillman, T. Wu, M. Chorlton, E. Rafferty, R. H. Moore, D. B. Kopans, and D. A. Boas, "Coregistered tomographic x-ray and optical breast imaging: initial results," J Biomed. Opt. **10**, 024033:1–9 (2005).
6. B. Brooksby, S. Jiang, C. Kogel, M. Doyley, H. Dehghani, J. B. Weaver, S. P. Poplack, B. W Pogue, and K. D Paulsen, "Magnetic resonance guided near infrared tomography of the breast," Rev. Sci. Instrum. **75**, 5262–5270 (2004).
7. A. Li, E. L. Miller, M. E. Kilmer, T. J. Brukilacchio, T. Chaves, J. Stott, Q. Zhang, T. Wu, M. Chorlton, R. H. Moore, D. B. Kopans, and D. A. Boas, "Tomographic optical breast imaging guided by three-dimensional mammography," Appl. Opt. **42**, 5181–5190 (2003).

8. A. Li, G. Boverman, Y. Zhang, D. Brooks, E. L. Miller, M. E. Kilmer, Q. Zhang, E. M. C. Hillman, and D. A. Boas, "Optimal linear inverse solution with multiple priors in diffuse optical tomography," Appl. Opt. **44**, 1948–1956 (2005).
9. V. Ntziachristos, A. G. Yodh, M. Schnall, and B. Chance, "Concurrent MRI and diffuse optical tomography of breast after indocyanine green enhancement," Proc. Nat. Acad. Sci. U.S.A. **97**, 2767-2772 (2000).
10. G. Boverman, E. L. Miller, A. Li, Q. Zhang, T. Chaves, D. H. Brooks, and D. Boas, "Quantitative spectroscopic diffuse optical tomography of the breast guided by imperfect a priori structural information," Phys. Med. Biol. **50**, 3941–3956 (2005).
11. R. L. Barbour, H. L. Graber, J. W. Chang, S. L. S. Barbour, P. C. Koo, R. Aronson, "MRI-guided optical tomography: Prospects and computation for a new imaging method," IEEE Comp. Sci. Eng. **2**, 63–77 (1995).
12. A. H. Hielscher and S. Bartel, "Use of penalty terms in gradient-based iterative reconstruction schemes for optical tomography," J. Biomed. Opt. **6**, 183-192 (2001).
13. V. Ntziachristos, X. H. Ma, and B. Chance, "Time-correlated single photon counting imager for simultaneous magnetic resonance and near-infrared mammography," Rev. Sci. Instrum. **69**, 4221–4233 (1998).
14. B. Brooksby, H. Dehghani, B. W. Pogue, and K. D. Paulsen, "Near infrared (NIR) tomography breast image reconstruction with *a priori* structural information from MRI: algorithm development for reconstructing heterogeneities," IEEE J. Sel. Top. Quantum Electron. **9**, 199–209 (2003).
15. B. Brooksby, S. Jiang, H. Dehghani, B. W. Pogue, K. D. Paulsen, J. Weaver, C. Kogel and S. P. Poplack, "Combining near infrared tomography and magnetic resonance imaging to study in vivo breast tissue: implementation of a Laplacian-type regularization to incorporate magnetic resonance structure," J. Biomed. Opt. **10**, 051504:1–10 (2005).
16. B. Brooksby, B. W. Pogue, S. Jiang, H. Dehghani, S. Srinivasan, C. Kogel, T. D. Tosteson, J. Weaver, S. P. Poplack and K. D. Paulsen, "Imaging breast adipose and fibroglandular tissue molecular signatures using Hybrid MRI-Guided Near-Infrared Spectral Tomography," Proc. Nat. Acad. Sci. U.S.A. **103**, 8828–8833 (2006).
17. M. F. Ernst and J. A. Roukema, "Diagnosis of non-palpable breast cancer: a review," The Breast **11**, 13 (2002).
18. H. Dehghani, B. W. Pogue, S. P. Poplack, and K. D. Paulsen, "Multiwavelength three-dimensional near-infrared tomography of the breast: initial simulation, phantom, and clinical results," Appl. Opt. **42**, 135–145 (2003).
19. X. Wang, B.W. Pogue, S. Jiang, X. Song, K.D. Paulsen, C. Kogel, S.P. Poplack, and W.A. Wells, , "Approximation of Mie scattering parameters in near-infrared tomography of normal breast tissue in vivo," J. Biomed. Opt. **10**, 051704:1–8 (2005).
20. S. R. Arridge, "Optical tomography in medical imaging," Inv. Problems **15**, R41–R93 (1999).
21. S. Srinivasan, B. W. Pogue, H. Dehghani, S. Jiang, X. Song, and K. D. Paulsen, "Improved quantification of small objects in near-infrared diffuse optical tomography," J. Biomed. Opt. **9**, 1161–1171 (2004).
22. H. Dehghani, B. W. Pogue, J. Shudong, B. Brooksby, and K. D. Paulsen, "Three-dimensional optical tomography: resolution in small-object imaging," Appl. Opt. **42**, 3117–3126 (2003).
23. B. Brooksby, S. Srinivasan, S. Jiang, H. Dehghani, B. W. Pogue, K. D. Paulsen, J. Weaver, C. Kogel, and S. P. Poplack, "Spectral priors improve near-infrared diffuse tomography more than spatial priors," Opt. Lett. **30**, 1968–1970 (2005).
24. H. Jiang, K. D. Paulsen, and U. Osterberg, B. W. Pogue, and M. S. Patterson, "Optical image reconstruction using frequency domain data: simulations and experiments," J. Opt. Soc. Am. A **13**, 253–266 (1996).
25. M. Schweiger, S. R. Arridge, M. Hiroaka, and D. T. Delpy, "The Finite Element Model for the Propagation of Light in Scattering Media: Boundary and Source Conditions," Med. Phys. **22**, 1779–1792 (1995).
26. K. D. Paulsen and H. Jiang, "Spatially varying optical property reconstruction using a finite element diffusion equation approximation," Med. Phys. **22**, 691-701 (1995).
27. A. N. Tikhonov, "Regularization of mathematically incorrectly posed problems," Soviet Math. Dokl. **4**, 1624-1627 (1963).
28. P. K. Yalavarthy, B. W. Pogue, H. Dehghani, and K. D. Paulsen, "Weight-matrix structured regularization provides optimal generalized least-squares estimate in diffuse optical tomography," Med. Phys. 34(6), 2085–2098 (2007).
29. K. Levenberg, "A method for the solution of certain nonlinear problems in least squares," Q. Appl. Math. **2**, 164-168 (1944).
30. D. W. Marquardt, "An algorithm for least squares estimation of nonlinear parameters," J. Soc. Ind. Appl. Math. **11**, 431-441 (1963).
31. H. Jiang, K. D. Paulsen, U. Osterberg, B. W. Pogue, and M. S. Patterson, "Simultaneous reconstruction of optical absorption and scattering maps in turbid media from near-infrared frequency-domain data," Opt. Lett. **20**, 2128-2130 (1995).
32. B. W. Pogue, K. D. Paulsen, H. Kaufman, and C. Abele, "Calibration of near-infrared frequency-domain tissue spectroscopy for absolute absorption coefficient quantitation in neonatal head-simulating phantoms," J. Biomed. Opt. **5**, 185-193 (2000).
33. S. Jiang, B. W. Pogue, T. O. McBride, M. M. Doyley, S. P. Poplack, and K. D. Paulsen, "Near-infrared breast tomography calibration with optoelastic tissue simulating phantoms," J. Electron. Imaging **12**, 613–620 (2003).
34. D. R. Lynch, *Numerical partial differential equations for environmental scientists and engineers – A first practi-*

cal course, (Springer, Edition 1, 2005).
35. T. O. Mcbride, B. W. Pogue, S. Jiang, U. L. Osterberg, and K. D. Paulsen, "A parallel-detection frequency-domain near-infrared tomography system for hemoglobin imaging of the breast in vivo," Rev. Sci. Instrum. **72**, 1817–1824 (2001).
36. P. K. Yalavarthy, H. Dehghani, B. W. Pogue, and K. D. Paulsen, "Critical computational aspects of near infrared circular tomographic imaging: Analysis of measurement number, mesh resolution and reconstruction basis," Opt. Express **14**, 6113–6127 (2006).
37. B. Brooksby, *Combining near infrared tomography and magnetic resonance imaging to improve breast tissue chromophore and scattering assessment*, Ph.D. Thesis, Dartmouth College, May 2005.
38. S. Srinivasan, B. W. Pogue, H. Dehghani, S. Jiang, X. Song, and K. D. Paulsen, " Effect of image reconstruction bias upon spectroscopy-based quantification of chromophores in near infrared tomography," Proc. OSA Biomedical Topical Meetings, OSA Technical Digest, WB3:1-3, Optical Society of America, Washington, DC (2004).

1. Introduction

Near Infrared (NIR) optical tomography is a method that uses light in the 650-900nm wavelength range to recover images of the internal spatial distribution of tissue optical properties, absorption (or chromophore concentrations) and scattering parameters[1-3]. When imaged at multiple wavelengths, these quantities can be used to estimate tissue hemoglobin and water concentration[3] and have the advantage of being acquired non-invasively and without ionizing radiation. The imaging procedure can be rapidly or repeatedly applied to investigate physiological state, and systems can be integrated into conventional imaging platforms such as X-ray mammography, Ultrasound and MRI[4-9]. These hybrid systems have been shown to achieve superior performance in terms of resolution and quantitative accuracy which should provide more accurate physiological data from the tissue under investigation[4-16]. However, a fundamental question is how to utilize the spatial information from the clinical system to maximize the accuracy of NIR tomography. In this study, the ability to improve the quantitative accuracy of regions imaged with NIR tomography was investigated, in the setting where prior spatial information is readily available.

This work explores image reconstruction strategies that take advantage of multimodality image data, in particular, the combination of MRI with NIR optical tomography for breast cancer imaging. MRI provides structural information at high spatial resolution (near 1 mm), whereas NIR imaging has relatively poor spatial resolution (near 4-7 mm). Yet MR imaging would benefit from the molecular-specific signatures available through NIR[3, 16-18], specifically tissue hemoglobin content, oxygenation level, and water, as well as scattering particle size and number density [19]. The inverse problem (image reconstruction procedure) in NIR imaging is known to be a non-linear, ill-posed and ill-conditioned problem [20]. Use of structural information in NIR reconstruction schemes has been explored by several research groups. For example, Li et. al [7] have used the data derived from X-ray mammography for choosing different regularization parameters for the region of interest (ROI) and surrounding tissue, and have shown that the contrast and resolution of the reconstructed images can be improved. Srinivasan et al. [21] have developed a three-step reconstruction process for improving the quantification accuracy of small-objects in NIR tomography, where they use the conventional NIR reconstructed images (first step) as a structural prior for the last two steps. Earlier papers have shown that optical contrast can be correlated to MR contrast [6, 9, 13] and that structural MRI images can be used to reduce the number of unknown parameters to be estimated [14]. The difficulty with parameter reduction approaches (referred to as *hard-priors* [22]) is the potential of introducing error by imposing incorrect model assumptions and introducing variation due to uncertainty in the prior information (even when the underlying model is appropriate). For example, the features which lead to contrast in one imaging system may not be spatially coregistered with those that produce contrast in another imaging system. Further, segmentation of congruent features always includes classification errors resulting from digitization. Recently, Boverman et. al [10] showed

that even imperfect priors which encode breast background structure improves anomaly localization, but at the expense of biasing the spectroscopic dimension of the image reconstruction. Another type of approach for constraining the problem, often described as soft-priors, penalizes the variation within regions which are assumed to have the same properties by controlling regularization. Brooksby et. al [15, 16, 23] have developed a Laplacian type of regularization that allows intra-region variability. This is a method which works well even if the confidence in the prior structural information is low.

This paper develops a more generalized framework, known as soft-priors, for incorporating the structural priors into the NIR image reconstruction process, and explores a covariance-based constraint scheme adopted from finite differencing of the Helmholtz equation in addition to the soft and hard prior approaches noted above. The soft-prior approach allows optical property variation with a given region, reducing biases caused by the use of imperfect prior information. The results indicate that imperfect structural information can generate errors in the hard-priors case, whereas the soft-priors are able to quantify regions more appropriately. Simulation and experimental studies are performed to demonstrate the superior reconstruction image quality. These types of procedures are needed to improve NIR imaging both in terms of high spatial resolution available from MRI and high contrast inherent in the NIR signal.

2. Methods: mathematical formulation

2.1. Diffusion-based Light Transport Model

Light transport in breast tissue can be described accurately by the Diffusion Equation (DE), which is an approximation to the Radiative Transport Equation (RTE) [24]. In the frequency-domain, the DE is given by

$$-\nabla.\mathbf{D}(\mathbf{r})\nabla\Phi(\mathbf{r},\omega)+(\mu_{\mathbf{a}}(\mathbf{r})+i\omega/c)\Phi(\mathbf{r},\omega)=Q_o(\mathbf{r},\omega) \tag{1}$$

where $\Phi(\mathbf{r},\omega)$ is the photon density at position $\mathbf{r}$ and light modulation frequency is given by ω (in this work, ω = 100 MHz). The isotropic source term is represented by $Q_o(\mathbf{r},\omega)$ and speed of light in tissue by c. $\mu_{\mathbf{a}}(\mathbf{r})$ is the optical absorption coefficient and $\mathbf{D}(\mathbf{r})$ is the optical diffusion coefficient, which is defined as

$$\mathbf{D}(\mathbf{r})=\frac{1}{3[\mu_{\mathbf{a}}(\mathbf{r})+\mu'_{\mathbf{s}}(\mathbf{r})]} \tag{2}$$

where $\mu'_{\mathbf{s}}(\mathbf{r})$ is the reduced scattering coefficient, which is defined as $\mu'_{\mathbf{s}}=\mu_{\mathbf{s}}(1-g)$. $\mu_{\mathbf{s}}$ is the scattering coefficient and g is the anisotropy factor. A Robin-type (Type-III) boundary condition is applied to exactly model the refractive-index mismatch at the boundary [25]. The boundary data for a frequency domain system are the amplitude and phase of the measured signal, which is used with a Finite Element Method (FEM) based reconstruction procedure to obtain the internal spatial distributions of μ_a and μ'_s.

2.2. Standard image reconstruction

The objective function (Ω) for this procedure can be written as

$$\Omega=\min_{\mathbf{D},\ \mu_{\mathbf{a}}}\ \{\|\mathbf{y}-\mathbf{F}(\mathbf{D},\mu_{\mathbf{a}})\|^2+\lambda\,\|(\mathbf{D},\mu_{\mathbf{a}})-(\mathbf{D_0},\mu_{\mathbf{a0}})\|^2\} \tag{3}$$

Where, $\mathbf{F}$ is the forward operator that generates the model response and $\mathbf{y}$ is the experimental measured data. $\|.\|^2$ represents L2-Norm of the vector. This is also known as the Tikhonov approach [27], where λ is the regularization parameter that balances the current estimate of

optical properties and the initial values, and the data-model misfit. More specifically, it is the ratio of the variances of the data noise and the parameter ($\lambda = \sigma_y^2/\sigma_{(D,\mu_a)}^2$)[28]. Minimizing Eq. (3) (by setting first derivatives with respect to μ_a and D to zero) leads to an update equation

$$(J^T J + \lambda I)(\delta \mathbf{D}, \delta \mu_\mathbf{a}) = J^T(\mathbf{y} - \mathbf{F}(\mathbf{D}, \mu_\mathbf{a})) - \lambda[(\mathbf{D}, \mu_\mathbf{a}) - (\mathbf{D_0}, \mu_\mathbf{a0})] \tag{4}$$

Note that deriving this update equation is not so straight forward, the full derivation is given in Ref. [28]. In Eq. 4, J is the Jacobian matrix and I is the identity matrix. Note that $J^T J$ is ill-conditioned; λI stabilizes the matrix. However, a slight deviation from this update equation is generally employed, which is also known as the Levenberg-Marquardt (LM) regularization method[29, 30], assuming $[(\delta D, \delta \mu_a) = (\mathbf{D}, \mu_\mathbf{a}) - (\mathbf{D_0}, \mu_\mathbf{a0})]$ leading to [31]

$$(J^T J + 2\lambda I)(\delta \mathbf{D}, \delta \mu_\mathbf{a}) = J^T(\mathbf{y} - \mathbf{F}(\mathbf{D}, \mu_\mathbf{a})) \tag{5}$$

Most of the literature reports $\lambda^* \equiv 2\lambda$[20, 31], which is true only for the Levenberg-Marquardt minimization which does not involve the parameter field in the objective function (Eq. 3)[29, 30]. A detailed discussion about different least-squares minimization methods is presented in Ref. [28]. In this LM approach, λ^* typically starts being the ratio of the variances and is reduced at each of the iterations by a small factor (in here, it is $\sqrt{10}$ and also multiplied by the maximum of the diagonal values of $J^T J$[21]). The iterative procedure is repeated until experimental data matches with modeled data within a preset value ε ($\approx$ data noise level). In general, the initial values, $(\mathbf{D_0}, \mu_\mathbf{a0})$, are obtained from a pre-reconstruction step where the data is calibrated by a homogeneous fitting procedure[32, 33].

2.3. *Inclusion of* a priori *information: Soft-Priors*

The objective function with inclusion of prior information is given as[15]

$$\Omega = \min_{\mathbf{D},\ \mu_\mathbf{a}} \{\|\mathbf{y} - \mathbf{F}(\mathbf{D}, \mu_\mathbf{a})\|^2 + \lambda \|L[(\mathbf{D}, \mu_\mathbf{a}) - (\mathbf{D_0}, \mu_\mathbf{a0})]\|^2\} \tag{6}$$

Here also λ is the ratio of the variance of the data noise to parameter field and L is a penalty matrix (dimensionless in all the cases considered in this work) which can be derived from MRI structural priors as indicated below. The update equation resulting from this procedure is:

$$(J^T J + \lambda L^T L)(\delta \mathbf{D}, \delta \mu_\mathbf{a}) = J^T(\mathbf{y} - \mathbf{F}(\mathbf{D}, \mu_\mathbf{a})) - \lambda L^T L[(\mathbf{D}, \mu_\mathbf{a}) - (\mathbf{D_0}, \mu_\mathbf{a0})] \tag{7}$$

In this work, each location in the computational discretized model is labeled according to tissue type (fatty, fibroglandular or tumor) determined from MRI T1-weighted images[15, 16, 23]. It was also assumed that there is no covariance between the different regions of the imaging domain. Since the domain model does not itself change throughout the iterative reconstruction algorithm, the L-matrix is calculated before the reconstruction procedure and it is used through out the process to penalize the solution. In implementation of Eq. 7 for simultaneous reconstruction of D and μ_a, using the Jacobian form described in Ref. [18] leads to the block matrices

$$\left\{\left[\begin{array}{c|c} H_{D^2} & H_{D\mu_a} \\ \hline H_{D\mu_a} & H_{\mu_a{}^2} \end{array}\right] + \left[\begin{array}{c|c} (\lambda_D)L^T L & 0 \\ \hline 0 & (\lambda_{\mu_a})L^T L \end{array}\right]\right\}\left[\begin{array}{c} \delta k \\ \delta \mu_a \end{array}\right] = \left[\begin{array}{c} (J^T)_D\,(y - F(\mathbf{D}, \mu_\mathbf{a})) \\ (J^T)_{\mu_a}\,(y - F(\mathbf{D}, \mu_\mathbf{a})) \end{array}\right] - \left[\begin{array}{c} (\lambda_D)L^T L\,(D_{i-1} - D_0) \\ (\lambda_{\mu_a})L^T L\,(\mu_{ai-1} - \mu_{a0}) \end{array}\right] \tag{8}$$

where H represents Hessian matrix ($J^T J$). Since D and μ_a are considered to be independent of each other in the estimation procedure, the cross-terms in the combined regularization matrix ($\lambda L^T L$) become zero. Two forms for the L-matrix are discussed in the subsections below, including the Laplacian and Helmholtz structures.

2.3.1. a Laplacian-type structured regularization matrix

The Laplace equation in parameter $u(r)$ can be written as

$$\nabla^2 u(r) = 0 \tag{9}$$

A finite difference approximation to this equation for 'N' number of equi-space (step size = h) nodes can be written as [34]

$$\nabla^2 u(r)h^2 \approx u_1 + u_2 + \ldots - N u_{N/2} + \ldots + u_{N-1} + u_N = 0 \tag{10}$$

Dividing the whole equation by '-N' leads to

$$\frac{-u_1}{N} + \frac{-u_2}{N} + \ldots + u_{N/2} + \ldots + \frac{-u_{N-1}}{N} + \frac{-u_N}{N} = 0 \tag{11}$$

The L matrix is a matrix that relates each nodal property of the numerical model to all other nodes. Therefore given a node i within the mesh, its relationship to another node j having Laplacian structure (Eq. 11) within the same mesh can be given as [15, 16]

$$L_{ij} = \begin{cases} 0 & \text{if i and j are not in the same region} \\ -1/N & \text{if i and j are in the same region} \\ 1 & \text{if i = j} \end{cases} \tag{12}$$

where N is the number of finite element mesh nodes comprising a given region. In this case, $L^T L$ approximates a second-order Laplacian smoothing operator within each region, and functionally works to average the update within a region, while allowing discontinuity between different regions.

2.3.2. a Helmholtz-type structured regularization matrix

The Helmholtz equation in parameter u(r) for a damped wave can be written as

$$\nabla^2 u(r) - \kappa^2 u(r) = 0 \tag{13}$$

where κ is the wave number, specifically $\kappa = 1/l$, where l covariance length[34]. l also represents the decay length scale over which the parameter $u(r)$ has correlation. Making κ = 0, will give the Laplace equation (Eq. 9). A finite difference approximation to this equation for 'N' number of equi-space (step size = h) nodes can be written as [34]

$$\left(\nabla^2 - \kappa^2\right) u(r)h^2 \approx u_1 + u_2 + \ldots + [-(N + (\kappa h)^2)] u_{N/2} + \ldots + u_{N-1} + u_N = 0 \tag{14}$$

Dividing the whole equation by '$-(N + (\kappa h)^2)$' gives

$$\frac{u_1}{-(N + (\kappa h)^2)} + \frac{u_2}{-(N + (\kappa h)^2)} + \ldots + u_{N/2} + \ldots + \frac{u_{N-1}}{-(N + (\kappa h)^2)} + \frac{u_N}{-(N + (\kappa h)^2)} = 0 \tag{15}$$

Writing this as a generalized L-matrix form similar to Eq. 12

$$L_{ij} = \begin{cases} 0 & \text{if i and j are not in the same region} \\ -\frac{1}{N+(\kappa h)^2} & \text{if i and j are in the same region} \\ 1 & \text{if i = j} \end{cases} \tag{16}$$

For the FEM nodes case, h is chosen to be the distance between the nodes. Moreover, $\kappa = 1/l$ is generally chosen to be the inverse of the size of the feature (tumor in this case) in the imaging

domain. This can be seen as using the best priors for the estimation of optical properties[28], termed as best priors estimate (BPE). As the prior structural information is available through MRI, l is chosen to be the diameter of the target (tumor) in the BPE case. In this case, $L^T L$ (L given by Eq. 16) approximates a second-order Helmholtz smoothing operator. To determine the effect of κ on the parameter reconstruction, different values for κ are chosen. It is shown that for small values of κ, which corresponds to a large correlation length (l), both Laplacian and Helmholtz structures recover the same optical property distribution.

2.4. Inclusion of a priori *information: hard-priors*

Reduction of parameter space to the number of regions segmented from a high resolution imaging modality is known as hard-priors[28]. In this section, a detailed formulation for this approach is given. The estimation optical properties (D and μ_a) in this procedure is performed through LM minimization, which was discussed in detail in Ref. [28]. The update equation in this case is given by Eq. 5, with Jacobian having dimension of (2*NM)x(2*NR) instead of (2*NM)x(2*NN). In here, NM, NN and NR represent the number of measurements, number of FEM nodes, and number of regions, respectively. The multiplication factor 2 in the dimensions results from the treatment of amplitude and phase separately for the frequency-domain signal, and the estimated parameters being D and μ_a. This transformation requires multiplication of original Jacobian, J, by region mapper matrix (R)[22].

$$\tilde{J} = JR \tag{17}$$

where the R has dimension of (2*NN)x(2*NR), having a block form $R = \begin{bmatrix} \Sigma \\ \Sigma \end{bmatrix}$. J can be also seen as a block matrix with $J = [J_D \; J_{\mu_a}]$. If RL_j represented a segmented region (j) in the FEM mesh for j = 1, 2, ...NR, then Σ has the from

$$\Sigma_{ij} = \begin{cases} 1 & \text{if } i \in RL_j \\ 0 & \text{otherwise} \end{cases} \tag{18}$$

Overall, the new Jacobian $\tilde{J}$ matrix elements were produced by adding the sensitivity of nodes belonging to the same region[22]. Using $\tilde{J}$ instead of J, in Eq. 5 gives the update of optical properties of the segmented regions $\left(\delta\tilde{\mathbf{D}}, \delta\tilde{\mu}_{\mathbf{a}}\right)$ having dimension of (2*NR)x1. To map back this solution vector to the original dimensions (2*NN)x1, requires

$$(\delta\mathbf{D}, \delta\mu_{\mathbf{a}}) = R\left(\delta\tilde{\mathbf{D}}, \delta\tilde{\mu}_{\mathbf{a}}\right) \tag{19}$$

It is also important to relaize that even though, NR$\ll$NM, solving this might still be ill-posed[20], leading to LM update equation[28].

3. Methods: simulations and experiments

3.1. Breast geometry - Effect of imperfect a priori *information*

The techniques described in Sec. 2 were used to reconstruct images from synthetic data with 1% random noise added. Numerical experiments using synthetic data generated on MRI T1-weighted breast images with incorrect priors to show the effectiveness of soft-priors. Figure 1(a) (first column) shows the original distribution of three tissue layers, namely fatty (μ_a = 0.006 mm^{-1} and μ_s' = 0.6 mm^{-1}), fibro glandular (μ_a = 0.012 mm^{-1} and μ_s' = 1.2 mm^{-1}), and tumor (μ_a = 0.018 mm^{-1} and μ_s' = 1.8 mm^{-1}) for the breast geometry (labeled as 0, 1 and 2 respectively, in Fig. 1(a) first column). Sixteen light collection/delivery fibers were arranged

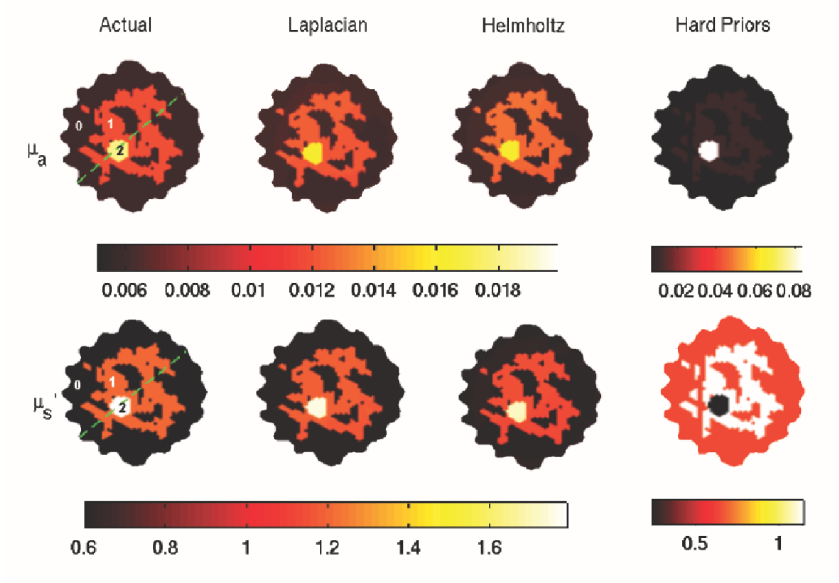

(a)

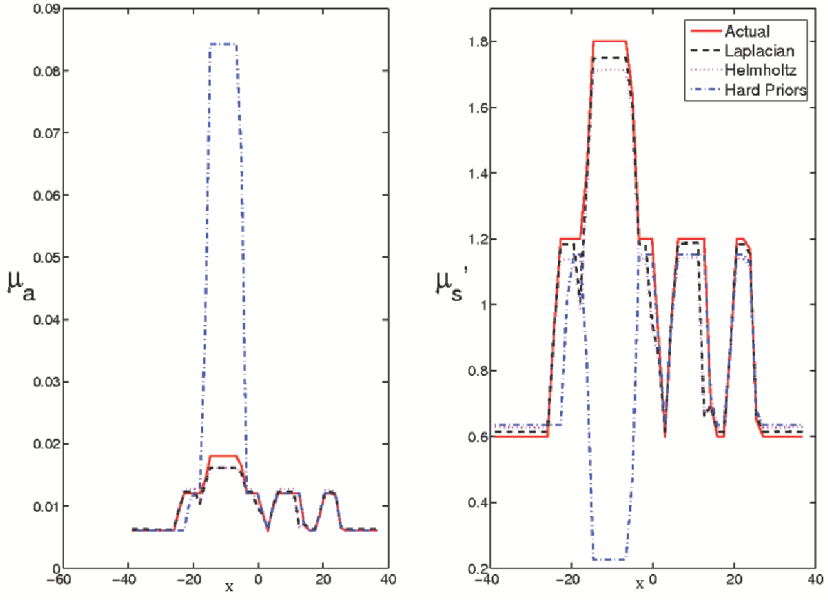

(b)

Fig. 1. (a) Simulated μ_a and μ_s' distributions from a breast (obtained from a volunteer) are shown in the first column. Optical properties for the region labeled '0' (fat) are: μ_a = 0.006 mm^{-1} and μ_s = 0.6 mm^{-1}. Region '1' (fibroglandular) values are: μ_a = 0.012 mm^{-1} and μ_s' = 1.2 mm^{-1}. Region '2' (tumor) values are: μ_a = 0.018 mm^{-1} and μ_s' = 1.8 mm^{-1}. Reconstructed μ_a and μ_s' images from different techniques with simulated data having 1% random noise and imperfect structural information in defining region '1' (7% reduction compared to the original segmentation) are shown in the rest of the columns. The middle two columns use soft prior structural information while the last column shows the result with hard prior information. In the Helmholtz case, κ = 1/8 mm^{-1} (BPE) was used. (b) Cross-sectional plots, along the dotted line in the actual image (see first column of (a)), of true and reconstructed μ_a and μ_s' distributions.

equally spaced on a circle (indentions in Fig. 1(a)). In succession, one fiber was used as the source while all other fibers served as detectors which provided a total of 240 measurements. In these studies, the source was modeled as a Gaussian profile with a Full Width Half Maximum (FWHM) of 3 mm to most accurately represent the light applied in the clinical system[35], and was placed at a depth of one transport scattering distance from the tissue boundary. A mesh of 1785 nodes (corresponding to 3418 linear triangular elements) with uniform nodal density was used for the diffusion model and reconstruction calculations[36]. A total of 7% of the glandular layer (label-1) FEM nodes were labeled (relative to the original glandular layer nodes) as fat (label-0) to introduce imperfect structural priors.

The same initial estimates (optical properties of region '0') were used as homogeneous starting conditions. The iterative procedure was stopped once the data-model misfit (residual) did not improve by more than 2% when compared with the previous iteration. The starting value for λ is chosen to be 25000 and 75 for μ_a and D respectively, derived from the noise characteristics[28], for Eq. 5. For the case of Eq. 7, a starting value of 10 was chosen and was decreased as the iterations progressed, this procedure is outlined in Ref. [21].

Table 1. Mean and standard deviation of the reconstructed (a) μ_a and (b) μ_s' values in different regions (labeled in first column of Fig. 1(a)) recovered with simulated data having 1% random noise and imperfect structural information defining region '1' (7% reduction compared to the original segmentation). The corresponding reconstructed images are shown in Fig. 1(a)

Methods	*Region-0*	*Region-1*	*Region-2*
Actual	0.006	0.012	0.018
Laplacian	0.0064±0.0010	0.0117±0.0018	0.0156±0.0018
Helmholtz (κ = 1/8)	0.0062±0.0011	0.0120±0.0020	0.0156±0.0017
Hard Priors	0.006	0.0118	0.0843

(a)

Methods	*Region-0*	*Region-1*	*Region-2*
Actual	0.6	1.0	1.8
Laplacian	0.63±0.10	1.13±0.18	1.67±0.23
Helmholtz (κ = 1/8)	0.64±0.09	1.09±0.16	1.64±0.22
Hard Priors	0.64	1.13	0.23

(b)

3.2. Breast geometry - effect of data noise level

The techniques described in Sec. 2 were used to reconstruct images from synthetic data with 1, 3, 5 and 10% Gaussian distributed noise to see the effect of data noise level on the reconstruction techniques. The breast geometry (and the optical properties) were equivalent to the previous section (Fig. 1(a)), however, perfect spatial priors were used. The same FEM mesh as described above was employed in the forward and reconstruction problems. Optical properties of region '0' were used as initial guess for the iterative procedure. The regularization parameter (λ) and stopping criterion was chosen according to each data noise level.

3.3. Phantom studies

A multi-layered gelatin phantom (86 mm diameter, 25 mm height) was fabricated with different optical properties using heated mixtures of water (80%), gelatin (20%) (G2625, Sigma Inc.), India ink for absorption, and TiO_2 (titanium oxide powder, Sigma Inc.) for scattering[15] (see Fig. 3). Different layers of gelatin were constructed by successively hardening gel solutions

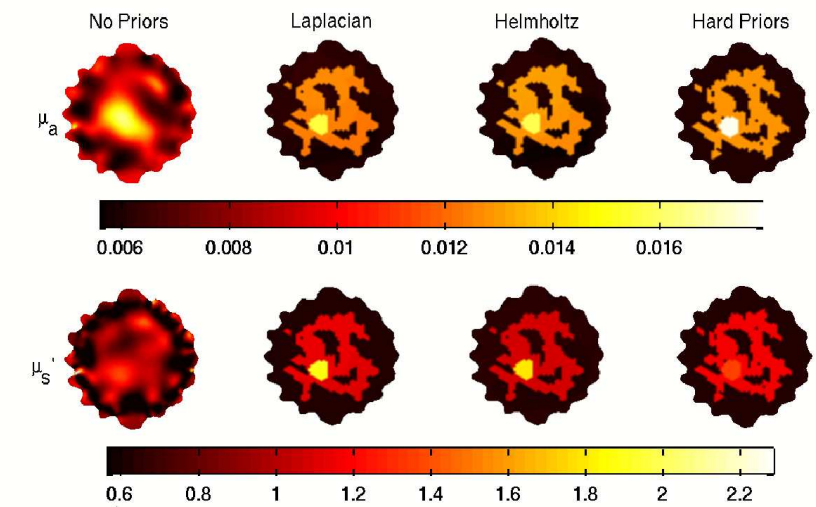

(a)

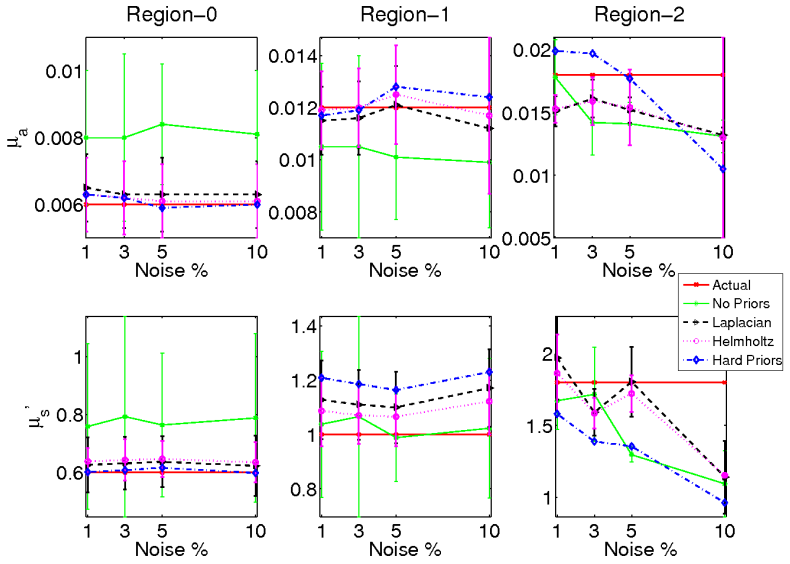

(b)

Fig. 2. (a) Reconstructed μ_a and μ_s' images from different techniques with simulated data having 5% random noise and perfect structural priors (actual images are shown in the first column of Fig. 1(a)). The first column shows the reconstruction results without the use of prior information. The middle two columns use soft prior structural information while the last row shows the result with hard prior information. In the Helmholtz case, $\kappa = 1/8$ mm^{-1} (BPE) was used. (b) The mean values and standard deviations (plotted as error bars) in μ_a and μ_s' for different regions of breast geometry (labeled in actual image) with increasing noise level (1% to 10 %).

containing different amounts of ink and TiO_2. A cylindrical hole (diameter of 16 mm and height of 24 mm) was filled with liquid to mimic the tumor. The first column in Fig. 4 shows the axial cross-section of three-layers of the phantom (Fig. 3) where the region labeled '0' has the optical properties (μ_a = 0.0065 mm^{-1} and μ_s' = 0. 65 mm^{-1}), similar to the typical fatty layer in the breast[6] and a thickness of 10 mm. The fibroglandular layer (diameter 76mm) has optical properties (region labeled '1') of μ_a = 0.01 mm^{-1} and μ_s' = 1.0 mm^{-1}. The tumor (represented by the region labeled '2') has a diameter of 16 mm with optical properties of μ_a = 0.02 mm^{-1} and μ_s' = 1.2 mm^{-1}. The optical properties were validated by measuring large cylindrical samples of each layer. Appropriate mixtures of Intralipid and India ink were used to achieve the desired optical parameters of the tumor. Data was acquired using a clinical NIR system[35] where the fibers were marked and photographed to extract region information (analogous to MRI images). This regional information was used to label the corresponding regions in the FEM mesh[15]. A mesh of 1785 nodes (corresponding to 3418 linear triangular elements) was used for the diffusion model calculations and a mesh having 1360 nodes was used in the reconstruction[36]. The meshes considered in this work have uniform nodal density across the total computation volume. NIR data was calibrated using a reference homogenous phantom to obtain initial optical properties estimates and minimize the variation between the 16 optical channels according to standard practice in human imaging studies[32, 33].

Fig. 3. Photograph for gelatin phantom (representing the idealized two-dimensional cross-sectional geometry shown as first column in Fig. 4(a)) used in the experimental studies.

4. Results

Reconstructed μ_a and μ_s' images obtained from the noisy simulated data with imperfect (7% error) glandular layer priors using the methods described in Sec. 2 are shown in Fig. 1. Using hard priors, the total number of unknowns is reduced to 6 parameters (μ_a and μ_s' for each of the 3 regions) and these images are presented in the last column of Fig. 1(a). The images from two different approaches of soft-priors are shown in the middle 2 columns; the first column shows the expected results. For the Helmholtz case, κ = 1/8 mm^{-1} (BPE) was used, where 8 mm is the diameter of the tumor. Cross-sectional plots of the reconstructed μ_a and μ_s' distributions along the dotted line in Fig. 1(a) (first column) are provided in Fig. 1(b). Table 1(a) and (b) show the mean and standard deviation of the optical property estimations in each region of the reconstructed images. Note that the NIR reconstruction procedure without prior information (not shown) did not generate meaningful images in this complex case.

Figure 2(a) shows the reconstructed images from the data with 5% noise using all four techniques described in Sec. 2. The first column of Fig. 1(a) shows the actual distribution of optical properties. Figure 2(b) shows the mean and standard deviation values (as error bars) of reconstructed images using different techniques for different regions of the breast geometry with increasing data noise level. In the Helmholtz case, κ = 1/8 mm^{-1} (BPE) was used. The actual values are also plotted for the comparison. It can be clearly seen Laplacian regularization

gives lesser standard deviation for the absorption coefficient (μ_a) reconstruction compared to the Helmholtz structure. On the other hand, Helmholtz structure performs better than Laplacian in the case of scattering coefficient (μ_s').

A photograph of the phantom used to collect data at 785nm with 16 fibers in a single plane (giving 240 measurements) is shown in Fig. 3. Images obtained from the procedures described in Sec. 2 are presented in Fig. 4(a) along with cross-sectional plots of the reconstructed μ_a and μ_s' distributions in Fig. 4(b). Table 2(a) and (b) show the mean and standard deviation of the optical property estimations in each region of the reconstructed images. Here also, for Helmholtz case, the BPE ($\kappa = 1/16$ mm^{-1}) was used. Figure 5(a) gives the results for different values of κ (given on the top of the each column, true distribution is shown as first column in Fig. 4(a)) in the Helmholtz case. Corresponding cross-sections are plotted in Fig. 5(b). The mean and standard deviation values for each of this case are also given in Table 2(a) and (b).

5. Discussion

The reconstructed results (Fig. 1, 2, 4 and 5) show that the structural priors improve the reconstructed image quality dramatically. The penalized problem formulation (different type of regularizations) generates smoother images resulting in smaller standard deviations from the mean values (see Table-2) as compared to the generalized problem that does not incorporate prior information.

The hard-prior case produces significant optical property value error when the structural a priori information is imperfect in the breast geometry (Fig. 1 and Table-1). In this case, a 7% variation in the definition of the glandular layer caused false estimates of the optical properties. On the other hand, soft-priors (Laplacian and Helmholtz) yield good estimates for each layer. Hard-priors over-estimate the tumor absorption coefficient by 360% and under-estimate its scattering coefficient by 88% (Fig. 1). Soft-priors are within 6% of the expected values even with the error in the structural prior. Note that in this particular case, hard-priors failed when 7% of glandular layer made as a fatty layer, yet below this error value it gave reasonable estimates of optical properties. It is also important to realize that this is only a test case of the spatial-prior error progation. There is not enough *in-vivo* data for a systematic investiagion of spatial-error propagation in the reconstruction procedures, especially in the hard-priors case.

With perfect structural priors, increasing the data noise level also increases the quantification error in the reconstructed images (Fig. 2(a) and(b)). Hard–Priors clearly fail in quantifying the tumor optical properties as the data noise level increases. Soft–Priors does better in the quantification than Hard–Priors. It is also evident that incorporation of structural information is key for accurate quantification of the optical properties. The experimental results (Fig. 4) from the three-layer gelatin phantom (Fig. 3) also show that incorporation of perfect structural information improves the quantification and quality of the reconstructed images. Specifically, the mean and standard deviation of the reconstructed optical property values in each region are both more accurate and more precise where the priors are included. The mean values (Table-2) show that the absorption coefficient for the Region-0 (fat) is under-estimated by 77% in the case of the Helmholtz regularization (BPE). This error can be explained by the fact that the Euclidean distance between the nodes was used rather than the distance between the nodes along the boundary of a particular region. Both Laplacian and Hard-Priors over estimate the scattering coefficient of the tumor region by a factor of 2. It is known that the photon path length is affected by the scattering coefficient. By constraining the problem based on the distance, one can expect to estimate the scattering better. In this experimental case, table-2 indicates that the Helmholtz technique produces more quantitative accuracy for the scattering coefficient estimation of the tumor and the Laplacian technique is best for the absorption coefficient estimation (as well as Fig. 2 and 4). Usage of the Helmholtz-type form for the diffusion part and the Laplacian-

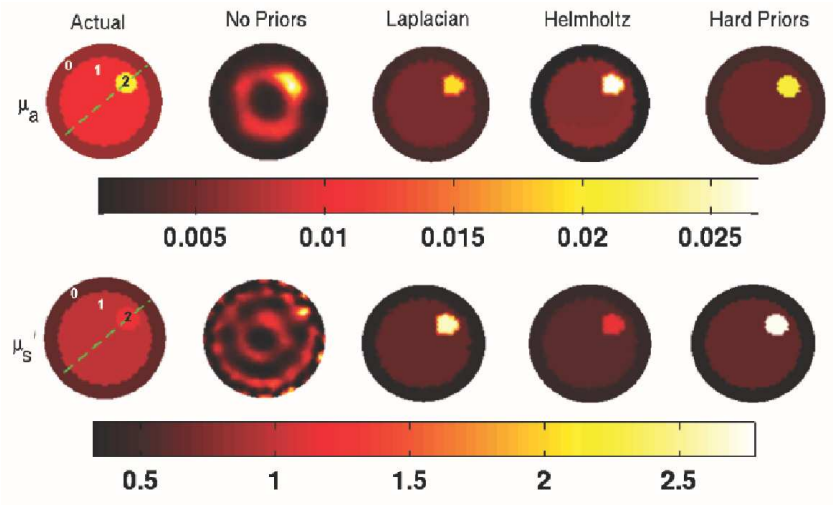

(a)

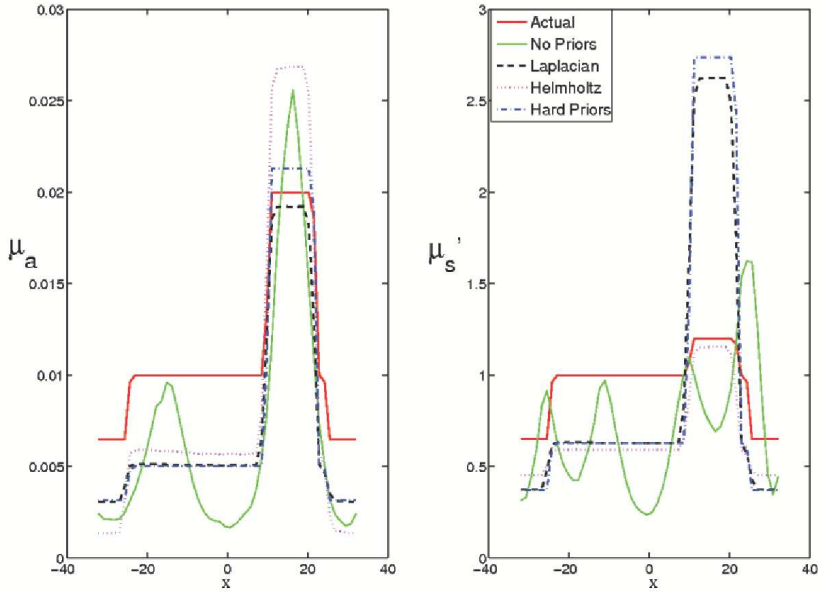

(b)

Fig. 4. (a) Actual μ_a and μ_s' distributions (axial cross-section) of phantom (Fig. 3) case are shown in the first column. Optical properties for the region labeled '0' are: μ_a = 0.0065 mm^{-1} and μ_s' = 0. 65 mm^{-1}. Region '1' values are: μ_a = 0.01 mm^{-1} and μ_s' = 1.0 mm^{-1}. Region '2' (tumor) values are: μ_a = 0.02 mm^{-1} and μ_s' = 1.2 mm^{-1}. Reconstructed μ_a and μ_s' distribution from different techniques (discussed in Sec. 2) from the experimental phantom data. Second column of images does not use prior information. The middle rows use soft prior structural information and the last row of images were recovered with hard priors. In the Helmholtz case, κ = 1/16 mm^{-1} (BPE) was used. (b) Cross-sectional plots along the dotted line in the actual image (see first column of (a)) of the true and reconstructed μ_a and μ_s' distributions.

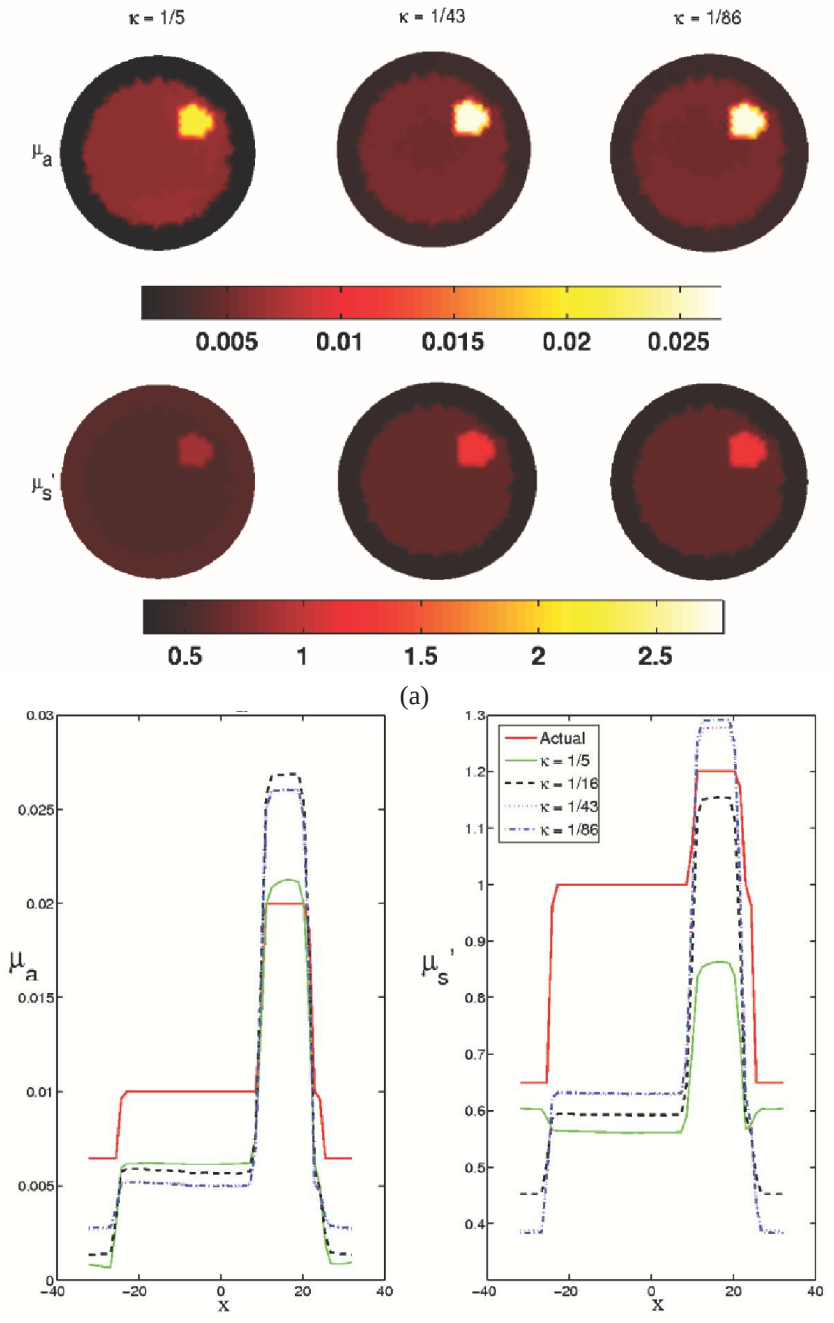

Fig. 5. (a) Reconstructed μ_a and μ_s' images from the experimental phantom data using Helmholtz-type regularization matrix for different values of κ, which are given at the top of each column. (b) Cross-sectional plots along the dotted line of the actual images in Fig. 4(a) (first column) are shown with the data from reconstructed μ_a and μ_s' images in (a). The best prior estimate (BPE) case (κ = 1/16 mm^{-1}) is also presented for comparison.

type form for the absoprtion part (in Eq. 8), may lead to a better estimation of both optical properties, which will be considered as a future work. Under estimation of optical properties in the regions '0' and '1' can be attributed to the random fluctuations in heating/cooling of the gelatin solution especially in making layered phantom, which eventually changes optical properties. Moreover, ink and TiO_2 particles settling to the bottom, making the mixture less homogenous also causes the change optical properties. These type of errors are more common for layered gelatin phantoms[37].

Table 2. Mean and standard deviation of the reconstructed (a) μ_a and (b) μ_s' values in different regions (labeled in first column of Fig. 4(a)) recovered from the experimental phantom data. The corresponding reconstructed images are shown in Fig. 4(a) and 5(a).

Methods	*Region-0*	*Region-1*	*Region-2*
Actual	0.0065	0.01	0.02
No Priors	0.0025±0.0010	0.0045±0.0022	0.0120±0.0090
Laplacian	0.0031±0.0002	0.0051±0.0005	0.0174±0.0029
Helmholtz (κ = 1/16)	0.0015±0.0005	0.0058±0.0009	0.0241±0.0043
Hard Priors	0.0032	0.005	0.0213
Helmholtz (κ = 1/5)	0.0009±0.0006	0.0061±0.0008	0.0191±0.0031
Helmholtz (κ = 1/43)	0.0027±0.0003	0.0052±0.0007	0.0234±0.0043
Helmholtz (κ = 1/86)	0.0022±0.0005	0.0061±0.0032	0.0192±0.0044

(a)

Methods	*Region-0*	*Region-1*	*Region-2*
Actual	0.65	1.0	1.2
No Priors	0.64±0.40	0.66±0.27	0.76±0.16
Laplacian	0.38±0.03	0.63±0.07	2.37±0.41
Helmholtz (κ = 1/16)	0.46±0.02	0.59±0.02	1.08±0.12
Hard Priors	0.37	0.63	2.74
Helmholtz (κ = 1/5)	0.60±0.01	0.57±0.01	0.82±0.06
Helmholtz (κ = 1/43)	0.39±0.03	0.63±0.03	1.19±0.13
Helmholtz (κ = 1/86)	0.39±0.03	0.63±0.04	1.21±0.14

(b)

Theoretically Helmholtz and Laplacian structures are identical when $\kappa = 0$ (equivalently l is large). Figures 5(a) and (b) (as well as Table-2) show that when $\kappa = 1/86$ mm^{-1} (l = 86 mm is the diameter of the domain), Laplacian and Helmholtz structures give reasonably close reconstruction values of optical properties, which indicates the expected trend presented in this paper for the two methods. It also indicates that the BPE case ($\kappa = 1/16$ mm^{-1}) gives the best results, as the priors applied are close to the true structure of the feature (tumor). These results also indicate that unreasonable constraints (like $\kappa = 1/5$ mm^{-1}, Fig. 5(a) first column) makes the estimation problem amplify the noise resulting in physiologically invalid (scattering coefficient is greater for fatty layer compared to fibroglandular layer) estimates of optical properties. In the tumor region, as κ decreases, the estimated values of optical parameters become closer to expected values (Table-2 and Fig. 5, $\kappa = 1/43$ and $\kappa = 1/86$ cases). This is due to the correlation length becoming larger, making the covariance in the neighboring nodes larger.

In this study, it is shown that imperfect priors (commonly caused by improper image segmentation and image artifacts in MRI or X-ray) can lead to error-prone results in the hard-prior case whereas soft-priors are more immune to uncertainty in the prior data. It is also shown that the techniques used to incorporate the soft structural prior information influences the image outcome, which may lead to improvements in image accuracy if properly implemented. Srini-

vasan et. al[38] have found that 5% error in optical properties introduces approximately 45% error in the chromophore concentration when a limited number of wavelengths are used for imaging. The correct "soft" inclusion of *a priori* information therefore can be expected to lead to a more accurate quantification of chromophore concentrations as well. It should be noted that over-weighting of the penalty term in the problem formulation may make the solution ignore the data-model misfit and emphasize smooth feature extraction. The techniques developed in this work were applied for two-dimensional test objects, and can be easily extended to three-dimensional case. A more extensive study of this is left for future investigations.

6. Conclusions

This work has investigated several ways of incorporating structural information into an iterative image reconstruction. The results have been supported by gelatin phantom experiments that represent multi-layered structure which is commonly found in breast tissue with adipose (fatty) tissue on the exterior and fibroglandular tissue nearer to the interior. Soft-priors allow the tissue optical properties to vary within predefined regions, unlike hard-priors which constrain these zones to be homogeneous. Hard-priors were found to perform poorly when the prior information contained area errors as small as 7% which can easily be produced by most segmentation algorithms. True boundary extraction from MRI images introduces unavoidable segmentation and discretization errors that are better tolerated when the structural information is encoded through the soft-prior approach involving a penalty matrix.

The results reported here indicate that the optical properties of different tissue types can be quantified more accurately when their estimation is properly guided by "soft" structural *a priori* information. The problem formulation and results presented in this work indicate that data from other imaging modalities such as ultrasound or x-ray tomography, could also be used as the source of the structural prior. In the experimental cases investigated, the Helmholtz structure using best priors gave a better estimation of scattering coefficient of the target (tumor). However, the Laplacian type of regularization leads to more superior absorption coefficient estimate. So it is reasonable to conclude that Laplacian structure gives the best estimates of total hemoglobin concentration (Hb_T), hemoglobin oxygen saturation ($S_tO_2\%$) and water fraction (H_2O) (which are the main absorbers). Helmholtz structure gives the best estimates of the scattering power and scattering amplitude (scattering parameters). The framework presented here can also be extended to other regularization terms such as total variation minimization or spectral prior constraints, which may be studied in future work.

Acknowledgments

Authors are grateful to Professor Daniel R. Lynch for the useful discussions and comments on this paper. P.K.Y. acknowledges the DOD Breast Cancer predoctoral fellowship (BC050309). This work has been sponsored by the National Cancer Institute through grants RO1CA78734, PO1CA80139, and DAMD17-03-1-0405.

Implementation of a computationally efficient least–squares algorithm for highly under-determined three-dimensional diffuse optical tomography problems

Phaneendra K. Yalavarthy[†,ϕ], Daniel R. Lynch[†], Brian W. Pogue[†,*], Hamid Dehghani[†,§], and Keith D. Paulsen[†]

[†] *Thayer School of Engineering, Dartmouth College, Hanover, NH 03755 USA*
[§] *School of Physics, University of Exeter, Stocker Road, Exeter, EX4 4QL, UK*
[ϕ] *Current address: Department of Radiation Oncology, Washington University School of Medicine, St. Louis, MO 63110 USA*

[*] *e-mail: Pogue@dartmouth.edu*
Tel:(603)-646-3861, Fax:(603)-646-3699

Submitted to
Medical Physics
December 7, 2007

ABSTRACT

Three-dimensional (3D) diffuse optical tomography (DOT) is known to be a non-linear, ill-posed and sometimes under-determined problem, where regularization is added to the minimization to allow convergence to a unique solution. In this work, a generalized least-squares (GLS) minimization method was implemented, which employs weight matrices for both data-model misfit and optical properties to include their variances and covariances, using a computationally efficient scheme. This allows inversion of a matrix that is of dimension dictated by the number of measurements, instead of by the number of imaging parameters. This increases the computation speed up to four times per iteration in most of under-determined 3D imaging problems. An analytic derivation, using the Sherman-Morrison-Woodbury identity, is shown for this efficient alternative form and it is proven to be equivalent, not only analytically, but also numerically. Equivalent alternative forms for other minimization methods, like Levenberg-Marquardt (LM) and Tikhonov, are also derived. 3D reconstruction results indicate that the poor recovery of quantitatively accurate values in 3D optical images can also be a characteristic of the reconstruction algorithm, along with the target size. Interestingly, usage of GLS reconstruction methods reduces error in the periphery of the image, as expected, and improves by 20% the ability to quantify local interior regions in terms of the recovered optical contrast, as compared to LM methods. Characterization of detector (PMTs) noise have enabled the use of the GLS method for reconstructing experimental data and showed a promise for better quantification of target in 3D optical imaging. Use of these new alternative forms becomes effective when the ratio of the number of imaging property parameters exceeds the number of measurements by a factor greater than 2.

Keywords: near infrared, diffuse optical tomography, three-dimensional imaging, image reconstruction, inverse problems, least squares minimization.

1. Introduction

Diffuse optical tomography (DOT) uses near infrared wavelengths (600-1000 nm) to obtain optical absorption and scattering images for characterizing functional properties of the tissue under investigation.[1–4] The most important step in forming these images is solving the inverse problem, i.e. estimating the optical properties by matching the experimental data with modeled results in the least-squares sense.[3,5,6] This problem is typically ill-posed and ill-determined depending on the noise in the data, the number of measurements and the dimensions of the parameter space.[6] Even though light travels in three-dimensions (3D), most of the numerical models reported in the literature have been two-dimensional (2D) because of computational considerations. Moreover, the 3D DOT imaging problem is more under-determined relative to the 2D case and has been found to generate poor quantitative estimates of the optical properties when compared to 2D results.[7–14] Several methods have appeared in the literature describing efficient 3D computations,[11,14,16] but no unified approach to the problem has been discussed. Recently, a generalized least-squares (GLS) minimization scheme was presented for 2D DOT image reconstruction.[17] This paper reports a computationally efficient approach for implementing GLS minimization in 3D which shows an improvement in the quantification of optical properties relative to earlier studies. Even though the focus is on GLS implementation, equivalent forms for other methods are also presented in light of the GLS framework.

The inverse problem in DOT is solved by minimizing the objective function (Ω) over the range of optical properties (μ). Methods based on gradient optimization, which do not require an explicit inversion of the Hessian matrix [1] (in general some form of $\mathbf{J}^T\mathbf{J}$, $\mathbf{J}$ being the Jacobian) are known to be computationally efficient.[18,19] But these methods require an optimization scheme, which can be thought of as an inner iteration, for choosing the step-size, and are not as straight forward as a direct inversion of the matrix. Alternatively, the full-Newton methods require calculation of the Jacobian ($\mathbf{J}$), the forward data, and inversion of the dense Hessian matrix at each iteration. Because full-Newton methods are relatively easy to implement, they are widely used for DOT image reconstruction even though they require large matrix inversions at every iteration. Thus, while the full-Newton method is ideal for small problems, it rapidly becomes intractable for larger domains, such as those encountered in 3D imaging problems. This manuscript presents a formal approach, using the Sherman-Morrison-Woodbury identity, to construct a more efficient alternative forms of update equations of GLS and Levenberg-Marquardt (LM) minimization schemes, which generates a Hessian matrix to invert. The dimension of this Hessian is dictated by the number of measurements, rather than the number of parameter estimates which can

[1] Here, Hessian approximates the second derivative, this can be some form equivalent to $\mathbf{J}^T\mathbf{J}$ or $\mathbf{J}\mathbf{J}^T$

be considerably lower for highly under-determined problems, and therefore, much more efficient computationally. This equivalent form is also shown for other common minimization method, namely Tikhonov.

Later part of this paper describes a way to characterize the systematic noise using a simple analytical formula, when photomultiplier tube (PMT) used as a detector. Characterizing noise behavior of the experimental data lead to use of the GLS technique in the experimental data case and it is also shown that usage of noise characterstics will lead to better quality and quantification of target in a experimental test case.

2. Diffuse Optical Tomography: Forward Problem

Near-infrared (NIR) light propagation in a biological tissue like breast can be modeled using the Diffusion Equation (DE)[6,20] which in the frequency domain, becomes

$$-\nabla.D(r)\nabla\Phi(r,\omega) + (\mu_a(r) + i\omega/c)\Phi(r,\omega) = Q_o(r,\omega) \tag{1}$$

where the optical diffusion and absorption coefficients are given by $D(r)$ and $\mu_a(r)$, respectively. The light source, represented by $Q_o(r,\omega)$, is modeled as isotropic. $\Phi(r,\omega)$ is the photon fluence rate at a given position r. The light modulation frequency is denoted by ω, where $\omega = 2\pi$f, (here f = 100 MHz). The velocity of light in tissue is represented by c, which is assumed to be constant. Note that

$$D(r) = \frac{1}{3[\mu_a(r) + \mu_s'(r)]} \tag{2}$$

where $\mu_s'(r)$ is the reduced scattering coefficient which is defined as $\mu_s' = \mu_s(1-g)$. μ_s is the scattering coefficient and g is the anisotropy factor. The finite element method (FEM) is used to solve equation (1) to generate modeled data ($G(\mu)$) for a given distribution of optical properties (μ),[11,13,21] where $\mu = [\mu_s'(r); \mu_a(r)]$. A Type-III boundary condition is employed to account for the refractive-index mismatch at the boundary.[22] Under the Rytov approximation, the data (y) becomes the natural logarithm of the amplitude (A) and phase (θ) of the frequency-domain signal; $y = [lnA; \theta]$.

3. Diffuse Optical Tomography: Inverse Problem

3.A. Levenberg-Marquardt (LM) Minimization

The most-common approach for solving the inverse problem in DOT is Levenberg-Marquardt (LM) minimization.[1,6,11,13,17,20,23,24] A detailed discussion of this method is available in Ref.[17] and it is only briefly reviewed here.

The objective function[25,26] for this approach is defined as

$$\Omega = \|y - G(\mu)\|^2 \tag{3}$$

where y is the experimental data and $G(\mu)$ is the modeled response. Minimization of this objective function with respect to μ is achieved by setting the first-order derivative equal to zero

$$\frac{\partial \Omega}{\partial \mu} = \mathbf{J}^T \delta = 0 \tag{4}$$

where δ is the data-model misfit, $\delta = y - G(\mu)$, and $\mathbf{J}$ represents the Jacobian ($\mathbf{J} = \frac{\partial G(\mu)}{\partial \mu}$). Due to the ill-conditioned nature of the problem, the update equation for the optical properties at iteration 'i' is regularized to be

$$\triangle \mu_i = \left[\mathbf{J}^T\mathbf{J} + \alpha \mathbf{I}\right]^{-1} \mathbf{J}^T \delta_{i-1} \tag{5}$$

or equivalently (See Appendix-A.2)

$$\triangle \mu_i = \mathbf{J}^T \left[\mathbf{J}\mathbf{J}^T + \alpha \mathbf{I}\right]^{-1} \delta_{i-1} \tag{6}$$

where $\triangle \mu_i$ represents the update of the optical property parameters at the i^{th} step. α is the regularization parameter, which monotonically decreases with increasing iteration (always > 0).[26] In this approach (Eq. 5), the Jacobian is normalized by its optical properties. Moreover, α is chosen empirically (it typically starts at 10 and reduced by a factor of $10^{0.25}$ at every following iteration after being multiplied by the maximum of the diagonal values of $\mathbf{J}\mathbf{J}^T$.[17,27]). The iterative procedure is stopped when the L2 norm of the data-model misfit (δ) does not improve (in our experience, by more than 1% because beyond these values the LM procedure can become unstable[17]).

Even though LM minimization or its modified versions have been used successfully for DOT image reconstruction,[1,6,11,13,17,20,23,24,27] the final image depends on the choice of α due to the ill-conditioned nature of the problem. Moreover, the approach ignores the noise characteristics of the data and optical properties. A more systematic and generalized method for image reconstruction can be based on GLS minimization. The GLS scheme is discussed extensively in Ref.[17] and is only briefly reviewed here.

3.B. Generalized Least Squares (GLS) Minimization

In GLS, the objective function is given by[17,28]

$$\Omega = (y - G(\mu))^T \mathbf{W}_\delta (y - G(\mu)) + (\mu - \mu_0)^T \mathbf{W}_{\mu-\mu_\mathbf{0}} (\mu - \mu_0) \tag{7}$$

where $\mathbf{W}_\delta$ and $\mathbf{W}_{\mu-\mu_\mathbf{0}}$ are the weight matrices for the data-model misfit (δ) and optical properties (μ-μ_0), respectively. Note that $\mathbf{W}_\delta = (\mathbf{C}_\delta)^{-1}$, where $\mathbf{C}$ represents the covariance

matrix, and similarly $\mathbf{W}_{\mu-\mu_\mathbf{0}} = (\mathbf{C}_{\mu-\mu_\mathbf{0}})^{-1}$ (see Appendix:A-4 of Ref.[28]). These weight matrices are symmetric and positive definite (because they are inverses of covariance matrices). No regularization parameter is involved because the weight matrices include the noise characteristics of the experimental data and optical properties.[17] Similarly to the LM approach, minimization of Ω (Eq. 7) is accomplished by setting the first derivative of Ω with respect to μ equal to zero:

$$\frac{\partial \Omega}{\partial \mu} = \mathbf{J}^T \mathbf{W}_\delta \delta - \mathbf{W}_{\mu-\mu_\mathbf{0}}(\mu - \mu_0) = 0. \tag{8}$$

Linearizing the problem leads to the iterative update equation (for i^{th} iteration)[17]

$$\triangle \mu_i = \left[\mathbf{J}^T \mathbf{W}_\delta \mathbf{J} + \mathbf{W}_{\mu-\mu_\mathbf{0}}\right]^{-1} \left(\mathbf{J}^T \mathbf{W}_\delta \delta_{i-1} - \mathbf{W}_{\mu-\mu_\mathbf{0}}(\mu_{i-1} - \mu_0)\right) \tag{9}$$

Explicit definitions of the weight matrices ($\mathbf{W}_\delta$ and $\mathbf{W}_{\mu-\mu_\mathbf{0}}$) are given in Ref.[17] Although any number of forms for $\mathbf{W}_{\mu-\mu_\mathbf{0}}$ can exist, only one is considered here, specifically, where the covariance matrix is defined as[17]

$$[\mathbf{C}_{\mu-\mu_\mathbf{0}}]_{ij} = (\sigma_{\mu-\mu_0})^2 \left(1 + \frac{r_{ij}}{l}\right) e^{-\frac{r_{ij}}{l}} \tag{10}$$

with l being the correlation length (here $l = 15$ mm) and r_{ij} being the distance between the FEM nodes i and j. $(\sigma_{\mu-\mu_0})^2$ is the expected variance of $\mu - \mu_0$. Strategies for calculating the expected variance are given in Ref.[17] In this work, the expected variance is determined from the prior knowledge that the expected contrast between tumor and normal tissue is about 50-400%. To demonstrate the robustness of the GLS reconstruction procedure, for the results discussed here, the variance was chosen to be $(4 * \mu)^2$. Both weight matrices, $\mathbf{W}_\delta$ and $\mathbf{W}_{\mu-\mu_\mathbf{0}}$, are computed before the reconstruction procedure begins, whereas the Jacobian ($\mathbf{J}$), and modeled data, $G(\mu)$, are calculated at each iteration. The iterative procedure is stopped when the L2 norm of the data-model misfit (δ) does not improve by more than 0.001%. Beyond these values, the round-off error dominates.

3.B.1. GLS Implementation

The parameters recovered in the case of this GLS scheme are $(\mu_s'; \mu_a)$, which is different from some previous approaches that estimate $(D; \mu_a)$. The later case has a mismatch because the units of D are mm whereas those of μ_a are mm^{-1}. In its implementation typically the whole equation is normalized by the optical properties (outlined in Ref.[17]) which becomes computationally intensive especially for GLS in 3D because the update equation must be left and right multiplied by the optical properties at every iteration. Here, the GLS problem was reformulated in terms of $(\mu_s'; \mu_a)$, so that both parameters have same units (mm^{-1}). While this is a relatively minor alteration in the form of the algorithm, it has important implications for the computational time required for matrix preconditioning.

A simple transformation converts the diffusion part of the Jacobian ($\frac{\partial G(\mu)}{\partial D}$) to its scattering component ($\frac{\partial G(\mu)}{\partial \mu_s'}$):

$$\frac{\partial G(\mu)}{\partial \mu_s'} = \frac{\partial G(\mu)}{\partial D}\ \frac{\partial D}{\partial \mu_s'} \tag{11}$$

Using Eq. 2

$$\frac{\partial D}{\partial \mu_s'} = \frac{1}{3}\left(\frac{-1}{[(\mu_a + \mu_s')]^2}\right) = -3D^2 \tag{12}$$

and substituting Eq. 12 in Eq. 11, leads to

$$\frac{\partial G(\mu)}{\partial \mu_s'} = \frac{\partial G(\mu)}{\partial D}(-3D^2) \tag{13}$$

After this transformation (Eq. 13) the Jacobian ($\mathbf{J}$) has the form

$$\mathbf{J} = \begin{bmatrix} \frac{\partial lnA_1}{\partial \mu_{s1}'} & \frac{\partial lnA_1}{\partial \mu_{s2}'} & \cdots & \frac{\partial lnA_1}{\partial \mu_{sNN}'} & \frac{\partial lnA_1}{\partial \mu_{a1}} & \frac{\partial lnA_1}{\partial \mu_{a2}} & \cdots & \frac{\partial lnA_1}{\partial \mu_{aNN}} \\ \frac{\partial \theta_1}{\partial \mu_{s1}'} & \frac{\partial \theta_1}{\partial \mu_{s2}'} & \cdots & \frac{\partial \theta_1}{\partial \mu_{sNN}'} & \frac{\partial \theta_1}{\partial \mu_{a1}} & \frac{\partial \theta_1}{\partial \mu_{a2}} & \cdots & \frac{\partial \theta_1}{\partial \mu_{aNN}} \\ \frac{\partial lnA_2}{\partial \mu_{s1}'} & \frac{\partial lnA_2}{\partial \mu_{s2}'} & \cdots & \frac{\partial lnA_2}{\partial \mu_{sNN}'} & \frac{\partial lnA_2}{\partial \mu_{a1}} & \frac{\partial lnA_2}{\partial \mu_{a2}} & \cdots & \frac{\partial lnA_2}{\partial \mu_{aNN}} \\ \frac{\partial \theta_2}{\partial \mu_{s1}'} & \frac{\partial \theta_2}{\partial \mu_{s2}'} & \cdots & \frac{\partial \theta_2}{\partial \mu_{sNN}'} & \frac{\partial \theta_2}{\partial \mu_{a1}} & \frac{\partial \theta_2}{\partial \mu_{a2}} & \cdots & \frac{\partial \theta_2}{\partial \mu_{aNN}} \\ \vdots & \vdots & \cdots & \vdots & \vdots & \vdots & \cdots & \vdots \\ \frac{\partial lnA_{NM}}{\partial \mu_{s1}'} & \frac{\partial lnA_{NM}}{\partial \mu_{s2}'} & \cdots & \frac{\partial lnA_{NM}}{\partial \mu_{sNN}'} & \frac{\partial lnA_{NM}}{\partial \mu_{a1}} & \frac{\partial lnA_{NM}}{\partial \mu_{a2}} & \cdots & \frac{\partial lnA_{NM}}{\partial \mu_{aNN}} \\ \frac{\partial \theta_{NM}}{\partial \mu_{s1}'} & \frac{\partial \theta_{NM}}{\partial \mu_{s2}'} & \cdots & \frac{\partial \theta_{NM}}{\partial \mu_{sNN}'} & \frac{\partial \theta_{NM}}{\partial \mu_{a1}} & \frac{\partial \theta_{NM}}{\partial \mu_{a2}} & \cdots & \frac{\partial \theta_{NM}}{\partial \mu_{aNN}} \end{bmatrix} \tag{14}$$

where NM and NN represents the number of measurements and number of property parameters associated with the FEM mesh, respectively. The implementation of the GLS update equation (Eq. 9) requires assembly of the weight matrix ($\mathbf{W}_{\mu-\mu_\mathbf{0}}$) for simultaneous reconstruction of μ_s' and μ_a and is accomplished by writing Eq. 9 in block matrix form

$$\left\{\left[\begin{array}{c|c} H_{\mu_s'^2} & H_{\mu_s'\mu_a} \\ \hline H_{\mu_s'\mu_a} & H_{\mu_a{}^2} \end{array}\right] + \left[\begin{array}{c|c} W_{\mu_s'-\mu_{s0}'} & 0 \\ \hline 0 & W_{\mu_a-\mu_{a0}} \end{array}\right]\right\}\left[\begin{array}{c} \triangle\mu_{s\,i}' \\ \triangle\mu_{a\,i} \end{array}\right] = \left[\begin{array}{c} (J^T)_{\mu_s'} W_\delta \delta_{i-1} \\ (J^T)_{\mu_a} W_\delta \delta_{i-1} \end{array}\right] - \left[\begin{array}{c} W_{\mu_s'-\mu_{s0}'}\left(\mu_{s\,i-1}' - \mu_{s0}'\right) \\ W_{\mu_a-\mu_{a0}}\left(\mu_{a\,i-1} - \mu_{a0}\right) \end{array}\right] \tag{15}$$

where H represents the Hessian matrix ($\mathbf{J}^T\mathbf{W}_\delta\mathbf{J}$). Here, the cross-terms in the weight matrix ($\mathbf{W}_{\mu-\mu_\mathbf{0}}$) are zero because μ_s' and μ_a are independent parameters in the estimation procedure. Note that the dimensions of the matrices in Eq. 9 are: $\mathbf{J}$: 2NM x 2NN, $\mathbf{W}_{\mu-\mu_\mathbf{0}}$: 2NN x 2NN, $\mathbf{W}_\delta$: 2NM x 2NM, δ = 2NM x 1, and $\triangle\mu$ = 2NN x 1. Most 3D-DOT problems are ill-determined, i.e. NM $\ll$ NN.

Computing an update of the optical properties ($\triangle\mu_i$, from Eq. 9) requires an inversion (or its equivalent) of a large matrix with dimensions 2NN x 2NN. Inverting a matrix of dimension NxN, typically requires an order of N^3 operations and N^2 memory.[28] Hence, any gain in reducing the dimensionality of the matrix to be inverted, will reduce the computation

time cubically and the memory requirement quadratically. An alternative from of Eq. 9, which requires few operations is

$$\triangle\mu_i = \left[\mathbf{I} - \mathbf{C}_{\mu-\mu_\mathbf{0}}\mathbf{J}^T\left(\mathbf{J}\mathbf{C}_{\mu-\mu_\mathbf{0}}\mathbf{J}^T + \mathbf{C}_\delta\right)^{-1}\mathbf{J}\right]\left\{\mathbf{C}_{\mu-\mu_\mathbf{0}}\mathbf{J}^T\mathbf{W}_\delta\delta_{i-1} - (\mu_{i-1} - \mu_0)\right\} \qquad (16)$$

Full derivation of this alternative form is given in the appendix (A.1) along with the equivalent expressions for other minimization methods. Eq. 16 requires an inversion of a matrix with dimensions 2NM x 2NM (same is true for Eq. 6).

Note that the covariance/weight matrices are calculated before the start of the iterative procedure and are used throughout the iteration. For nodes where the sensitivity (column sum of Jacobian) fell below 1% of the maximum sensitivity, the expected variance of the optical properties was chosen to be 1% of background μ (in Eq. 10).

4. Simulation Studies: Three-dimensional Test Problem

For all numerical experiments discussed here, the imaging domain was chosen to be cylindrical (as shown in Fig. 1) with a diameter of 84 mm and height of 109 mm. The background optical properties were $\mu_a = 0.01$ mm^{-1} and $\mu_s' = 1.0$ mm^{-1}. Two meshes were used: (1) a cylinder consisting of 21,440 nodes corresponding to 110,483 linear tetrahedral elements for the forward model and (2) a cylinder having 9,211 nodes corresponding to 45,980 linear tetrahedral elements for the reconstruction. The data-collection geometry consisted of 48 fibers that were arranged in a circular, equally-spaced fashion in three layers spaced 10 mm apart (Fig. 1), with 16 fibers per plane. One fiber was used at a time as the source while the fibers in the same "source fiber plane" were used as detectors to generate 720 (3x16x15) measurement locations or a total of 1440 values (720 lnA data points and 720 θ data points). The sources were modeled as a Gaussian profile with a full-width half maximum of 3 mm to represent the distribution used in an experimental setup.[29] The source was also placed one mean transport scattering distance inside the boundary.

Both spherical and cylindrical objects were considered as targets. The cylindrical target had a contrast of 2:1 with the background in both μ_a and μ_s' and a diameter of 15 mm. It extended in Z-direction throughout the domain (height of 109 mm) and was placed at the center (at (0,0), first row of Fig. 5) and near the boundary (at (30,0)). Two-dimensional cross-sections of both reconstructed and actual 3D volumes are displayed in increments of 5 mm spanning from z = -25 mm to z = 25 mm (from left-hand side to right-hand side) are shown in Figs. 3, 5, and 6. Cross-section below z= -25 mm and beyond z = 25 mm did not show any deviation from the starting values of iterations as the sensitivity in this region is almost negligible compared to the rest of the domain, so these cross-sections are

omitted for display purposes. Measurements with a noise level of 1% were assumed as the experimental data (y) in most of the cases discussed here. The noise variance was also used with GLS reconstruction algorithm.[17] The background optical properties were selected as starting values for the iterative image reconstruction procedures discussed in Sec.3. All computations were carried out on a Linux work station with an AMD Dual Core Opteron 280 processor (2.2 GHz) with 8GB of RAM.

5. Phantom Studies

5.A. Data variance estimation

Use of weight matrices in the GLS scheme ($\mathbf{W}_\delta$ in Eq. 9) requires an estimation of data variance, which requires experimental characterization of the expected values, prior to patient/phantom imaging. This was achieved by tracking the detected voltage measured at the photo multiplier tube (PMT). PMTs are used as a detectors in the experimental system at Dartmouth, details of the experimental system are given in Ref.[29] Note that this characterization includes only systematic errors associated with low signal levels, but errors due to poor fiber-tissue coupling are not accounted for in this model.

Starting from the assumption that the detected signal using a PMT in diffuse optical imaging is shot noise limited leads to

$$\sigma = \sqrt{N} \tag{17}$$

where σ is the standard deviation in the detected signal and N is the number of photons reaching the PMT. The voltage (V) measured at the PMT is directly proportional to N, which also implies that amplitude (A) of the detected frequency domain signal (y) is proportional to this voltage. This is written as

$$\begin{gathered} A \propto V \implies A = kV \\ \sigma(A) = k\sigma(V) \end{gathered} \tag{18}$$

here, k acts as a proportionality constant. In the reconstruction procedure, the Rytov approximation is used, leading to data being represented as lnA rather than A. If $f(x)$ is a function of x and is continuous and differentiable, then

$$\sigma\left(f(x)\right) = \frac{\partial f(x)}{\partial x}\sigma(x) \tag{19}$$

similar to the previous equation (Eq. 19), writing the standard deviation of lnA leads to

$$\sigma(lnA) = \frac{1}{A}\sigma(A) \tag{20}$$

now using Eq. 18 leads to

$$\sigma(lnA) = \frac{\sigma(V)}{V} \tag{21}$$

From the above equation (Eq. 21), it can be concluded that the variance in data (σ^2) can be known by measuring the deviation in the PMT voltage (V).

To measure the deviation in the measured signal, a series of light signal measurements were taken through a homogeneous intralipid phantom experiments were conducted with increasing levels of blood (HbT) concentration, varying from 7.3 μM to 36 μM, leading to a decrease in the measured PMT voltage. To achieve this, the gain of the PMT was kept at 0.9. A concise discussion of the PMT gain setting in the system characterization is given in Ref.[29] A single source and the farthest detector was used for these transmission measurements. For every concentration, 200 data points were collected to estimate the deviation in the measured voltage using the same gain settings. The approach for the characterization is similar to the one described in Ref.,[29] except the raw detected voltage was used here for estimation of the error (or deviation σ). Note also that two sets of diameters, 56 mm and 84 mm, were used to get the voltage in the range of 0-1 volts. This was repeated for all the wavelengths to ensure uniformity of performance in the signal, and to ensure that the obeserved trend was independent of wavelength and gain setting.

Figure 9 gives a plot of error ($\sigma(V)/V$) as a function of measured PMT voltage for 785 nm wavelength. A similar trend was observed for other wavelengths. This plot also gives a deviation in phase ($\sigma(\theta)$) in degrees for the same voltage. Each of these points represents a sample size of 200. The lowest measured voltage of PMT was 0.001 volts. The measured deviations were 1% for lnA and 0.5^o for θ for PMT voltages above 0.005 volts. These values are similar to the ones reported in the literature (Mcbride et. al[29] reported 0.32% for the PMT voltage and 0.48^o in phase). A solid line in Fig. 9 shows these average deviation using $1/\mathrm{V}^2$ fitting (following the shot-noise model). From this plot, the weight matrix for the data-model misfit ($\mathbf{W}_\delta$ in Eq. 9) can be written as

$$[\mathbf{W}_\delta]_{ij} = \begin{cases} 0 & \text{if i} \neq \text{j} \\ \frac{1}{[(5.7/V^2)+0.6]^2} \; for\ lnA\ with\ V \geq 0.001 & \text{if i} = \text{j} \\ \frac{1}{[(1.3/V^2)+0.4]^2} \; for\ \theta\ with\ V \geq 0.001 & \text{if i} = \text{j} \\ 1 \qquad for\ lnA\ with\ V < 0.001 & \text{if i} = \text{j} \\ \frac{1}{(\theta)^2} \qquad for\ \theta\ with\ V < 0.001 & \text{if i} = \text{j} \end{cases} \tag{22}$$

This implies that if the PMT voltage is below 0.001 volts, the signal is considered to be in the noise floor. For the signals above 0.001 volts, the variance can be estimated using $1/\mathrm{V}^2$

fitted curve (Eq. 22). This characterization enables the usage of the GLS scheme in the case of experimental data, with a requirement that the voltage measured at the PMT is available.

5.B. Gelatin Phantom

A multi-layer cylindrical gelatin phantom of diameter 86 mm, height 25 mm was fabricated using different mixtures of India ink for absoprtion and Titanium oxide (TiO_2) for scattering. These different layers of gelatin were fabricated by successively hardening heated gelatin solutions (typically 80% deioinized water and 20% gelatin (G2625, Sigma Inc)) along with different amounts of ink and TiO_2 (Sigma Inc). A cylindrical hole extending in Z-direction (diameter of 16 mm and height of 24 mm) filled with intralipid mixed with india ink acted as a target having the optical properties $\mu_a = 0.02$ mm^{-1} and $\mu_s' = 1.2$ mm^{-1}. The outer layer with optical properties $\mu_a = 0.0065$ mm^{-1} and $\mu_s' = 0.65$ mm^{-1} had a thinkness of 10 mm mimicing the typical fatty layer of the breast.[46] The middle layer with 76 mm diameter, mimicing fibroglandular layer, had optical properties $\mu_a = 0.01$ mm^{-1} and $\mu_s' = 1.0$ mm^{-1}. Validation of individual layers optical properties was performed by the data collected on large cylindrical samples of each layer using 785 nm wavelength laser diode as the source. Two-dimensional cross-sections of this gelatin phantom optical properties are displayed in increments of 2.5 mm spanning from z = -12.5 mm to z = 12.5 mm (from left-hand side to right-hand side) in top rows of Fig. 10 (a) and (b). In this phantom case, data was collected using only one layer of fibers (at z = 0 mm) leading to 240 lnA data points and 240 θ data points. A cylindrical mesh consisting 8990 nodes corresponding to 44803 linear terahedral elements was used and the experimental data was also calibrated using a reference homogenous phantom data. The outer layer (mimicing fatty layer) optical properties were used as initial guess for reconstruction procedures. A second mesh with the same geometry contianing 3718 nodes (16627 linear tetrahedral elements) was used as a reconstruction mesh.

6. Results

The number of operations required to produce an optical property update ($\triangle\mu_i$) for both the original and alternative GLS update equations (Eqs. 9 and 16, respectively) was compared as a function of the ratio of the number of estimation parameters (NN) to the number of measurements (NM). A similar comparison for LM update equations (Eqs. 5 and 6) was also performed. The results are plotted in Fig. 2(a) and (b) respectively. The expressions used for calculating the number of operations are given in Appendix-A.4. Memory required for implementing these inversions are presented in Fig. 2(c). To relate the analysis to existing experiments, NM was chosen to be 720. The number of nodes (equivalently estimation parameters) was varied from 2 to 80,000. The number of computations increases for both LM and GLS cases as NN increases, but the alternative form for GLS (GLS-AF) has a

lower computational cost when NN/NM is greater than 6. In the case of alternative form LM (LM-AF), this is when NN/NM is greater than 2. In terms of memory, as soon as $NN > NM$, both GLS-AF and LM-AF requirement is less than GLS and LM counterparts.

In order to assess algorithm performance, a series of test reconstructions were evaluated. Data with 1% noise from the cylinder containing a 15 mm diameter spherical target (first rows of Fig. 3(a) and (b)) was reconstructed for the optical properties using LM and GLS techniques (middle and last rows and Fig. 3(a) and (b)). In the case of the GLS scheme, the reformulated update equation (alternative form - Eq. 16) was used (last rows of Fig. 3(a) and (b)). However, it was also important to confirm that the two forms of the update equation (Eqs. 9 and 16) produced numerically equivalent solutions. Figure 4 shows a comparison of results generated with the original GLS update equation (Eq. 9) and its alternative form (Eq. 16) in terms of data-model misfit (δ) and reconstructed optical properties. The difference plots (Figs. 4(b) and (d)) demonstrate that Eqs. 9 and 16 are equal within the limits of the numerical precision to be expected ($< 10^{-8}$ of the L2-norm value, after the first few iterations). A similar analysis between the original LM update equation (Eq. 5) and its alternative form (Eq. 6) was performed gave similar results (not shown here). Reconstruction results with different target shapes and positions are summarized in Table-1 which reports the mean and standard deviation of recovered μ_a and μ_s' values in the background and target areas. Note that the recovered optical properties between Z = 15 mm and Z = -15 mm were used because the reconstructed optical properties were equal to the actual background values and the standard deviation was zero (within round-off error limits) above/below these Z-values.

To show the robustness of the GLS procedure, data with 5% noise was used in the reconstruction of a cylindrical target located in the center (as shown first rows of Fig. 5(a) and (b)). The reconstruction results using the LM and GLS schemes are presented in middle and last rows of Fig. 5(a) and (b) respectively. The GLS minimization technique was able to localize the target more clearly than the LM method.

To see the effect of target size on the recovery of its contrast using these reconstruction techniques, a series of simulations were performed where the diameter of the spherical target located at the center was varied (from 10 to 35 mm). One set of results is presented for the 15 mm diameter target in Fig. 3. Another sample set for a target with diameter of 10 mm is shown in Fig. 6. A comparison plot is given in Fig. 7. The data noise level for the cases considered here is 1%. Increase in the diameter of the spherical target increases the contrast recovery.

A performance comparison of these reconstruction techniques with increases in target (spherical object with diameter of 25 mm) contrast (from 2 to 10 with respect to background optical properties) located at the center (0,0,0) and (20,0,0) is presented in Fig. 8. Again, the noise level in the data was 1%. The recovery of contrast is much lower in the case of the centered target compared to the off-centered location in both LM and GLS techniques. Between the LM and GLS methods, the later performs better in terms of recovery of contrast.

A study was conducted to evaluate estimation parameter independence (cross-talk) in these reconstruction procedures. The spherical target having a contrast of 2:1 only in μ_a was considered at the center and near the boundary of the imaging domain. Synthetic data with 1% noise was used in the reconstructions, and the results are presented in Table-2 in terms of recovered mean and standard deviation of the optical properties . The recovery of contrast was higher in the GLS case and the amount of cross-talk was less (roughly 50% in the LM case compared to 30% in the GLS case). A similar study with a contrast of only in μ_s' was also conducted (not shown)and it also showed a similar trend in terms of cross-talk.

Finally, using the experimental data (Sec. 5.B) collected using a multi-layered gelatin phantom, reconstructions using both LM and GLS techniques were performed. For the GLS technique, experimental data variance was estimated (Sec. 5.A) using analytical equation, given in Eq. 22. Two-dimensional cross-sections of the actual and reconstructed optical properties distribution are plotted in Fig. 10 (a) and (b). The middle and bottom rows corresponds to the reconstruction results obtained by LM and GLS techniques. As the variance in the data (noise charterstics) are embedded in the GLS reconstruction procedure, resulting in optimal weighting (highly noisy data points gets less weightage and vice versa for less noisy data points), leading to better quantification of tumor region.

7. Discussion

Appendix (A.1) presents a computationally efficient form for implementing an iterative GLS reconstruction scheme which reduces the dimensionality of the matrix to be inverted. The alternative forms for other minimization methods are also developed in the appendices (A.2 and A.3). Appendix-A.4 presents expressions for estimating the operations count of both forms of the GLS update equations (Eqs. 9 and 16) for a single iteration. This appendix (A.4) also gives operations count for both LM and its alternative form (Eqs. 5 and 6) as well. Fig. 2 shows a log-log plot of operations count as a function of the ratio of number of optical property parameters (NN) to number of measurements (NM) which determines the form of the GLS and LM update equation to be preferred (given that both produce

numerically equivalent results as reported in Fig. 4). For example, when spatial-priors are available, the number of optical unknowns can be reduced to the number of regions that can be segmented[32] which in the case of breast tissue, is typically NN = 3 (assuming fatty, fibroglandular and tumor regions).[32] Here, since NM $\gg$ NN, the original LM and GLS update equation (Eqs. 5 and 9 respectively) is effective. In under-determined problems, such as the cases considered in this paper, where NM $\ll$ NN (NN/NM ratio of 12 in the test problems), the GLS alternative form reduces the number of operations (by up to two times in Fig. 2(a) when NN/NM = 12). In fact, the alternative form of the GLS update equation (Eq. 16) becomes effective once NN/NM $>$ 6 and the number of operations decreases by an order of magnitude when NN/NM reaches 100. For the LM minimization scheme, alternative form reduces the number of operations by a factor of 6 in Fig. 2(b) when NN/NM = 12. The memory required for inverting such matrices is plotted in Fig. 2(c) as a function of NN/NM. It is also important to recognize that the memory required to complete these operations can become critical because the cache sizes and RAM available on different architectures is variable but influences the efficiency of the computational processes executing on a given platform.

Under-determinedness of the imaging problem (i.e. NN/NM $>$ 1) leads to non-uniqueness in the solution space, but regularization helps to give a unique solution in these cases. Typically NN/NM values are between 2 to 10 for a typical two-dimensional (2D) problem, as the choice depends on the expected resolution in the reconstructed image, imaging domain size, shape, data-collection geometry and prior information available. For a 3D problem, this choice (NN/NM values) also depends on these factors, but one expects this ratio to be higher than the 2D case as the imaging domain size is bigger reflecting in the number of imaging parameters (NN) to be larger (Typical example: NN = 600 (in 2D) and 6000 (in 3D)). Ideally, one would like to have this ratio (NN/NM) constant between 2D and 3D, which implies that the number of measurements has to increase by the same factor (typical case requires a factor of 10), which might not be feasible due to instrumentation constrains.[24] This leads to choice of NN/NM greater than 6 at least, where the derived forms are effective (even though in the case of LM, the alternative form is effective when NN/NM $>$ 2). It is also important to note that, ideally one would like mesh the volume where the sensitivity is greater (for the imaging domain discussed here z between -25 mm and 25 mm) finer and rest of the domain coarser, to keep NN/NM in the same range as in 2D (typically 3-8). This adaptive meshing gets trickier when the patients are imaged, in our experience, we could not find appropriate tools that could be used in real-time for this meshing problem. Even though efforts to solve this patient-specfic adaptive meshing is being pursued.[30,31] Even when NN/NM = 3 (lowest ratio one expects in a 3D imaging problem),

from Fig. 2(b), the alternative form (LM-AF, Eq. 6) in the case of LM minimization scheme becomes effective.

Figure 4 demonstrates that the two GLS update forms (Eqs. 9 and 16) are equivalent numerically (within the numerical precision of the L2 norm value). For the cases considered here, the computation time for each iterative update using Eq. 16 was approximately 46 minutes, which was three times faster than with Eq. 9 (computation time $\sim$ 126 minutes per iteration). In terms of operations count, a factor of 2 reduction would be estimated from Fig. 2(a) for the NN/NM ratio involved. The deviation in run-time that occurs in practice is likely due to the cost of memory management alluded to above in the case of Eq. 9. It is also important to note that implementation of Eq. 9 requires an inversion of the covariance matrix (Eq. 10), whereas this matrix can be used directly in Eq. 16. In the case of Levenberg-Marquardt (LM) update equations, computation time for an iteration using Eq. 6 was approximately 21 minutes and for Eq. 5 was 91 minutes. The deviation from factor of 6 (from Fig. 2(b)) is mainly due to the memory required to perform these operations, which affects run time in turn.

Middle and last rows of Fig. 3(a) and (b) indicate that with 1% noise in the data, LM has failed to recover μ_a in a spherical target with a diameter of 15 mm located at the center, whereas GLS was able to identify the target very well. The failure of LM minimization is indicative of a lack of sensitivity at the center of the domain[24] which is improved through the GLS approach by including the noise characteristics and covariances associated with the problem. When the same target is located near the boundary (at (30,0,0)), both techniques were able to recover the contrast approximately 20% better relative to the center position (Table-1).

When 1% noisy data generated from a centered cylindrical target with a diameter of 15 mm (first rows of Fig. 5(a) and (b)) was used in the reconstruction, both LM and GLS techniques were able to recover approximately 50% of the expected contrast (Table-1). For the same type of target located near the boundary (at (30,0)), the recovery of contrast was approximately 70% in the case of GLS. For LM, the recovery was only 50% for μ_a and 85% for μ_s' under these conditions. The reconstruction results also show that recovery of the centered target is always poor relative to an object near the boundary. This is primarily due to the hyper-sensitivity at the boundary in these cases.[24] The extended cylindrical target is essentially equivalent to the two-dimensional case of a circular inclusion and the trend observed in 3D of recovering more contrast for a target near the boundary is similar to the behavior found in 2D.[24]

When 5% noisy data was used, LM reconstruction (middle rows of Fig. 5(a) and (b)) performs poorly in terms of localization of the target, whereas GLS was able to reconstruct optical images with better quality and quantitation (up to 70%). Even though the reconstructed results using very noisy data were presented here from only one type of target, similar trends were also observed in other cases that mimic the 2D reconstructions reported in Ref.[17] These results show that GLS outperforms LM even though the data noise level is high because stability is retained by including the noise characteristics into the weight matrices used for normalization.

Accuracy in contrast recovery of local targets increases as the size of the target increases, as shown in Fig. 7. For example, the contrast recovered for a centered target below 20 mm in diameter is only about 30% of the true value and as low as 10% for the LM algorithm (Fig. 7), whereas increasing the size of target to 30 mm leads to quantitative accuracy near 100%. The GLS approach provides maximal contrast recovery and superior image quality at all sizes relative to LM (example: Fig. 6). Even when the target size is as low as 5 mm (Fig. 6), the object was well localized in the GLS case, but not with LM (Fig. 6).

The performance comparison of the algorithms in terms of contrast recovery (Fig. 8) confirms that the position of the target dictates the response. When the target had 10:1 contrast in comparison to the background, the maximum recovery of contrast was $\sim$ 5:1. GLS outperformed LM in this regard but there is a plateau in recovery of contrast at 400% of the background value.

Table-2 shows that estimation parameter dependence (cross-talk) is lower (by 20%) for GLS compared to LM, by reinforcing the independence of μ_a and μ_s' through elimination of any cross-terms in the weight matrix $\mathbf{W}_{\mu-\mu_\mathbf{0}}$ (Eq. 15). The inter-parameter dependence is complex because of the non-unique relationship between the optical property distribution and the incomplete boundary data, indicating that different formulations of the inversion tend to perform differently. Nonetheless, the estimation parameter dependence is substantially higher in 3D data-limited situations, relative to when the ratio of data to number of estimates is less skewed.

In the case of phantom data (Fig. 10), as expected GLS reconstructions showed more promising results in this test case. Characterization of the data collection system, leading to variance estimation depending on the voltage measure at PMT (Fig. 9) enabled the employment of the GLS technique for experimental data reconstructions. Both techniques

(LM and GLS) were able to give qualitative information about the target, in terms of quantification the GLS technique overtakes the LM technique (Fig. 10). It should be noted that this type of charcterization of the experimental system does not take into account coupling errors between the light collection/delivery fiber and tissue surface. These kind of unsystematic errors are difficult to estimate as it depends on many parameters, such as tissue surface roughness, tissue elastic properties, design of tissue-fiber coupling interface, repetability, and alingment of fibers. But development of these type of methods including systematic noise charcterstics in the reconstruction procedure will be taking a step in the right direction. Moreover, as it can be seen from Eq. 22, covarinces among the data points was ignored, making the data weight matrix ($\mathbf{W}_\delta$) a simple diagonal matrix. Inclusion of covariances can offer a better weighting in case of experimental data, this is under investigation as of now. Even though this test case showed very promising results, in our experience, in cases where coupling errors are dominant in the data, the GLS scheme did not yield any meaningful results. In these cases, the LM technique was able to give reasonable results.

Even though the data used here is generated by using in-plane data, it was collected only from the source fiber plane, previous invistigations indicate that the use of out-of-plane data (when the data was collected from rest of the fibers in all three planes) may not give enough advantage in terms of reconstructed image quality given an increase in the data-acquistion time and computational cost.[24] It is also important to note that, the results presented here uses a cylindrical imaging domain, this study is generic in nature, especially in terms of proving the computational efficiency of alternative forms (Fig. 2), as NN/NM was changed over a range of 0.0028 to 100 (spanning from well-determined to highly under-determined problems).

Partial volume effects can be observed in the recovery of contrast as a function of target size. The recovery of contrast was much higher for the extended cylinder target compared to the spherical inclusion (Table-1). The quantitative accuracy of reconstructed images increases with an increase in target size (Fig. 7). GLS reconstruction results of the data from a centered cylindrical object are encouraging, demonstrating recovery of more than 30% contrast in this case (other Newton-type algorithms have reported a maximum of 10% contrast recovery[7,11,13,14,24]).

8. Conclusions

Three-dimensional diffuse optical tomography is more computationally intensive because of the size of the parameter space to be reconstructed. Newton-based inversion methods that

operate on a Hessian matrix, which has dimensions of the number of measurements rather than the number of parameters, can be derived using the Sherman-Morrison-Woodbury identity and become computationally more efficient once the number of estimation parameters exceeds two times the number of measurements. Representative examples demonstrate that this form of update equation can be at least six times faster in practice in the highly under-determined problems which commonly occur in 3D. Three dimensional diffuse optical tomographic reconstruction algorithms also suffer from partial volume effects that degrade significantly the accuracy with which optical properties can be quantified. The GLS approach which incorporates structured weight matrices consisting of the variance and covariance of the data-model misfit and the optical properties, improves the quantification of optical properties by at least 20% in 3D. The GLS estimate is also robust to data noise as high as 5% – conditions under which other algorithms fail when the problem is highly under-determined. By characterizing the detector noise for systematic errors, using a multi-layered gelatin phantom data, the GLS technique can be easily employed for reconstructing experimental data and can yield better quantification of targets compared to conventional reconstruction methods. Future investigations will include thorough examination of the GLS technique when applied to phantom and clinical data and extension of the technique to direct-spectral reconstruction. The test data used in this article, along with computer algorithms, are available on a web page.[33]

A. Appendix

A.1. Alternative form for GLS update equation

Before deriving the alternative form, it is useful to catalog several properties of the weight-matrices and their inverses.[28]

$$\begin{array}{c} \mathbf{W}_{\delta} = (\mathbf{C}_{\delta})^{-1};\ \mathbf{W}_{\mu-\mu_{\mathbf{0}}} = (\mathbf{C}_{\mu-\mu_{\mathbf{0}}})^{-1} \\ (\mathbf{W}_{\delta})^{T} = \mathbf{W}_{\delta};\ (\mathbf{W}_{\mu-\mu_{\mathbf{0}}})^{T} = \mathbf{W}_{\mu-\mu_{\mathbf{0}}} \\ (\mathbf{C}_{\delta})^{T} = \mathbf{C}_{\delta};\ (\mathbf{C}_{\mu-\mu_{\mathbf{0}}})^{T} = \mathbf{C}_{\mu-\mu_{\mathbf{0}}} \end{array} \tag{23}$$

If a square matrix $\mathbb{A}$, has block form

$$\mathbb{A} = \begin{bmatrix} -\mathbf{C}_{\delta} & \mathbf{J} \\ \mathbf{J}^{T} & \mathbf{W}_{\mu-\mu_{\mathbf{0}}} \end{bmatrix} \tag{24}$$

with dimensions (2NM+2NN)x(2NM+2NN), it is readily shown to be symmetric by invoking the relationships in Eq. 23:

$$(\mathbb{A})^{T} = \begin{bmatrix} -\mathbf{C}_{\delta} & \mathbf{J} \\ \mathbf{J}^{T} & \mathbf{W}_{\mu-\mu_{\mathbf{0}}} \end{bmatrix}^{T} = \begin{bmatrix} -\mathbf{C}_{\delta}{}^{T} & (\mathbf{J}^{T})^{T} \\ \mathbf{J}^{T} & \mathbf{W}_{\mu-\mu_{\mathbf{0}}}{}^{T} \end{bmatrix} = \begin{bmatrix} -\mathbf{C}_{\delta} & \mathbf{J} \\ \mathbf{J}^{T} & \mathbf{W}_{\mu-\mu_{\mathbf{0}}} \end{bmatrix} = \mathbb{A}. \tag{25}$$

Since inverses of both $\mathbf{C}_\delta$ and $\mathbf{W}_{\mu-\mu_\mathbf{0}}$ exist, then $\mathbb{A}^{-1}$ also exists and can be expressed in block form as well

$$\mathbb{A}^{-1} = \begin{bmatrix} \mathbf{P} & \mathbf{Q} \\ \mathbf{R} & \mathbf{S} \end{bmatrix} \tag{26}$$

in which case

$$\mathbb{A}\mathbb{A}^{-1} = \begin{bmatrix} -\mathbf{C}_\delta & \mathbf{J} \\ \mathbf{J}^T & \mathbf{W}_{\mu-\mu_\mathbf{0}} \end{bmatrix} \begin{bmatrix} \mathbf{P} & \mathbf{Q} \\ \mathbf{R} & \mathbf{S} \end{bmatrix} = \begin{bmatrix} \mathbf{I} & \mathbf{0} \\ \mathbf{0} & \mathbf{I} \end{bmatrix} \tag{27}$$

requires that

$$-\mathbf{C}_\delta\mathbf{P} + \mathbf{J}\mathbf{R} = \mathbf{I} \tag{28}$$

$$-\mathbf{C}_\delta\mathbf{Q} + \mathbf{J}\mathbf{S} = \mathbf{0} \tag{29}$$

$$\mathbf{J}^T\mathbf{P} + \mathbf{W}_{\mu-\mu_\mathbf{0}}\mathbf{R} = \mathbf{0} \tag{30}$$

$$\mathbf{J}^T\mathbf{Q} + \mathbf{W}_{\mu-\mu_\mathbf{0}}\mathbf{S} = \mathbf{I}. \tag{31}$$

These relationships can be manipulated through a series of substitutions to express the blocks of $\mathbb{A}^{-1}$ in terms of combinations of the block components of $\mathbb{A}$. Specifically, Eqs. 29 and 30 along with the weight matrix properties in Eqs. 23 imply that

$$\mathbf{Q} = W_\delta\mathbf{J}\mathbf{S} \tag{32}$$

and

$$\mathbf{R} = -\mathbf{C}_{\mu-\mu_\mathbf{0}}\mathbf{J}^T\mathbf{P}. \tag{33}$$

Substituting Eq. 33 into Eq. 28 to form the expression

$$\mathbf{P} = -\left(\mathbf{C}_\delta + \mathbf{J}\mathbf{C}_{\mu-\mu_\mathbf{0}}\mathbf{J}^T\right)^{-1} \tag{34}$$

which is put back into Eq. 33 produces

$$\mathbf{R} = \mathbf{C}_{\mu-\mu_\mathbf{0}}\mathbf{J}^T\left(\mathbf{C}_\delta + \mathbf{J}\mathbf{C}_{\mu-\mu_\mathbf{0}}\mathbf{J}^T\right)^{-1}. \tag{35}$$

A similar series of steps starting with Eqs. 32 and 31 to write

$$\mathbf{S} = \left(\mathbf{W}_{\mu-\mu_\mathbf{0}} + \mathbf{J}^T\mathbf{W}_\delta\mathbf{J}\right)^{-1} \tag{36}$$

which is combined again with Eq. 32 yields

$$\mathbf{Q} = \mathbf{W}_\delta\mathbf{J}\left(\mathbf{W}_{\mu-\mu_\mathbf{0}} + \mathbf{J}^T\mathbf{W}_\delta\mathbf{J}\right)^{-1}. \tag{37}$$

Since $\mathbb{A}$ is symmetric and invertible, $\mathbb{A}^{-1}$ is symmetric as well.

$$(\mathbb{A}^{-1})^T = \begin{bmatrix} \mathbf{P} & \mathbf{Q} \\ \mathbf{R} & \mathbf{S} \end{bmatrix}^T = \begin{bmatrix} \mathbf{P}^T & \mathbf{R}^T \\ \mathbf{Q}^T & \mathbf{S}^T \end{bmatrix} = \begin{bmatrix} \mathbf{P} & \mathbf{Q} \\ \mathbf{R} & \mathbf{S} \end{bmatrix} = \mathbb{A}^{-1} \tag{38}$$

in which case

$$\mathbf{Q}^T = \mathbf{R} \tag{39}$$

Substituting the forms of $\mathbf{Q}$ and $\mathbf{R}$ (Eqs. 37 and 35, respectively) into Eq. 39 results in

$$\left[\mathbf{W}_\delta \mathbf{J} \left(\mathbf{W}_{\mu-\mu_\mathbf{0}} + \mathbf{J}^T \mathbf{W}_\delta \mathbf{J}\right)^{-1}\right]^T = \mathbf{C}_{\mu-\mu_\mathbf{0}} \mathbf{J}^T \left(\mathbf{C}_\delta + \mathbf{J}\mathbf{C}_{\mu-\mu_\mathbf{0}} \mathbf{J}^T\right)^{-1} \tag{40}$$

Equation 38 also requires $\mathbf{S}^T = \mathbf{S}$, where $\mathbf{S}$ is given by Eq. 36, which when identified in the term on the left side of Eq. 40 allows it to be rewritten as

$$\left(\mathbf{W}_{\mu-\mu_\mathbf{0}} + \mathbf{J}^T \mathbf{W}_\delta \mathbf{J}\right)^{-1} \mathbf{J}^T \mathbf{W}_\delta = \mathbf{C}_{\mu-\mu_\mathbf{0}} \mathbf{J}^T \left(\mathbf{C}_\delta + \mathbf{J}\mathbf{C}_{\mu-\mu_\mathbf{0}} \mathbf{J}^T\right)^{-1} \tag{41}$$

Alternately,

$$\mathbb{A}^{-1}\mathbb{A} = \begin{bmatrix} \mathbf{P} & \mathbf{Q} \\ \mathbf{R} & \mathbf{S} \end{bmatrix} \begin{bmatrix} -\mathbf{C}_\delta & \mathbf{J} \\ \mathbf{J}^T & \mathbf{W}_{\mu-\mu_\mathbf{0}} \end{bmatrix} = \begin{bmatrix} \mathbf{I} & \mathbf{0} \\ \mathbf{0} & \mathbf{I} \end{bmatrix} \tag{42}$$

or

$$\mathbf{R}\mathbf{J} + \mathbf{S}\mathbf{W}_{\mu-\mu_\mathbf{0}} = \mathbf{I}. \tag{43}$$

Solving for $\mathbf{S}$

$$\mathbf{S} = \mathbf{C}_{\mu-\mu_\mathbf{0}} - \mathbf{R}\mathbf{J}\mathbf{C}_{\mu-\mu_\mathbf{0}} \tag{44}$$

and substituting Eqs. 35 and 36 for $\mathbf{R}$ and $\mathbf{S}$ in Eq. 44 produces

$$\left(\mathbf{W}_{\mu-\mu_\mathbf{0}} + \mathbf{J}^T \mathbf{W}_\delta \mathbf{J}\right)^{-1} = \mathbf{C}_{\mu-\mu_\mathbf{0}} - \mathbf{C}_{\mu-\mu_\mathbf{0}} \mathbf{J}^T \left(\mathbf{C}_\delta + \mathbf{J}\mathbf{C}_{\mu-\mu_\mathbf{0}} \mathbf{J}^T\right)^{-1} \mathbf{J}\mathbf{C}_{\mu-\mu_\mathbf{0}} \tag{45}$$

Note that this derivation was adapted from Liebelt et. al.[34] A variant of Eq. 45 exists in the literature with many names, the most-common being the **Sherman-Morrison-Woodbury identity**.[35–42] It is also known as the **matrix inversion lemma**.[43,44] Even though one can start from this equation and derive the alternative forms, the complete derivation is presented here for completeness.

Substituting Eq. 45 back into Eq. 9 yields

$$\triangle\mu_i = \left[\mathbf{C}_{\mu-\mu_\mathbf{0}} - \mathbf{C}_{\mu-\mu_\mathbf{0}} \mathbf{J}^T \left(\mathbf{J}\mathbf{C}_{\mu-\mu_\mathbf{0}} \mathbf{J}^T + \mathbf{C}_\delta\right)^{-1} \mathbf{J}\mathbf{C}_{\mu-\mu_\mathbf{0}}\right] \left\{\mathbf{J}^T \mathbf{W}_\delta \delta_{i-1} - \mathbf{W}_{\mu-\mu_\mathbf{0}} (\mu_{i-1} - \mu_0)\right\} \tag{46}$$

or

$$\triangle\mu_i = \left[\mathbf{I} - \mathbf{C}_{\mu-\mu_\mathbf{0}} \mathbf{J}^T \left(\mathbf{J}\mathbf{C}_{\mu-\mu_\mathbf{0}} \mathbf{J}^T + \mathbf{C}_\delta\right)^{-1} \mathbf{J}\right] \left\{\mathbf{C}_{\mu-\mu_\mathbf{0}} \mathbf{J}^T \mathbf{W}_\delta \delta_{i-1} - \mathbf{C}_{\mu-\mu_\mathbf{0}} \mathbf{W}_{\mu-\mu_\mathbf{0}} (\mu_{i-1} - \mu_0)\right\} \tag{47}$$

which results in

$$\triangle\mu_i = \left[\mathbf{I} - \mathbf{C}_{\mu-\mu_\mathbf{0}} \mathbf{J}^T \left(\mathbf{J}\mathbf{C}_{\mu-\mu_\mathbf{0}} \mathbf{J}^T + \mathbf{C}_\delta\right)^{-1} \mathbf{J}\right] \left\{\mathbf{C}_{\mu-\mu_\mathbf{0}} \mathbf{J}^T \mathbf{W}_\delta \delta_{i-1} - (\mu_{i-1} - \mu_0)\right\} \tag{48}$$

as the alternative form for the update equation (Eq. 16)

The next two subsections show the alternative forms of other least-squares minimization techniques, namely Levenberg-Marquardt and Tikhonov minimizations.

A.2. Alternative form for LM update equation

The Levenberg-Marquardt (LM) update equation (Eq. 5) is a special case of the GLS update equation (Eq. 9) when $\mathbf{W}_{\mu-\mu_\mathbf{0}} = \alpha\mathbf{I}$ and $\mathbf{W}_\delta = \mathbf{I}$ (see Sec. III.B.4 in Ref.[17]). Using these forms in Eq. 41 leads to an alternative form to Eq. 5

$$\triangle\mu_i = (\alpha\mathbf{I})^{-1}\mathbf{J}^T\left(\mathbf{J}(\alpha\mathbf{I})^{-1}\mathbf{J}^T + \mathbf{I}^{-1}\right)^{-1}\delta_{i-1} \tag{49}$$

Rearranging the terms in Eq. 49 leads to

$$\triangle\mu_i = \frac{\mathbf{J}^T}{\alpha}\left(\frac{\mathbf{J}\mathbf{J}^T + \alpha\mathbf{I}}{\alpha}\right)^{-1}\delta_{i-1} \tag{50}$$

which can be simplified to produce

$$\triangle\mu_i = \mathbf{J}^T\left(\mathbf{J}\mathbf{J}^T + \alpha\mathbf{I}\right)^{-1}\delta_{i-1}. \tag{51}$$

Eq. 51 is also known as under-determined form in the literature.[11,14]

A.3. Alternative form for Tikhonov update equation

The objective function[17,45] for the Tikhonov scheme is

$$\Omega = \|\mathbf{y} - G(\mu)\|^2 + \lambda\|\mathbf{L}(\mu - \mu_0)\|^2 \tag{52}$$

Minimization of Eq. 52 and linearizing the problem leads to update equation[17,32]

$$\triangle\mu_i = \left[\mathbf{J}^T\mathbf{J} + \lambda\mathbf{L}^T\mathbf{L}\right]^{-1}\left(\mathbf{J}^T\delta_{i-1} - \lambda\mathbf{L}^T\mathbf{L}(\mu_{i-1} - \mu_0)\right). \tag{53}$$

Equation 53 is a special case of the GLS update equation (Eq. 9) with weight matrices (see Sec. III.B.4 in Ref.[17])

$$\mathbf{W}_\delta = \mathbf{I};\ \mathbf{W}_{\mu-\mu_\mathbf{0}} = \lambda\mathbf{L}^T\mathbf{L} \tag{54}$$

From Eq. 48 one can write

$$\triangle\mu_i = \left[\mathbf{I} - \left(\lambda\mathbf{L}^T\mathbf{L}\right)^{-1}\mathbf{J}^T\left(\mathbf{J}\left(\lambda\mathbf{L}^T\mathbf{L}\right)^{-1}\mathbf{J}^T + \mathbf{I}^{-1}\right)^{-1}\mathbf{J}\right]\left\{\left(\lambda\mathbf{L}^T\mathbf{L}\right)^{-1}\mathbf{J}^T\mathbf{I}\delta_{i-1} - (\mu_{i-1} - \mu_0)\right\} \tag{55}$$

which leads to

$$\triangle\mu_i = \left[\mathbf{I} - \left(\mathbf{L}^T\mathbf{L}\right)^{-1}\mathbf{J}^T\left(\mathbf{J}\left(\mathbf{L}^T\mathbf{L}\right)^{-1}\mathbf{J}^T + \lambda\mathbf{I}\right)^{-1}\mathbf{J}\right]\left\{\left(\lambda\mathbf{L}^T\mathbf{L}\right)^{-1}\mathbf{J}^T\delta_{i-1} - (\mu_{i-1} - \mu_0)\right\} \tag{56}$$

Assuming $\mu_{i-1} = \mu_0$, the single-step Tikhonov update equation (or its equivalent)[14,46,47] becomes

$$\triangle\mu_i = \left(\mathbf{J}^T\mathbf{J} + \lambda\mathbf{L}^T\mathbf{L}\right)^{-1}\mathbf{J}^T\delta_{i-1} \tag{57}$$

Using Eqs. 41 and 54 leads to

$$\triangle\mu_i = \left(\lambda \mathbf{L}^T\mathbf{L}\right)^{-1}\mathbf{J}^T\left(\mathbf{J}\left(\lambda \mathbf{L}^T\mathbf{L}\right)^{-1}\mathbf{J}^T + \mathbf{I}^{-1}\right)^{-1}\delta_{i-1} \tag{58}$$

which can be rearranged to

$$\triangle\mu_i = \left(\mathbf{L}^T\mathbf{L}\right)^{-1}\mathbf{J}^T\left(\mathbf{J}\left(\mathbf{L}^T\mathbf{L}\right)^{-1}\mathbf{J}^T + \lambda\mathbf{I}\right)^{-1}\delta_{i-1} \tag{59}$$

Eq. 59 is also known as under-determined Tikhonov single-step update equation.[11,14,16]

A.4. Calculation of number of operations for LM and GLS update equations

The number of operations was estimated by assuming that divisions/multiplications consume most of the processor cycles. Note that Gaussian elimination was used in computing matrix inversion. Typically, Gaussian elimination for an NxN matrix requires $((N^3/3) + N^2 - (N/3))$ operations.[42] The memory required to invert a matrix of dimension NxN is N^2.[42] The number of operations only includes solution of the update equation and does not account for the number of operations required to form the matrices/vectors used in these equations.

For the GLS update equation (Eq. 9), the number of operations required for iteration i is (using the dimensions defined after Eq. 15)

$$\begin{aligned} Number\ of\ operations = &\left[(2NM*2NM*2NN) + (2NN*2NM*2NN) + \left(\tfrac{(2NN)^3}{3} + (2NN)^2 - \tfrac{2NN}{3}\right)\right] \\ &+(2NN*2NN*1) + [(2NN*2NM*1) + (2NM*2NM*1) + (2NN*2NN*1)] \end{aligned} \tag{60}$$

For the alternative form for the GLS update equation (Eq. 16), the number of operations is

$$\begin{aligned} Number\ of\ operations = &[(2NN*2NN*2NM) + (2NM*2NN*2NM) + (2NN*2NN*2NM) \\ &+\left(\tfrac{(2NM)^3}{3} + (2NM)^2 - \tfrac{2NM}{3}\right) + (2NM*2NM*2NN)] \\ &+(2NN*2NN*1) + [(2NN*2NN*2NM) + (2NN*2NM*1) + (2NM*2NM*1)] \end{aligned} \tag{61}$$

Similarly, for the LM update equation (Eq. 5), the number of operations required for iteration i is

$$Number\ of\ operations = \left[(2NN*2NM*2NN) + \left(\frac{(2NN)^3}{3} + (2NN)^2 - \frac{2NN}{3}\right)\right] + (2NN*2NM*1) \tag{62}$$

The number of operations for the alternative form for the LM update equation (Eq. 6) is

$$\begin{aligned} Number\ of\ operations = &(2NN*2NM*1) + \left[(2NM*2NN*2NM) + \left(\tfrac{(2NM)^3}{3} + (2NM)^2 - \tfrac{2NM}{3}\right)\right] \\ &+(2NM*2NM*1) \end{aligned} \tag{63}$$

Note that the computation time for these update equations is not only dependent on the number of operations needed to be performed, but also on the memory required for implementing the operations.

Acknowledgments

P.K.Y. acknowledges the DOD Breast Cancer predoctoral fellowship (BC050309). D.R.L. acknowledges support of NSF through grants DMS-0417769. This work has been sponsored by the National Cancer Institute through grants RO1CA78734 and PO1CA80139.

References

1. D. A. Boas, D. H. Brooks, E. L. Miller, C. A. DiMarzio, M. Kilmer, R. J. Gaudette, and Q. Zhang, "Imaging the body with diffuse optical tomography," IEEE Sig. Proc. Mag. **18**, 57–75 (2001).
2. S. Srinivasan, B. W. Pogue, S. Jiang, H. Dehghani, C. Kogel, S. Soho, J. J. Gibson, T. D. Tosteson, S. P. Poplack and K. D. Paulsen, "Interpreting Hemoglobin and Water Concentration, Oxygen Saturation and Scattering Measured In Vivo by Near-Infrared Breast Tomography," Proc. Nat. Acad. Sci. U.S.A. **100**, 12349–12354 (2003).
3. A. Gibson, J. C. Hebden, and S. R. Arridge, "Recent advances in diffuse optical tomography," Phys. Med. Biol. **50**, R1-R43 (2005).
4. D. R. Leff, O. J. Warren, L. C. Enfield, A. Gibson, T. Athanasiou, D. K. Patten1, J. Hebden, G. Z. Yang, and A. Darzi1, "Diffuse optical imaging of the healthy and diseased breast: A systematic review," Breast Cancer Res Treat. 2007 [Epub: ahead of print].
5. S. R. Arridge and J. C. Hebden, "Optical imaging in medicine: II. Modelling and reconstruction," Phys. Med. Biol. **42**, 841–853 (1997).
6. S. R. Arridge, "Optical tomography in medical imaging," Inv. Problems **15**, R41–R93 (1999).
7. M. Schweiger and S. R. Arridge, "Comparison of two- and three-dimensional reconstruction methods in optical tomography," Appl. Opt. **37**, 7419–7428 (1998).
8. H. Jiang, Y. Xu, N. Iftimia, J. Eggert, K. Klove, L. Baron, and L. Fajardo, "Three-dimensional optical tomographic imaging of breast in a human subject," IEEE Trans. Med. Imaging **20**, 1334–1340 (2001).
9. B. W. Pogue, S. Geimer, T. O. McBride, S. Jiang, U. L. sterberg, and K. D. Paulsen, "Three-dimensional simulation of near-infrared diffusion in tissue: boundary condition and geometry analysis for finite element image reconstruction," Appl. Opt. **40**, 588–600 (2001).
10. J. C. Hebden, H. Veenstra, H. Dehghani, E. M. C. Hillman, M. Schweiger, S. R. Arridge, and D. T. Delpy, "Three-dimensional time-resolved optical tomography of a conical breast phantom," Appl. Opt. **40**, 3278–3287 (2001).
11. H. Dehghani, B. W. Pogue, S. P. Poplack, and K. D. Paulsen, "Multiwavelength three-dimensional near-infrared tomography of the breast: initial simulation, phantom, and clinical results," Appl. Opt. **42**, 135–145 (2003).
12. A. Gibson, R. M. Yusof, E. M. C. Hillman, H. Dehghani, J. Riley, N. Everdale, R. Richards, J. C. Hebden, M. Schweiger, S. R. Arridge, and D. T. Delpy, "Optical tomography of a realistic neonatal head phantom," Appl. Opt. **42**, 3109–3116 (2003).
13. H. Dehghani, B. W. Pogue, J. Shudong, B. Brooksby, and K. D. Paulsen, "Three-

Dimensional Optical Tomography: Resolution in Small-Object Imaging," Appl. Opt. **42**, 3117–3128 (2003)

14. M. Schweiger, S. R. Arridge, and I. Nissila, "Gauss-Newton method for image reconstruction in diffuse optical tomography," Phys. Med. Biol. **50**, 2365–2386 (2005).
15. J. P. Culver, R. Choe, M. J. Holboke, L. Zubkov, T. Durduran, A. Slemp, V. Ntziachristos, D. N. Pattanayak, B. Chance, and A. G. Yodh, "Three-dimensional diffuse optical tomography in the plane parallel transmission geometry: Evaluation of a hybrid frequency domain/continuous wave clinical system for breast imaging," Med. Phys. **30**, 235–247 (2003).
16. M. J. Eppstein, D. E. Dougherty, D. J. Hawysz, and E. M. Sevick-Muraca "Three-dimensional Bayesian optical image reconstruction with domain decomposition IEEE Trans. Med. Imaging **20**, 147–163 (2001).
17. P. K. Yalavarthy, B. W. Pogue, H. Dehghani, and K. D. Paulsen, "Weight-Matrix Structured Regularization Provides Optimal Generalized Least-Squares Estimate in Diffuse Optical Tomography," Med. Phys. 34(6), 2085–2098 (2007).
18. S. R. Arridge and M. Schweiger, "A gradient based optimization scheme for optical tomography," Opt. Express **2**, 213–226 (1998).
19. A. H. Hielscher, A. D. Klose, and K. M. Hanson, "Gradient-based iterative image reconstruction scheme for time-resolved optical tomography," IEEE Trans. Med. Imag. **18**, 262–271 (1999).
20. H. Jiang, K. D. Paulsen, and U. Osterberg, B. W. Pogue, and M. S. Patterson, "Optical image reconstruction using frequency domain data: simulations and experiments," J. Opt. Soc. Am. A **13**, 253–266 (1996).
21. S. R. Arridge and M. Schweiger, "Photon-measurement density functions. Part 2: Finite-element-method calculations," Appl. Opt. **34**, 8026–8037 (1995).
22. M. Schweiger, S. R. Arridge, M. Hiroaka, and D. T. Delpy, "The Finite Element Model for the Propagation of Light in Scattering Media: Boundary and Source Conditions," Med. Phys. **22**, 1779–1792 (1995).
23. M. Schweiger, S. R. Arridge, and D. T. Delpy, "Application of the finite element method for the forward and inverse models in optical tomography," J. Math. Imag. Vision **3**, 263–283 (1993).
24. P. K. Yalavarthy, H. Dehghani, B. W. Pogue, and K. D. Paulsen, "Critical computational aspects of near infrared circular tomographic imaging: Analysis of measurement number, mesh resolution and reconstruction basis," Opt. Express **14**, 6113–6127 (2006).
25. K. Levenberg, "A method for the solution of certain nonlinear problems in least squares," Q. Appl. Math. **2**, 164-168 (1944).
26. D. W. Marquardt, "An algorithm for least squares estimation of nonlinear parameters,"

J. Soc. Ind. Appl. Math. **11**, 431-441 (1963).

27. S. Srinivasan, B. W. Pogue, H. Dehghani, S. Jiang, X. Song, and K. D. Paulsen, "Improved quantification of small objects in near-infrared diffuse optical tomography," J. Biomed. Opt. **9**, 1161–1171 (2004).
28. D. R. Lynch, *Numerical Partial Differential Equations for Environmental Scientists and Engineers – A First Practical Course*, Springer, 2005.
29. T. O. Mcbride, B. W. Pogue, S. Jiang, U. L. Osterberg, and K. D. Paulsen, "A parallel-detection frequency-domain near-infrared tomography system for hemoglobin imaging of the breast in vivo," Rev. Sci. Instr. **72**, 1817–1824 (2001).
30. S. Srinivasan, B. W. Pogue, C. M. Carpenter, P. K. Yalavarthy, and K. D. Paulsen, "A boundary element approach for image-guided near-infrared absorption and scatter estimation," Med. Phys. **34**, 4545–4557 (2007).
31. M. E. Eames, B. W. Pogue, P. K. Yalavarthy, and H. Dehghani, "An efficient Jacobian reduction method for diffuse optical image reconstruction," Opt. Express **15**, 15908–15919 (2007).
32. P. K. Yalavarthy, B. W. Pogue, H. Dehghani, C. M. Carpenter, S. Jiang, and K. D. Paulsen, "Structural information within regularization matrices improves near infrared diffuse optical tomography," Opt. Express **15**, 8043–8058 (2007).
33. http://nir.thayer.dartmouth.edu/gls3d.html
34. P. B. Liebelt, *An Introduction to optimal estimation*, Addison-Wesley, 1967.
35. W. J. Duncan, "Some devices for the solution of large sets of simultaneous equations (with an appendix on the reciprocation of partitioned matrices)," The London, Edinburgh and Dublin Philosophical Magazine and Journal of Science, Seventh Series **35**, 660–670 (1944).
36. J. Sherman, W. J. Morrison, "Adjustment of an inverse matrix corresponding to changes in the elements of a given column or a given row of the original matrix," Ann. Math. Statist. **20**, 621 (1949).
37. J. Sherman, W. J. Morrison, "Adjustment of an inverse matrix corresponding to changes in the elements of a given column or a given row of the original matrix," Ann. Math. Statist. **21**, 124–127 (1950).
38. M. Wooodbury, *Inverting modified matrices*, Memorandum report **42**, Statistical research group, Princeton (1950).
39. A. S. Householder, *The theory of matrices in numerical analysis*, Page-123, Dover Publications Inc., New York 1964.
40. H. V. Henderson and S. R. Searle, "On deriving the inverse of a sum of matrices," SIAM Review, **23**, 53-60 (1981).
41. G. H. Golub, C. F. Van Loan, *Matrix Computations*, Page-50, The John Hopkins uni-

versity press, Edition-III, Baltimore and London 1996.

42. J. R. Westlake, *A handbook of numerical matrix inversion and solution of linear equations*, Page-132, John Wiley & sons Inc, New York 1968.
43. J. M. Mendel, *Lessons in estimation theory for signal processing, communication, and control*, Page-62, Prentice Hall PTR, New Jersey 1995.
44. C. Wunsch, *The ocean circulation inverse problem*, Page-99, Cambridge university press 1996.
45. A. N. Tikhonov and V. A. Arsenin, *Solution of Ill-posed Problems*, Winston and Sons, Washington 1977.
46. B. Brooksby, S. Jiang, H. Dehghani, B. W. Pogue, K. D. Paulsen, J. Weaver, C. Kogel and S. P. Poplack, "Combining near infrared tomography and magnetic resonance imaging to study in vivo breast tissue: implementation of a Laplacian-type regularization to incorporate magnetic resonance structure," J. Biomed. Opt. **10**, 051504:1–10 (2005).
47. S. C. Davis, H. Dehghani, J. Wang, S. Jiang, B. W. Pogue, and K. D. Paulsen "Image-guided diffuse optical fluorescence tomography implemented with Laplacian-type regularization," Opt. Express **15**, 4066–4082 (2007).

List of Tables

Table 1: Mean and standard deviation of the reconstructed μ_a and μ_s' values in mm^{-1} for the background and target with LM and GLS techniques using data with 1% noise. The spherical target had a diameter of 15 mm. One set of reconstructed images for the target in the center is presented in Fig. 3. The cylindrical target diameter was 15 mm and extended through out the imaging domain in the z-direction.

Table 2: Mean and standard deviation of reconstructed μ_a and μ_s' in mm^{-1} values for the background and a spherical target with no scattering contrast using the LM and GLS techniques. The diameter of the spherical inclusion was 15 mm. Data with 1% noise was used.

List of Figures

Figure 1: Schematic diagram of the three-dimensional cylindrical imaging domain.

Figure 2: Comparison of the number of operations required for the original update equation and its alternative form (a). for GLS (Eq. 9, represented by GLS) and its alternative form (Eq.16, represented by GLS-AF) (b). for LM (Eq. 5, represented by LM) and its alternative form (Eq. 6, represented by LM-AF) as a function of the ratio of number of estimation parameters to number of measurements (represented by NN/NM). Memory required for implementing the inversion procedure is plotted in (c).

Figure 3: Actual and reconstructed (a) μ_a and (b) μ_s' distributions of a spherical target having a diameter of 15 mm located at the center (at (0,0,0)) using 1% noisy data. Two-dimensional cross-sections of the 3D volume in 5mm increments spanning from z = -25 mm to z = 25 mm (from left to right) are shown. Actual distributions are given in the first row. Reconstructed distribution using the Levenberg-Marquardt (LM) minimization scheme and GLS minimization scheme are presented in the middle and last rows respectively.

Figure 4: Comparison of results from the GLS update equation (Eq. 9, represented by GLS) and its alternative form (Eq.16, represented by GLS-AF). (a) L2-norm of data-model misfit (δ) as a function of iteration, (b) Difference (in %) in the curves in (a), (c) L2-norm of the solution space ($\mu_{actual} - \mu$) as a function of iteration (d) Difference (in %) in the curves in (c).

Figure 5: Actual and reconstructed (a) μ_a and (b) μ_s' distributions of a cylindrical target located at the center (diameter - 15 mm) using 5% noisy data. Two-dimensional

cross-sections of the 3D volume in 5mm increments spanning from z = -25 mm to z = 25 mm (from left to right) are shown. Actual distributions are given in the first row. Reconstructed distribution using the Levenberg-Marquardt (LM) minimization scheme and GLS minimization scheme are presented in the middle and last rows respectively.

Figure 6: Actual and reconstructed (a) μ_a and (b) μ_s' distributions of a spherical target having a diameter of 10 mm located at the center (at (0,0,0)) using 1% noisy data. Two-dimensional cross-sections of the 3D volume in 5mm increments spanning from z = -25 mm to z = 25 mm (from left to right) are shown. Actual distributions are given in the first row. Reconstructed distribution using the Levenberg-Marquardt (LM) minimization scheme and GLS minimization scheme are presented in the middle and last rows respectively.

Figure 7: Comparison of recovered optical properties as a function of inclusion size (diameter) for the spherical target located at (0,0,0) using both LM and GLS techniques. Standard deviations were of the same order as given in Table-1.

Figure 8: Comparison of recovered optical properties with respect to expected values in a spherical target located at (0,0,0) and (20,0,0) having a diameter of 25 mm using both LM and GLS reconstruction techniques. Observed standard deviations are of similar order to that reported in Table-1.

Figure 9: An error (deviation, σ) plot of the measured voltage and phase (θ) as a function of mean of measured PMT voltage. The legend of the figure represnts the fitting model used. Each data point corresponds to a sample size of 200.

Figure 10: Actual and reconstructed (a) μ_a and (b) μ_s' distributions of a cylindrical target using experimental multi-layered phantom data. Two-dimensional cross-sections of the 3D volume in 2.5 mm increments spanning from z = -12.5 mm to z = 12.5 mm (from left to right) are shown. Actual distributions are given in the first row. Reconstructed distribution using the Levenberg-Marquardt (LM) minimization scheme and GLS minimization scheme are presented in the middle and last rows respectively.

Tables

Methods	*Target*		*Background*		*Target*	
	shape	*position*	μ_a	μ_s'	μ_a	μ_s'
Actual	-	-	0.01	1.0	0.02	2.0
LM	Spherical	(0,0,0)	0.0101±0.0003	1.0079±0.0322	0.0104±0.0002	1.1259±0.0160
		(30,0,0)	0.0101±0.0006	1.0063±0.0500	0.0126±0.0009	1.4514±0.1152
	Cylindrical	(0,0)	0.0102±0.0010	1.0120±0.0874	0.0151±0.0012	1.4308±0.0854
		(30,0)	0.0101±0.0006	1.0030±0.0663	0.0148±0.0015	1.8406±0.2470
GLS	Spherical	(0,0,0)	0.0101±0.0001	1.0100±0.0212	0.0122±0.0004	1.2903±0.0326
		(30,0,0)	0.0100±0.0004	1.0108±0.0250	0.0141±0.0006	1.4498±0.0853
	Cylindrical	(0,0)	0.0102±0.0008	1.0055±0.0500	0.0159±0.0009	1.4750±0.0941
		(30,0)	0.0101±0.0008	1.0043±0.0588	0.0170±0.0012	1.6793±0.1848

Table 1

Methods	*Target position*	*Background*		*Target*	
		μ_a	μ_s'	μ_a	μ_s'
Actual	-	0.01	1.0	0.02	1.0
LM	(0,0,0)	0.0101±0.0003	1.0025±0.0211	0.0109±0.0001	1.0500±0.0071
	(30,0,0)	0.0101±0.0004	1.0009±0.0205	0.0119±0.0004	1.0934±0.0269
GLS	(0,0,0)	0.0101±0.0001	1.0016±0.0269	0.0126±0.0002	1.0924±0.0253
	(30,0,0)	0.0100±0.0004	1.0029±0.0189	0.0136±0.0003	1.1002±0.0294

Table 2

Figures

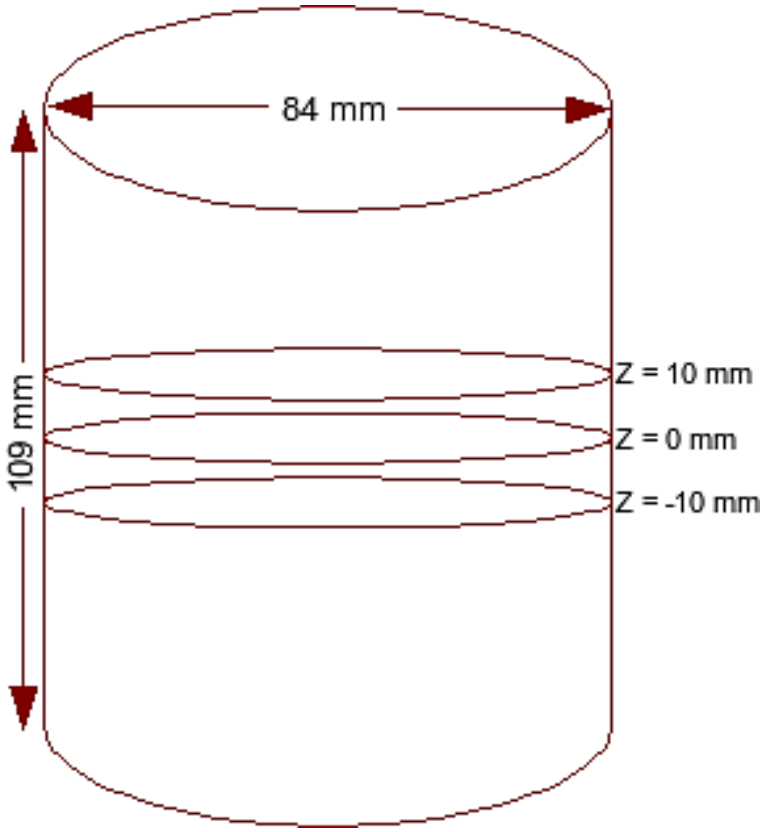

Figure 1

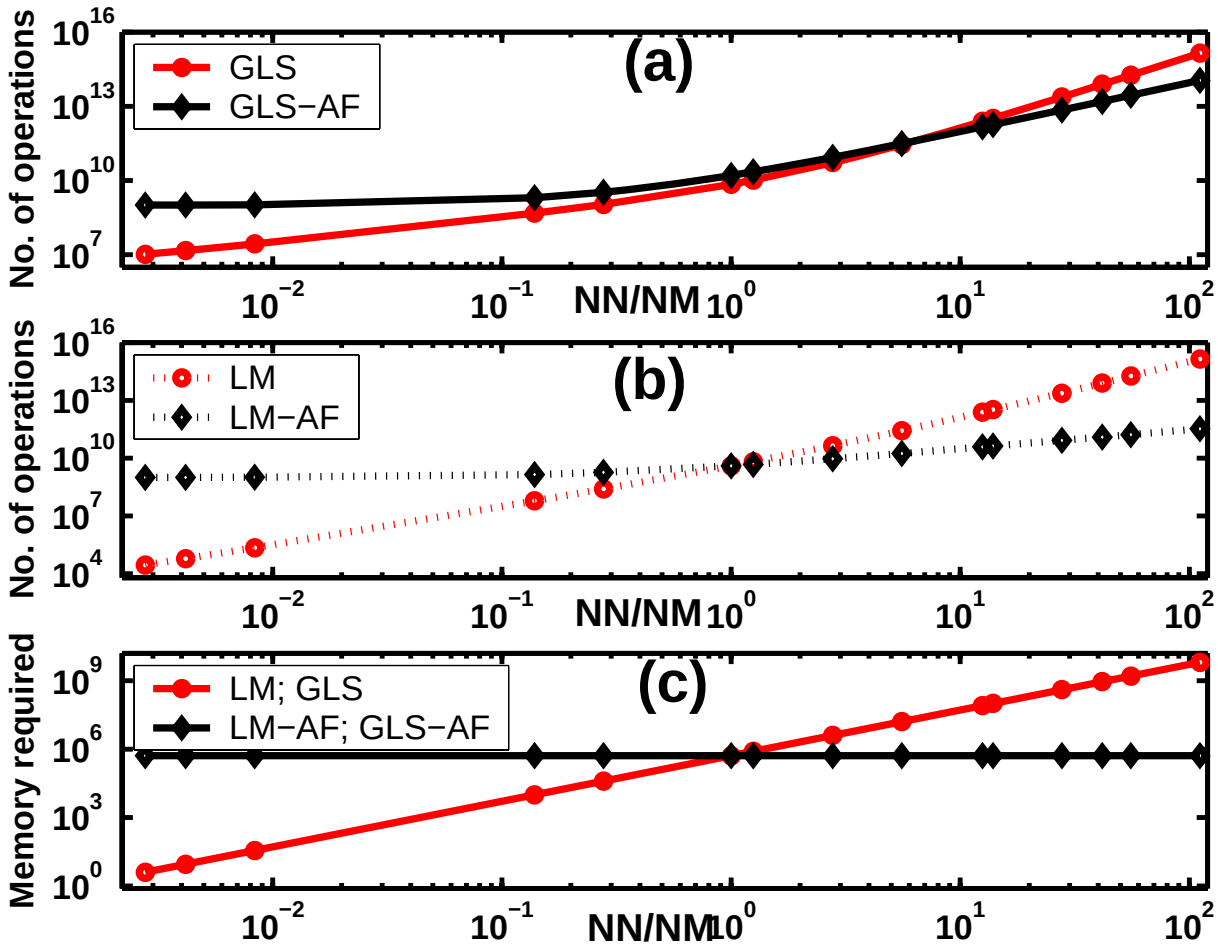
(a)
GLS
GLS−AF
No. of operations
(b)
LM
LM−AF
No. of operations
(c)
LM; GLS
LM−AF; GLS−AF
Memory required
NN/NM
NN/NM
NN/NM

Figure 2

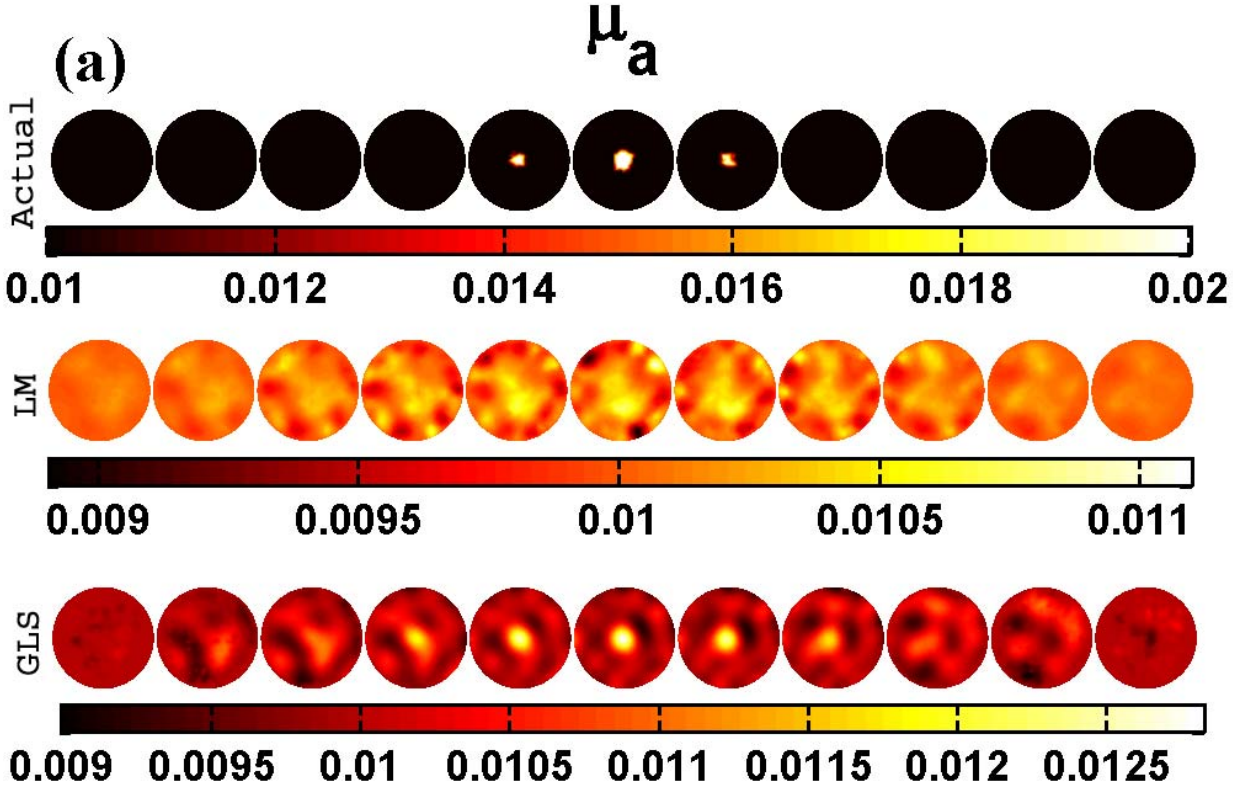
(a)
μa
Actual
0.01
0.012
0.014
0.016
0.018
0.02
LM
0.009
0.0095
0.01
0.0105
0.011
GLS
0.009
0.0095
0.01
0.0105
0.011
0.0115
0.012
0.0125

Figure 3(a)

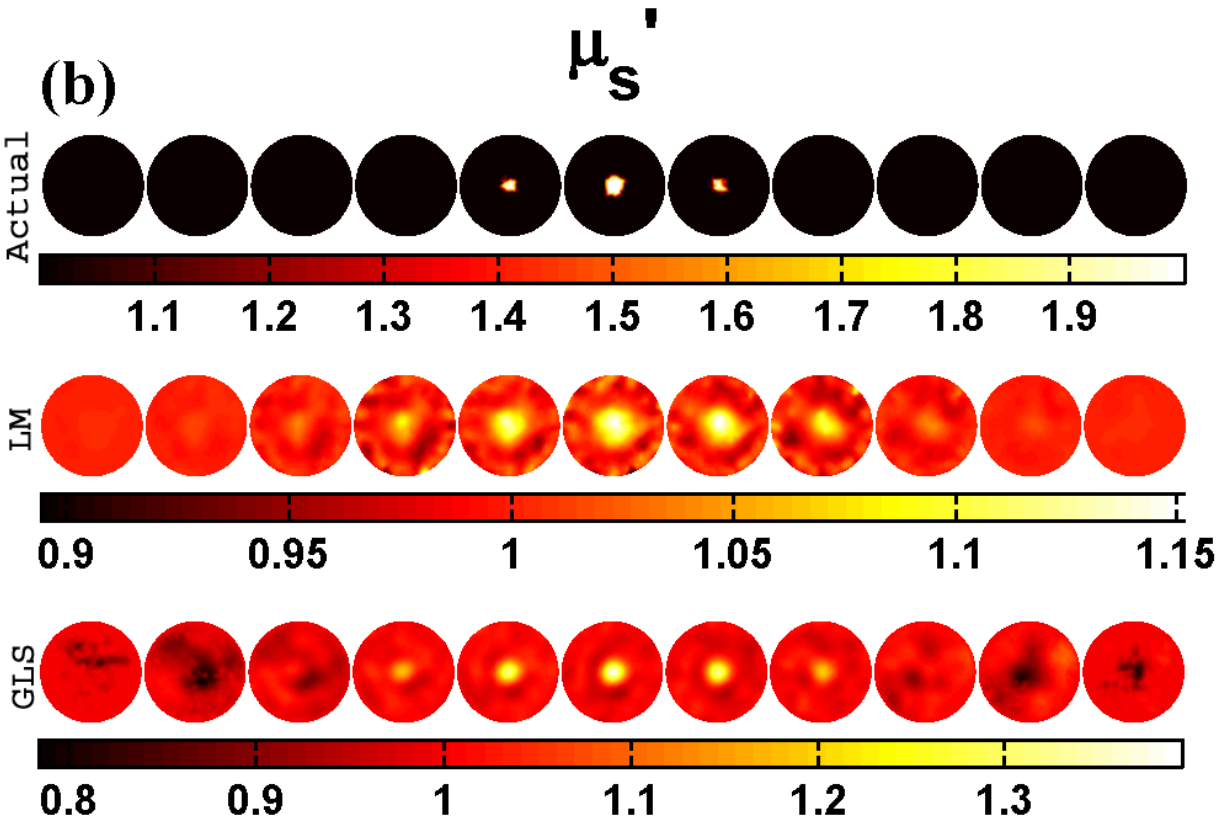
(b)
μs'
Actual
1.1
1.2
1.3
1.4
1.5
1.6
1.7
1.8
1.9
LM
0.9
0.95
1
1.05
1.1
1.15
GLS
0.8
0.9
1
1.1
1.2
1.3

Figure 3(b)

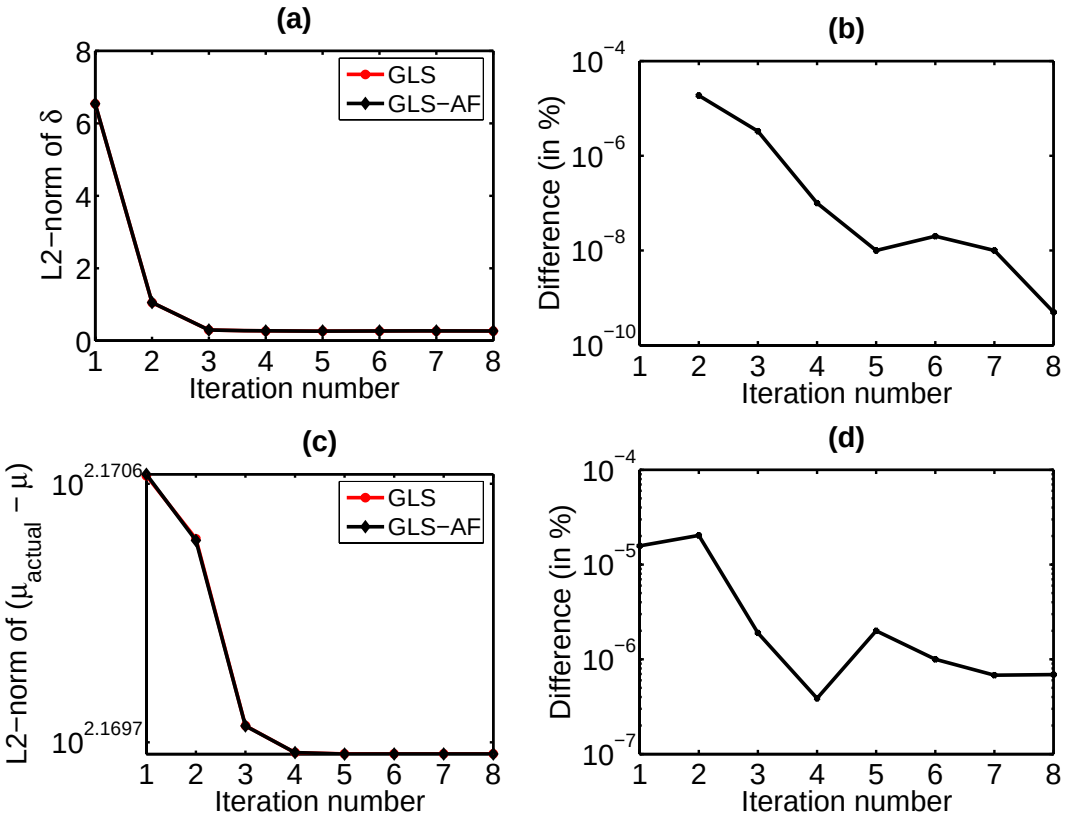
(a)
L2−norm of δ
Iteration number
GLS
GLS−AF
(b)
Difference (in %)
Iteration number
(c)
L2−norm of (μactual − μ)
Iteration number
GLS
GLS−AF
(d)
Difference (in %)
Iteration number

Figure 4

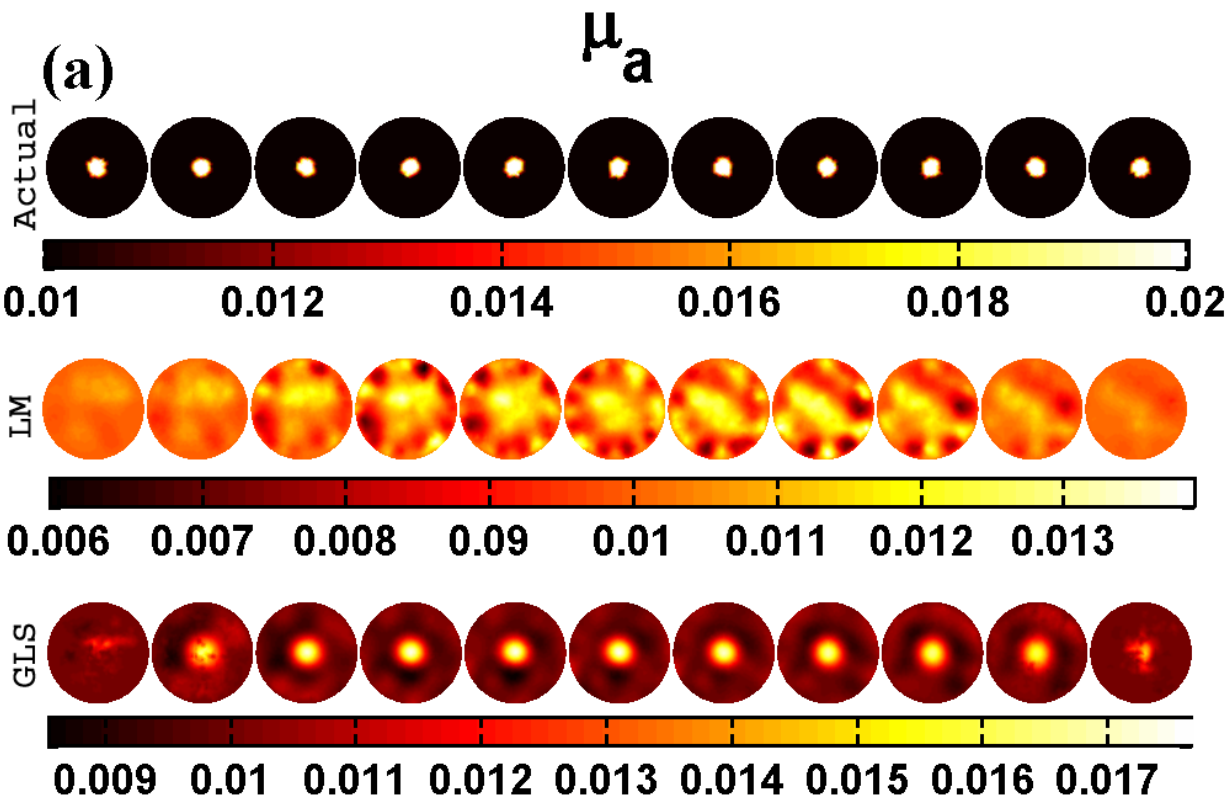
(a)
μa
Actual
0.01
0.012
0.014
0.016
0.018
0.02
LM
0.006
0.007
0.008
0.09
0.01
0.011
0.012
0.013
GLS
0.009
0.01
0.011
0.012
0.013
0.014
0.015
0.016
0.017

Figure 5(a)

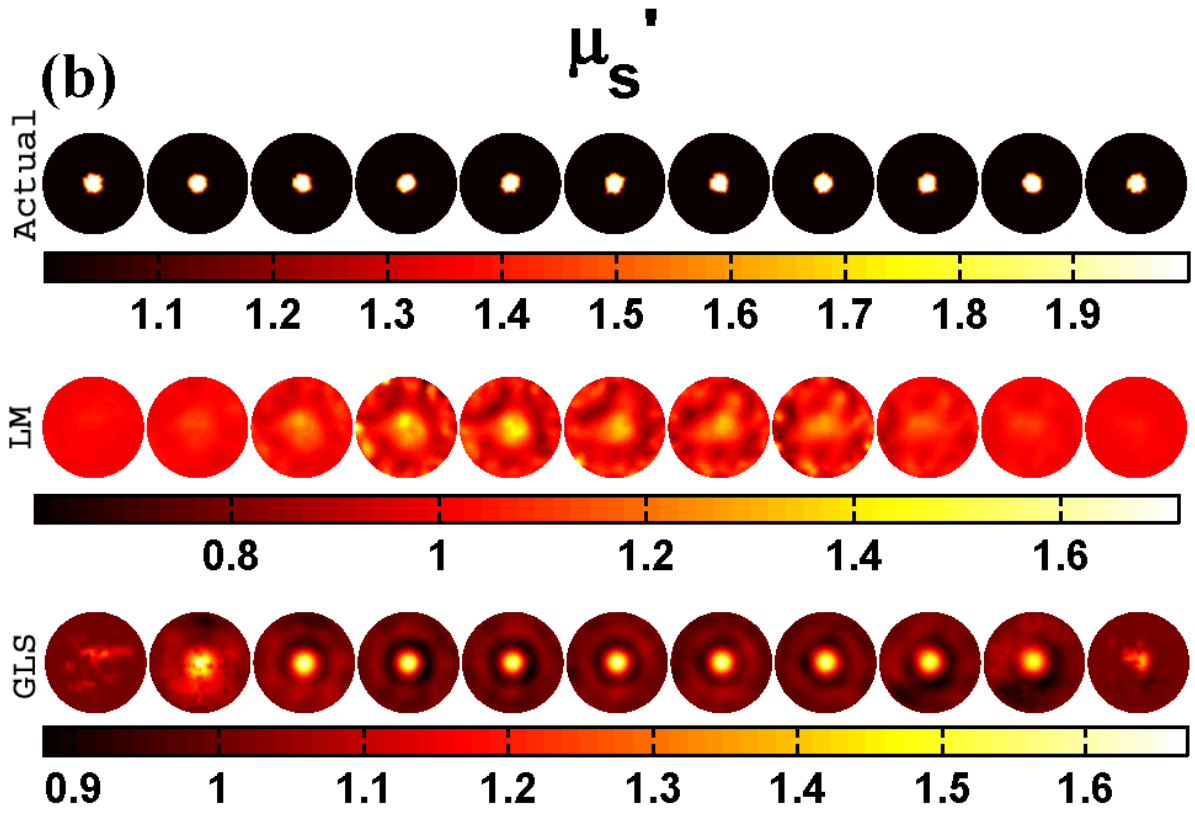
(b)
μs'
Actual
1.1 1.2 1.3 1.4 1.5 1.6 1.7 1.8 1.9
LM
0.8 1 1.2 1.4 1.6
GLS
0.9 1 1.1 1.2 1.3 1.4 1.5 1.6

Figure 5(b)

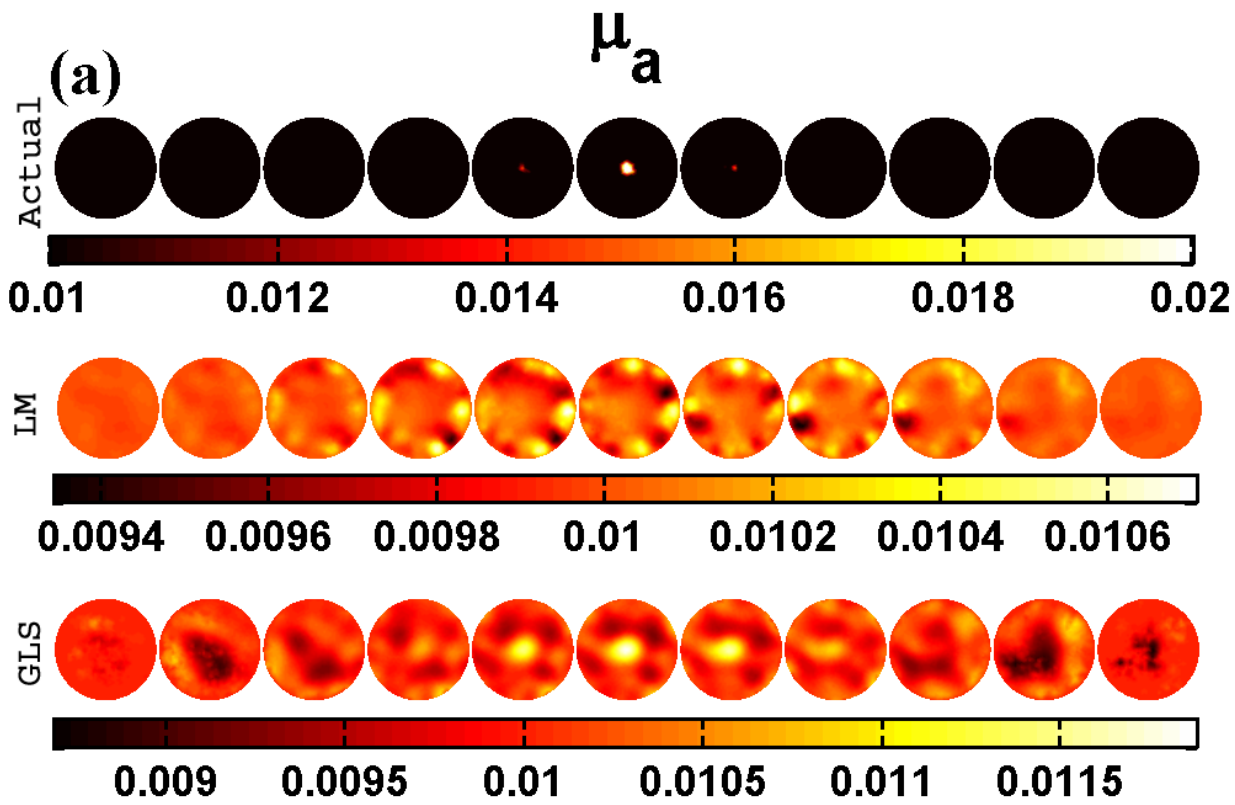
(a)
μa
Actual
0.01
0.012
0.014
0.016
0.018
0.02
LM
0.0094
0.0096
0.0098
0.01
0.0102
0.0104
0.0106
GLS
0.009
0.0095
0.01
0.0105
0.011
0.0115

Figure 6(a)

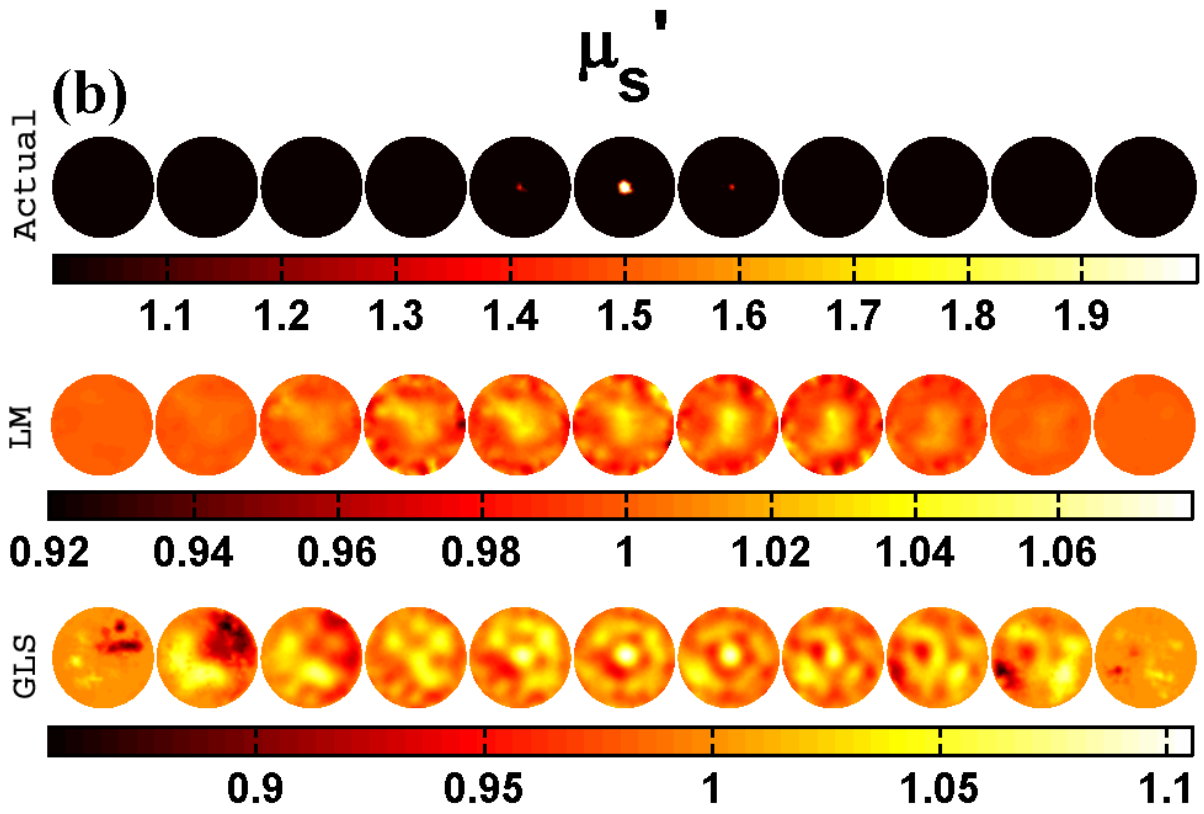
(b)
μs'
Actual
1.1
1.2
1.3
1.4
1.5
1.6
1.7
1.8
1.9
LM
0.92
0.94
0.96
0.98
1
1.02
1.04
1.06
GLS
0.9
0.95
1
1.05
1.1

Figure 6(b)

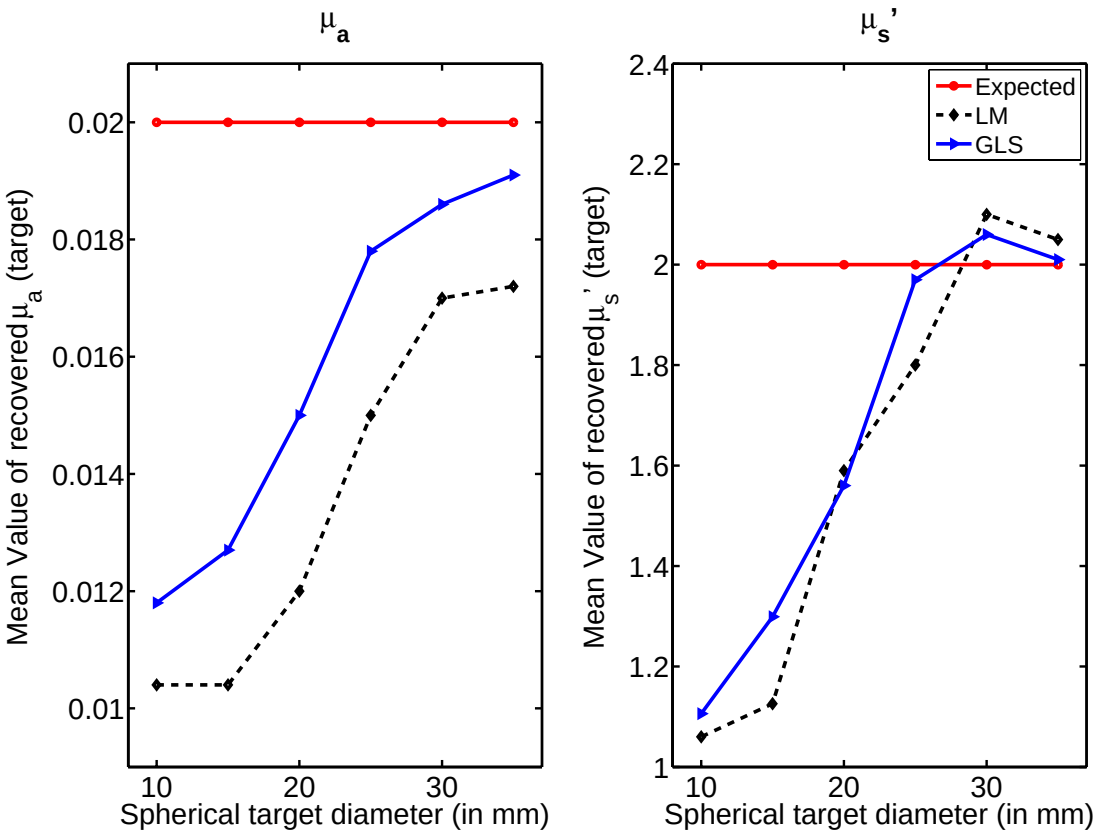
μa
μs'
Mean Value of recovered μa (target)
Mean Value of recovered μs' (target)
Spherical target diameter (in mm)
Spherical target diameter (in mm)
Expected
LM
GLS
0.02
0.018
0.016
0.014
0.012
0.01
2.4
2.2
2
1.8
1.6
1.4
1.2
1
10
20
30

Figure 7

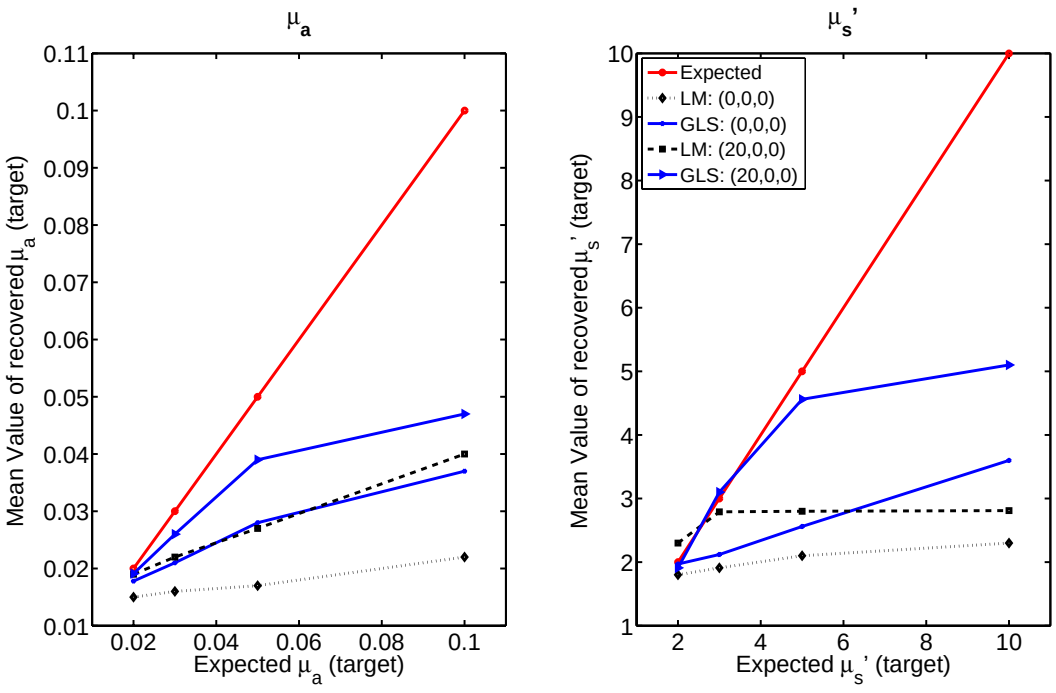
μa
μs'
Mean Value of recovered μa (target)
Expected μa (target)
Mean Value of recovered μs' (target)
Expected μs' (target)
Expected
LM: (0,0,0)
GLS: (0,0,0)
LM: (20,0,0)
GLS: (20,0,0)

Figure 8

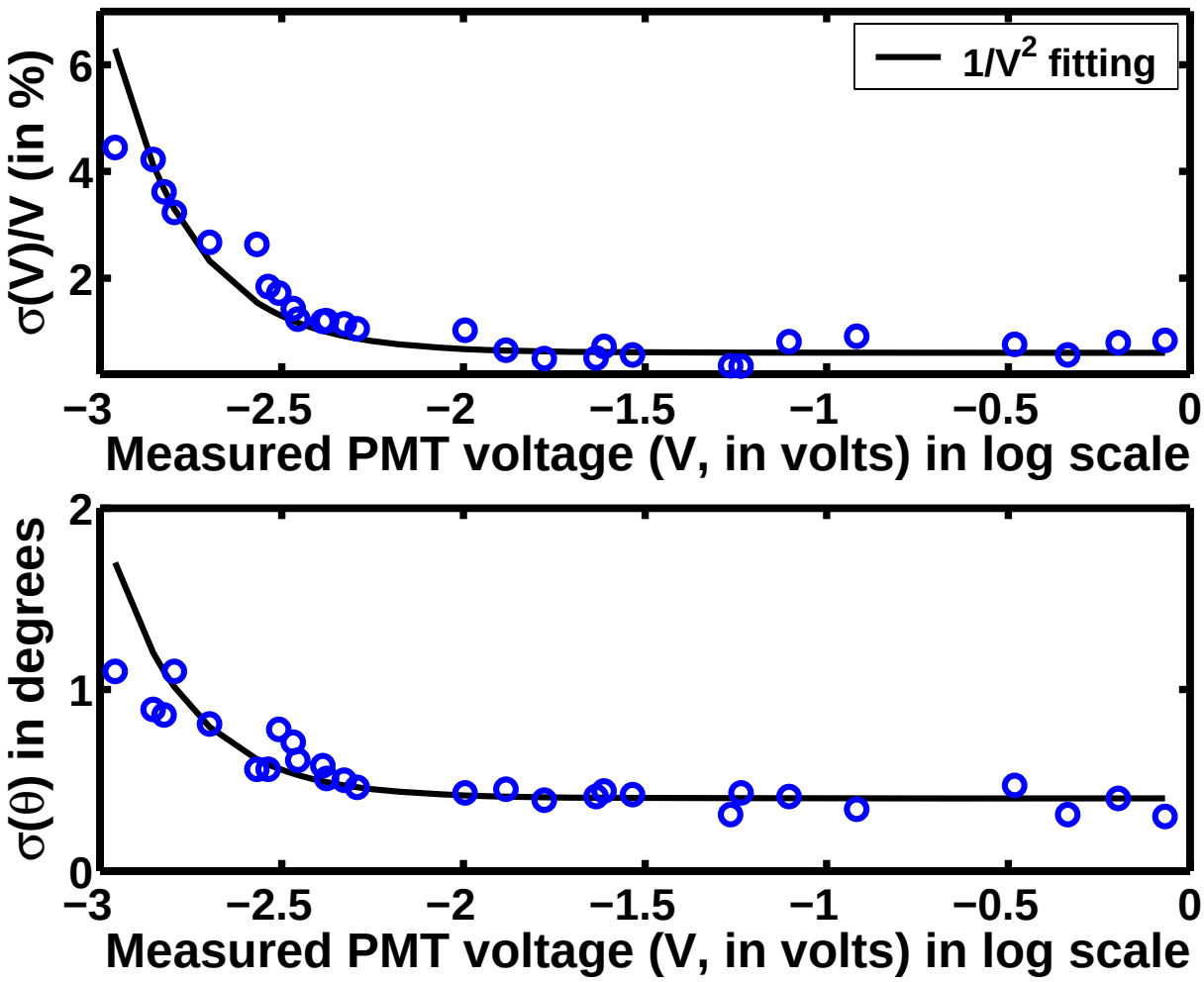
1/V^2 fitting
σ(V)/V (in %)
6
4
2
−3
−2.5
−2
−1.5
−1
−0.5
0
Measured PMT voltage (V, in volts) in log scale
σ(θ) in degrees
2
1
0
−3
−2.5
−2
−1.5
−1
−0.5
0
Measured PMT voltage (V, in volts) in log scale

Figure 9

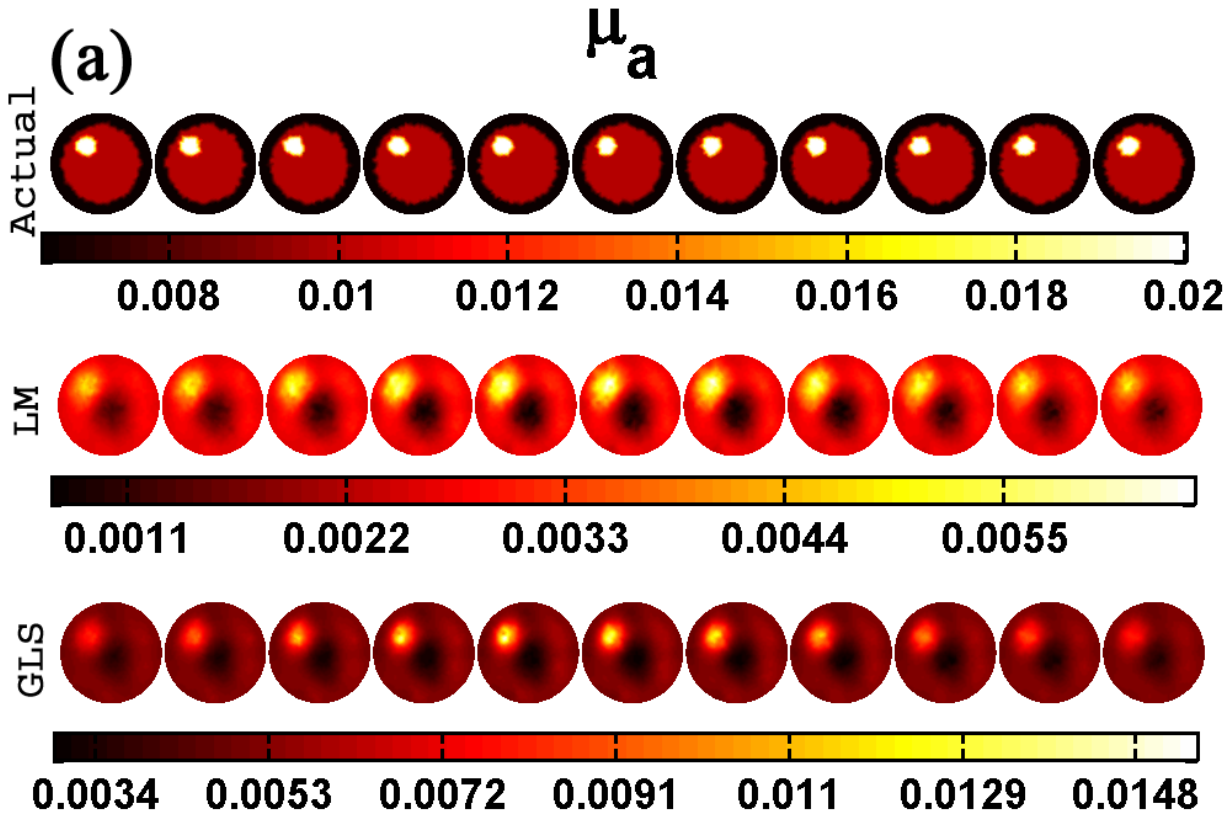
(a)
μa
Actual
0.008
0.01
0.012
0.014
0.016
0.018
0.02
LM
0.0011
0.0022
0.0033
0.0044
0.0055
GLS
0.0034
0.0053
0.0072
0.0091
0.011
0.0129
0.0148

Figure 10(a)

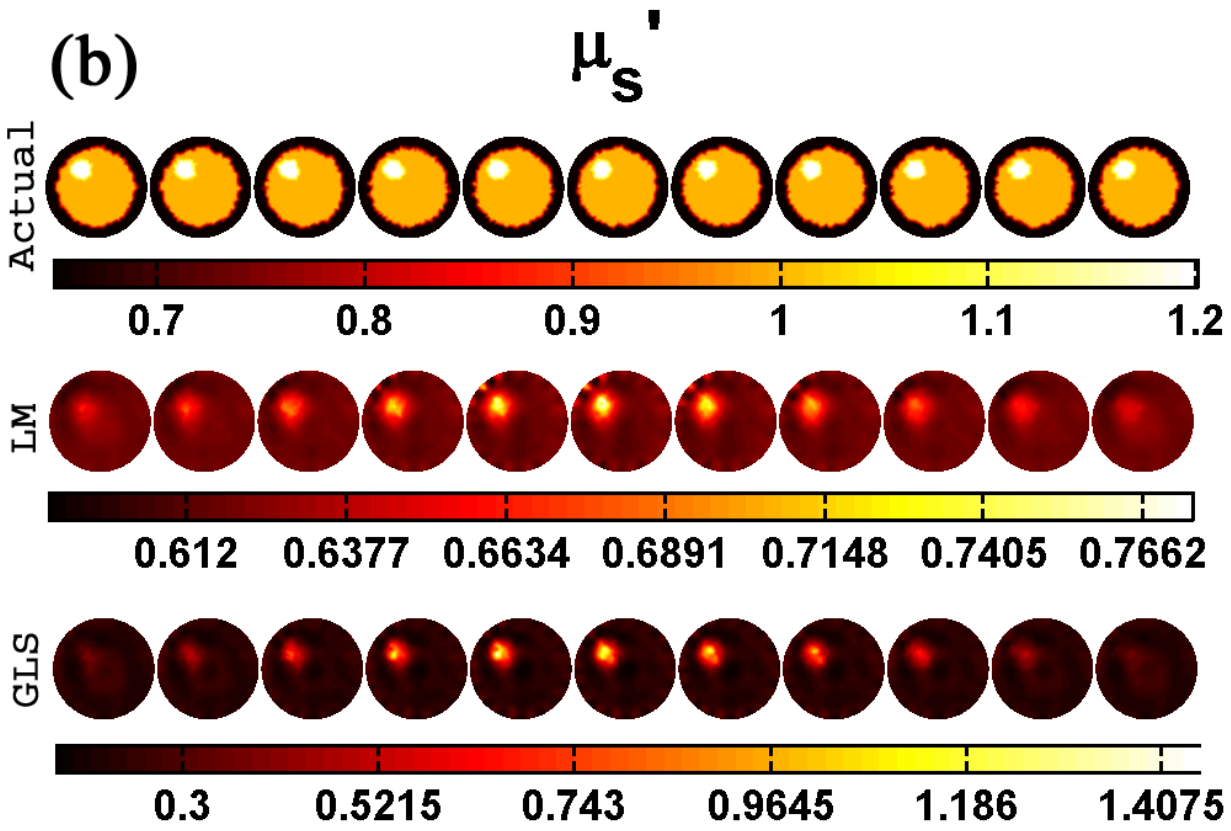
(b)
μs'
Actual
0.7
0.8
0.9
1
1.1
1.2
LM
0.612
0.6377
0.6634
0.6891
0.7148
0.7405
0.7662
GLS
0.3
0.5215
0.743
0.9645
1.186
1.4075

Figure 10(b)